UNIVERSITY OF SOUTHAMPTON

FACULTY OF ENGINEERING, SCIENCE AND MATHEMATICS

Institute of Sound and Vibration Research

ACOUSTIC OPTIMISATION AND PREDICTION OF SOUND PROPAGATION IN TURBOFAN ENGINE DUCTS

by

Iansteel Mukum Achunche

Thesis for the part award of the degree of Doctor of Engineering

January 2010

UNIVERSITY OF SOUTHAMPTON

ABSTRACT

FACULTY OF ENGINEERING, SCIENCE AND MATHEMATICS

Doctor of Engineering Thesis

by Iansteel Mukum Achunche

The research presented in this thesis explores the prediction of noise propagation and radiation in turbofan engine intakes and bypass ducts, and the optimisation of noise attenuation by using acoustic liners. A commercial FE/IE code ACTRAN/TM is used within two shell programs; B-induct for bypass ducts and ANPRORAD for intake ducts. An automated liner impedance capability has been demonstrated by exploiting an optimisation suite, SOFT.

Automated liner impedance optimisations to maximise the liner insertion loss have been performed for a uniform bypass duct with a multimodal noise source, by using B-induct within SOFT. Results show that, multi-segment liners are effective at low frequencies when few acoustic duct modes are present and less so at high frequencies when many modes are present. Other results show that, at high frequencies, having different liner impedances on the inner and outer walls could be more effective than axially segment liners. An automated liner impedance optimisation has also been performed for a realistic bypass duct, and an A-weighting has been considered.

Far field noise levels predicted by using ANPRORAD analysis have been validated against measured data from rig and engine tests. The predicted results are in good agreement with the measured data when the noise source is calibrated using in-duct measured values. This demonstrates that ANPRORAD is a viable methodology for intake noise predictions in industry. ANPRORAD has also been applied to investigate the effect of the intake geometry on low-frequency acoustic reflections in the intake, and integrated within SOFT to perform automated liner impedance optimisations to minimise acoustic reflections to the fan.

DECLARATION OF AUTHORSHIP

I, IANSTEEL MUKUM ACHUNCHE, declare that the thesis entitled,

ACOUSTIC OPTIMISATION AND PREDICTION OF SOUND PROPAGATION IN TURBOFAN ENGINE DUCTS

and the work presented in the thesis are both my own, and have been generated by me as the result of my own original research. I confirm that:

- this work was done wholly or mainly while in candidature for a research degree at this University;
- where any part of this thesis has previously been submitted for a degree or any other qualification at this University or any other institution, this has been clearly stated;
- where I have consulted the published work of others, this is always clearly attributed;
- where I have quoted from the work of others, the source is always given. With the exception of such quotations, this thesis is entirely my own work;
- I have acknowledged all main sources of help;
- where the thesis is based on work done by myself jointly with others, I have made clear exactly what was done by others and what I have contributed myself;
- parts of this work have been published as:

Iansteel Achunche, Jeremy Astley, Rie Sugimoto and Andrew Kempton, "Liner optimisation for a uniform bypass duct using B-induct and SOFT," *Aerodynamic Design and Optimisation Seminar (ADOS)*, Derby, UK, September 2008.

Iansteel Achunche, Jeremy Astley, Rie Sugimoto and Andrew Kempton, "Prediction of Forward Fan Noise Propagation and Radiation from Intakes," *15th AIAA/CEAS Aeroacoustics Conference*, Miami, FL, AIAA 2009-3239, May 2009.

Jeremy Astley, Iansteel Achunche and Rie Sugimoto, "Validation of CAA prediction of noise radiated from turbofan intakes," *The sixteenth International Congress on Sound and Vibration*, Krakow, Poland, July 2009, Paper 406.

Jeremy Astley, Iansteel Achunche, Rie Sugimoto and Andrew Kempton, "Automatic liner optimisation for bypass ducts," *Euronoise 2009*, Edinburgh, Scotland, October 2009, ANE19.

Signed:

Date:

Contents

List of Figures

List of Tables

Nomenclature

Abbreviations

ACARE	Advisory Council for Aeronautics Research
ARMOGA	Adaptive Range Multi-Objective Genetic Algorithm
BB	Broadband
BEM	Boundary Element Method
BPF	Blade Passing Frequency
CAA	Computational AeroAcoustics
CFD	Computational Fluid Dynamics
DGM	Discontinuous Galerkin Method
DHC	Dynamic Hill Climbing
DoE	Design of Experiment
DRP	Dispersion Relation Preserving
EO	Engine Order
EPNL	Effective Perceived Noise Level
FDNS	Frequency Domain Numerical Solution
FE	Finite Element
FEM	Finite Element Method
GA	Genetic Algorithm
HW	Hard-walled
ICAO	International Civil Aviation Organization
IE	Infinite Element

IFS	Inner Fixed Structure
LEE	Linearised Euler Equation(s)
ND	Nodal Diameter
OFS	Outer Fixed Structure
OGV	Outlet Guide Vane
POA	Percentage Open Area (porosity)
PWL	PoWer Level
RBF	Radial Basis Function
RSM	Response Surface Modelling
SOFT	Smart Optimisation For Turbomachinery
SPL	Sound Pressure Level
SQP	Sequential Quadratic Programming
TCS	Turbulence Control Screen

Symbols

(x, y, z)	Cartesian coordinate system
(r, θ, z)	Cylindrical coordinate system
(R, ψ, θ)	Spherical coordinate system
ΔPWL	Liner insertion loss, *subscript*: $_{Awt}$, A-weighted
χ	Acoustic reactance, *superscript*: $'$, Non-dimensional
η	Absorption coefficient
ϕ	Velocity potential; *no subscript*: unsteady/acoustic component, *subscript*: $_0$, mean flow component, *superscript*: *, total unsteady component, $\tilde{}$: approximate solution
ρ	Fluid density, *no subscript*: unsteady/acoustic component, *subscript*: $_0$, mean flow component, $_s$, stagnation value, *superscript*: *, total unsteady component, $\tilde{}$: approximate solution
γ	Ratio of specific heats, C_P/C_V

ω	Angular frequency
Ω	Angular velocity
${A^p}_{mn}$, ${A^\phi}_{mn}$	Modal amplitude of mode (m, n); *superscript*, ^{p}, acoustic pressure, $^\phi$, acoustic velocity potential
A, B, C, D	Amplitude coefficients
$\mathbf{C}$	Acoustic damping matrix in FE formulation
C_P	Specific heat capacity at constant pressure
C_V	Specific heat capacity at constant volume
c	Sound speed, *no subscript*: unsteady/acoustic component, *subscripts*: $_0$, mean flow component, $_s$, stagnation value
d	Liner cell depth
f	frequency, *subscript*: $_{1/3}$, one-third octave centre, $_s$, shaft
$\mathbf{F}$	Forcing term
H	Rectangular duct height
I	Acoustic intensity
i	$\sqrt{-1}$
k	Acoustic wave number, *subscript*: $_z$ or $_x$, axial wave number, $_r$, radial wave number
$\mathbf{K}$	Acoustic stiffness matrix in FE formulation
l	Mass inertance
M	Mach number
$\mathbf{M}$	Acoustic mass matrix in FE formulation
m	Circumferential mode order
N_{mn}	Normalisation factor
$\mathbf{n}$	Unit vector perpendicular to a surface
n	Radial mode order
p	Pressure; *no subscript*: unsteady/acoustic component, *subscript*: $_0$, mean flow component,

	superscript: *, total unsteady component
P	Modal acoustic power, *subscript*: $_I$, incident, $_R$, reflected, $_T$, transmitted
R, r	Acoustic resistance, Non-dimensional acoustic resistance
S	Surface of the FE domain
t	Time
$\mathbf{u}$	Velocity, *no subscript*: unsteady/acoustic component, *subscript*: $_0$, mean flow component, *superscript*: *, total unsteady component
U_0	Uniform mean flow axial velocity
V	Volume of the FE domain
W	Weighting function
Z, z	Acoustic impedance, Non-dimensional acoustic impedance

Acknowledgements

Firstly, I am very grateful for the generous financial support of the Engineering and Physical Sciences Research Council (EPSRC), provided through the UK Engineering Doctorate Scheme, and the Rolls-Royce Noise Engineering department, through the University Technology Centre in Gas Turbine Noise at the ISVR.

My decision to undertake an Engineering Doctorate was driven by a desire to gain an insight, and apply academic research to real engineering problems faced in industry. With the great support and guidance of my academic supervisor Jeremy Astley and my industrial supervisor Andrew Kempton throughout the course of my study, I have been able to achieve these goals. For this, I am immensely grateful to them both. I would like to give special thanks to Rie Sugimoto responsible for developing B-induct and ANPRORAD, whose enthusiasm, help, advice and thoroughness have been absolutely invaluable. I would also like to thank Shahrokh Shahpar for his advice on using SOFT.

I would like to thank my examiners, Pierre Lempereur (Airbus France), and Phillip Joseph (ISVR), for the time they have kindly given up to appraise my work.

The research presented in this thesis has benefited from useful discussions with many individuals. These include, Pete Schwaller, Dave Tomlinson, John Coupland, Alan McAlpine, Paul Murray, Andy Keane, to name but a few.

Throughout the course of my EngD I have been privileged to meet many friendly people. To name a few, these are, Eugene Deane, Mahdi Azarpeyvand, Chris Brooks, Phil Mclaughlin, Claire McAleer, Chris Lowis, Chris Ham, Feargus Kewin, Jack Lawrence, Adrian Bocher, Deepesh Singh, Mahak, Samuel Sinayoko, Vincent Blandeau, Mike Kingan, Chris Powles, Prateek Mustafi, Adriana Salgado, Martina Dieste, Mattieu Gruber...the list goes on.

Finally, I would like to express my gratitude to my family especially my wife, for their priceless support, love and care during my EngD.

Iansteel Mukum Achunche, January 2010

Chapter 1

Introduction

1.1 Background

Over the last decade, the rapid growth in air travel has led aircraft noise to be an increasing nuisance to residents in the vicinity of airports. This has led to the implementation of certification requirements and stringent regulations to curb aircraft noise levels around airports during take-off and approach. Consequently, the noise problem poses a major threat to the continued expansion of air transport. In this light, the reduction of aircraft noise is vital to the the continued prosperity of the aviation industry and a key factor in the development of new aircraft.

In order to counter this global noise problem, governmental organisations such as the International Civil Aviation Organization (ICAO) [6], has set noise requirements for aircraft to operate in its member states. In addition to the ICAO requirements, commercial aircraft are often required to meet local noise restrictions [7]. Such stringent noise legislation encourages research to reduce aircraft noise. In addition to noise legislation, research into reducing aircraft noise is also encouraged by initiatives proposed by non-governmental industry led organisations such as, the Advisory Council for Aeronautics Research in Europe (ACARE) [8] which has set a target of a 10 dB reduction in aircraft noise between 2000 and 2020. To achieve this goal, the sources of aircraft noise would

have to be identified after which, novel noise reduction techniques can be implemented.

In the noise certification requirements for aircraft issued by ICAO in Annex 16 [6], the metric used to quantify aircraft noise is the 'Effective Perceived Noise Level' (EPNL) measured in dB. EPNL is a noise measure, which is a single number evaluator of the subjective effects of aircraft noise on human beings.

In order to verify that an aircraft entering into service meets the ICAO noise requirements, the EPNL for the aircraft is calculated from noise measurements taken at three certification points. One of the certification points is below the flight path, when the aircraft is coming in to land (approach condition) at a distance of 2000 m from the runway threshold. The other two points are at take-off, one along a side line 450 m from and parallel to the extended runway centreline when the aircraft is climbing at full engine power (sideline or lateral condition), and the other is directly under the flight path at 6500 m from brake release when the engine power is cut back to about 80% of full power (cut-back condition).

1.2 Aircraft noise sources

The two main sources of aircraft noise are airframe noise and engine noise. The generation of noise in modern turbofan engines comes from a number of components. These are: the fan, the compressor, the combustor and the turbine (see Figure 1.1). During the operating cycle of a turbofan engine, the rotating fan ingests air into the engine. Some of this air goes through the core of the engine and the rest is funneled around the core of the engine through the bypass duct. The ratio of the air mass flow rate through the bypass duct to the air mass flow rate through the core of the engine is defined as the bypass ratio of the engine. The air that goes through the core of the engine is compressed in various stages in the compressor. The compressed air is then mixed with fuel in the combustor and burnt, after which it expands through various stages in the turbine, driving the latter which in turn drives the fan and compressor through a shaft. The hot air is then expelled from the rear of the engine as an exhaust jet.

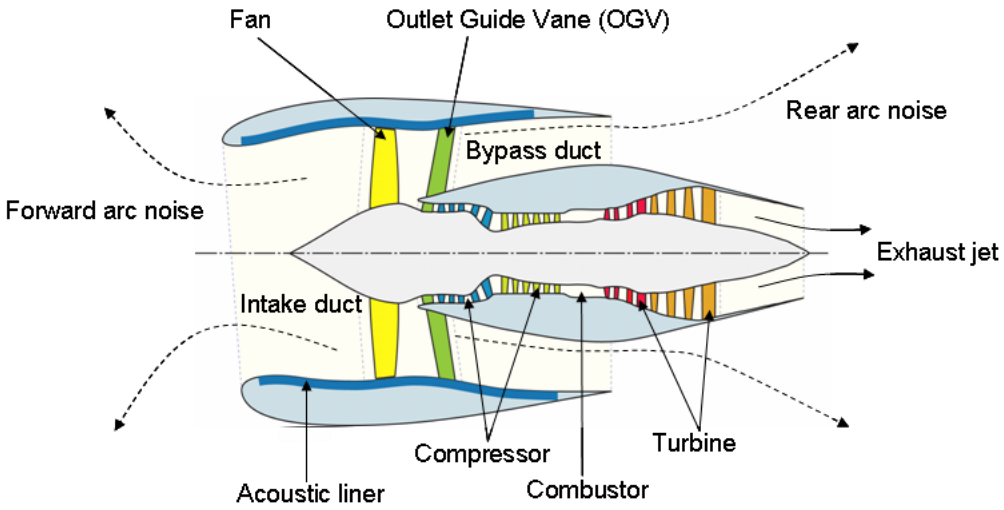

Figure 1.1: Modern turbofan engine showing main components and noise radiation through intake and bypass ducts.

As a result of these mechanisms, the major sources of aircraft noise include jet mixing noise, fan noise, turbine noise, combustor noise, compressor noise and airframe noise. Over the past forty years the noise contribution from each of these sources has changed as commercial turbojets (Figure 1.2(a)) evolved to high bypass ratio turbofan (Figure 1.2(b)) engines. This change in balance between the different noise sources is reflected in a change in the directivity and magnitude of the radiated sound power. In aircraft with modern turbofan engines, the dominant noise sources at take-off are jet noise and fan noise, and at approach, the dominant noise sources are airframe and fan noise. Typical noise source contributions for a commercial aircraft powered by a high bypass ratio turbofan engine are illustrated in Figure 1.3(a) for the take-off condition and in Figure 1.3(b) for the approach condition.

This thesis will focus on engine noise contributions to EPNL at take-off and approach and, more precisely on fan noise which is a dominant noise source at these conditions. Fan noise is composed of tones which are superposed on a broadband noise floor generated by turbulent unsteady flow over the fan and Outlet Guide Vane (OGV). The tones occur at discrete frequencies which are harmonics of the Blade Passing Frequency (BPF, 2BPF,

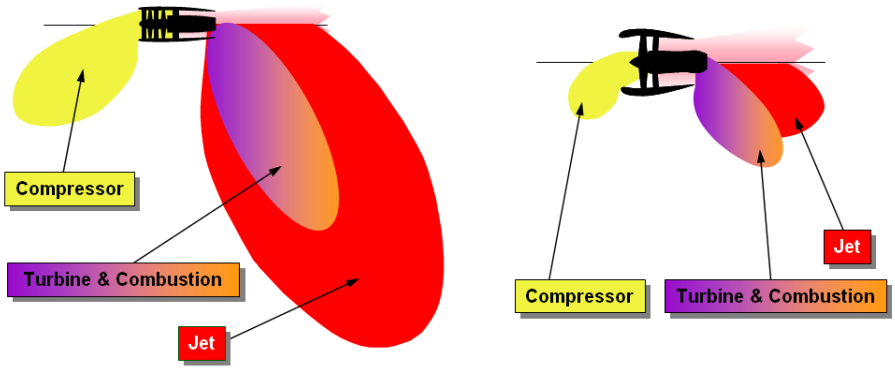

(a) Typical 1960s design. (b) Typical modern design.

Figure 1.2: Engine noise sources for a typical 1960s design and a modern design [2].

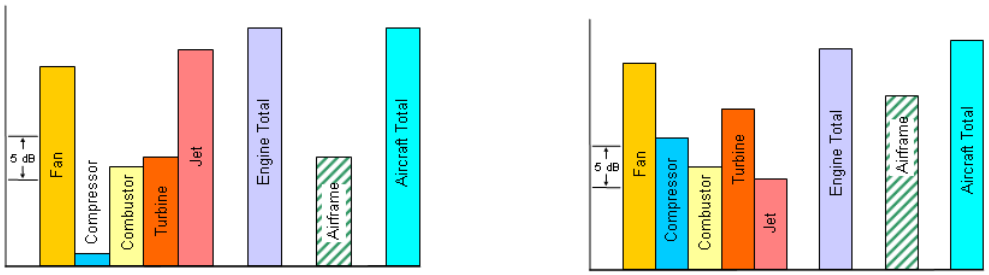

(a) Take-off (b) Approach

Figure 1.3: Aircraft noise sources relative power levels at take-off and approach [2].

3BPF etc) at subsonic and supersonic fan tip speeds but propagate more effectively in the latter case. At supersonic fan tip speeds buzz saw tones are generated at multiples of the shaft rotation frequency due to blade to blade differences in blade stagger angle.

Fan noise can either propagate into the forward arc through the intake or into the rear arc through the bypass duct as shown in Figure 1.1. The use of acoustic treatment within the intake and bypass ducts is a very effective way of reducing fan noise. Usually, duct walls are treated with acoustic liners (see Figure 1.1). Engine tests and rig tests can be used to assess the effectiveness of acoustic liners in intake and bypass ducts on radiated noise. However, noise tests are expensive and time consuming. Alternative methods for predicting the effect of noise treatments are required in the preliminary engine design phase to reduce the cost of improved quieter designs.

1.3 Motivation, aims and original contributions

The research presented in this thesis, was carried out within the Engineering Doctorate (EngD) program, and is performed in collaboration with Rolls-Royce. It has involved exploiting current prediction methods for turbofan noise. The advancement in aeroacoustics over the past decade has led to the commercialisation and availability of several computational techniques that can be used for predicting sound propagation and absorption in engine ducts, and radiation into the far field. Computational models capture the effects of a realistic geometry and flow, which are not represented in idealised analytical models commonly used in industry. In this thesis, a commercial Finite Element (FE) code ACTRAN/TM [9] and two shell programs B-induct and ANPRORAD developed at the ISVR are used to perform noise predictions for bypass and intake ducts. B-induct and ANPRORAD are shell programs which provide an automatic pre-processing and post-processing capability around ACTRAN/TM, for bypass and intake applications respectively. This automatic capability reduces the time required to perform bypass and intake predictions. The aim of this research is therefore to utilize these methods to gain an understanding of the fan noise problem, and to develop techniques based on these methods for performing

calculations in acceptable industry timescales, that can be implemented within the design process for quieter engines.

In order to confidently use a method in the engine design process, a thorough assessment and validation of the method is required. This usually involves validating the method against experimental data. For the bypass duct problem, the B-induct shell program has been assessed against experimental data by McAleer [1]. In this thesis, to further exploit the B-induct model, the latter is integrated within an in-house Rolls-Royce optimisation suite SOFT, developed by Shahpar [10], and is used to optimise the impedance of bypass duct liners. With the effectiveness of liners in reducing fan noise, an automated liner impedance optimisation process will provide an efficient method for the design of quieter engines.

In the intake problem, the work in this thesis focuses on using in-duct measured data to describe the fan noise source. The source representation is then used within the ANPRORAD model to perform predictions which are validated against experimental rig and engine data. The aim of this study it to formulate and demonstrate a robust methodology that can be used in future engine projects to perform accurate noise predictions at different engine conditions.

In addition to performing noise predictions, the ANPRORAD model is also used to investigate the effect of the intake geometry on low-frequency acoustic reflections within the intake, which affect fan blade stability. ANPRORAD has also been integrated within SOFT to automatically optimise the impedance of low-frequency liners to minimise the amplitude of acoustic reflections.

1.3.1 Original contributions

1.3.1.1 Integration of B-induct within SOFT

- The validation of a SOFT optimisation search strategy fully and partially for single and double liner impedances respectively.

- Automated impedance optimisations to assess the performance of different liner configurations in a uniform bypass duct, with the objective of maximising the liner insertion loss for a single frequency source.

- For multiple impedances, the automated approach is used to investigate the difference between optimising impedances simultaneously and, in turn (one after the other).

- The development of an integrated A-weighted liner insertion loss cost function ΔPWL_{Awt} at one-third octave centre frequencies from 0.5-10 kHz (as a computationally cheaper option to EPNL) to perform automated impedance optimisations for a uniform bypass duct.

- The validation of an automated impedance optimisation using a real bypass duct geometry and ΔPWL_{Awt} cost function, and comparison to results obtained by McAleer [1] using the same geometry and an EPNL cost function, (highlighting viability of the ΔPWL_{Awt} cost function in real applications).

1.3.1.2 Assessment of ACTRAN/TM and ANPRORAD as a viable methodology for intake noise predictions in industry

- Use of in-duct measured data from a circumferential array of pressure transducers to calibrate source levels and absolute levels for input into the ANPRORAD model to accurately predict far field Sound Pressure Level (SPL) field shapes.

- Demonstration of the dependence of far field hard-walled SPL field field shapes and liner attenuations on broadband modal power distribution.

- Benchmarking of ANPRORAD predictions (using source description derived from in-duct hard-walled measured data), against experimental rig and engine data for lined intakes at a range of fan speeds, for tone and broadband noise.

1.3.1.3 The use of ANPRORAD as a prediction tool to investigate the effect of intake geometry and fan speed on low-frequency acoustic reflections

- Demonstration of the effect of intake geometry and fan speed on the amplitude of low-frequency acoustic reflections from low order incident modes.

1.3.1.4 The integration of ANPRORAD within SOFT for low-frequency liner optimisation

- The automated impedance optimisation of a low-frequency liner to minimise the amplitude of the acoustic reflection from a low order incident mode.

1.4 The EngD scheme

The EngD scheme is a four year doctoral program which involves a significant taught technical and management component. This scheme promotes the close collaboration between research in academia and industry, hence requiring an industrial sponsor. The aim of this scheme is to resolve problems of industrial interest. The student acquires management experience and gains an insight into research and development in an industrial context.

The EngD program reported in this thesis is carried out in collaboration with Rolls-Royce. The sponsor's main objective was, to develop an efficient methodology for bypass duct liner impedance optimisation for future engine designs, and to demonstrate an intake prediction tool that can be used to accurately model the noise source and the propagation into the far field. These tasks were undertaken in parallel to meet industry timescales.

1.4.1 Planning and progress

Over the course of the EngD program, the author was based either at the Institute of Sound and Vibration Research (ISVR) or, at the Noise department in Rolls-Royce. A

work plan is provided in Figure 1.4[1] which shows the tasks undertaken, and the time spent between the university and the company. Review meetings between the author, the academic supervisor and the industrial supervisor were held quarterly to assess the work progress and to plan future tasks.

The tasks performed during the EngD program have been varied but closely related. They range from the development of an efficient tool for automatic liner impedance optimisation for bypass ducts through the integration of B-induct within SOFT, to exploiting the capabilities of ANPRORAD to be used as a viable methodology for intake noise predictions. The capabilities of ANPRORAD have also been exploited to be used as a 'Stage 1' model for fan blade stability analysis. ANPRORAD has also been integrated within SOFT to perform automatic low-frequency liner impedance optimisations with the objective of minimising acoustic reflections that may affect fan blade stability [2].

1.5 Outline of contents

This thesis is divided into nine chapters. In Chapter 2, a literature review is presented of prediction methods for aeroacoustics, of optimisation techniques, and of material on liner optimisation.

In Chapter 3, the in-house Rolls-Royce optimisation suite SOFT is introduced. Noise related analytical model problems are integrated within the optimisation suite to demonstrate its application to acoustic problems, and an assessment of different optimisation methods is carried out.

Chapter 4 contains an overview of the propagation model used within B-induct. A

[1]Some aspects of this work, such as the assessment of the HYDRA CFD code, and the details of the integration of B-induct within SOFT, were reported in the author's mini-thesis [11] but are not reported in this thesis.

[2]The author presented the automated liner impedance optimisation tool for bypass ducts, at an Aerodynamic Design and Optimisation Seminar at Rolls-Royce. The ANPRORAD methodology was advanced to the next Technology Readiness Level when presented to the Critical Capability Acquisition Review panel at Rolls-Royce.

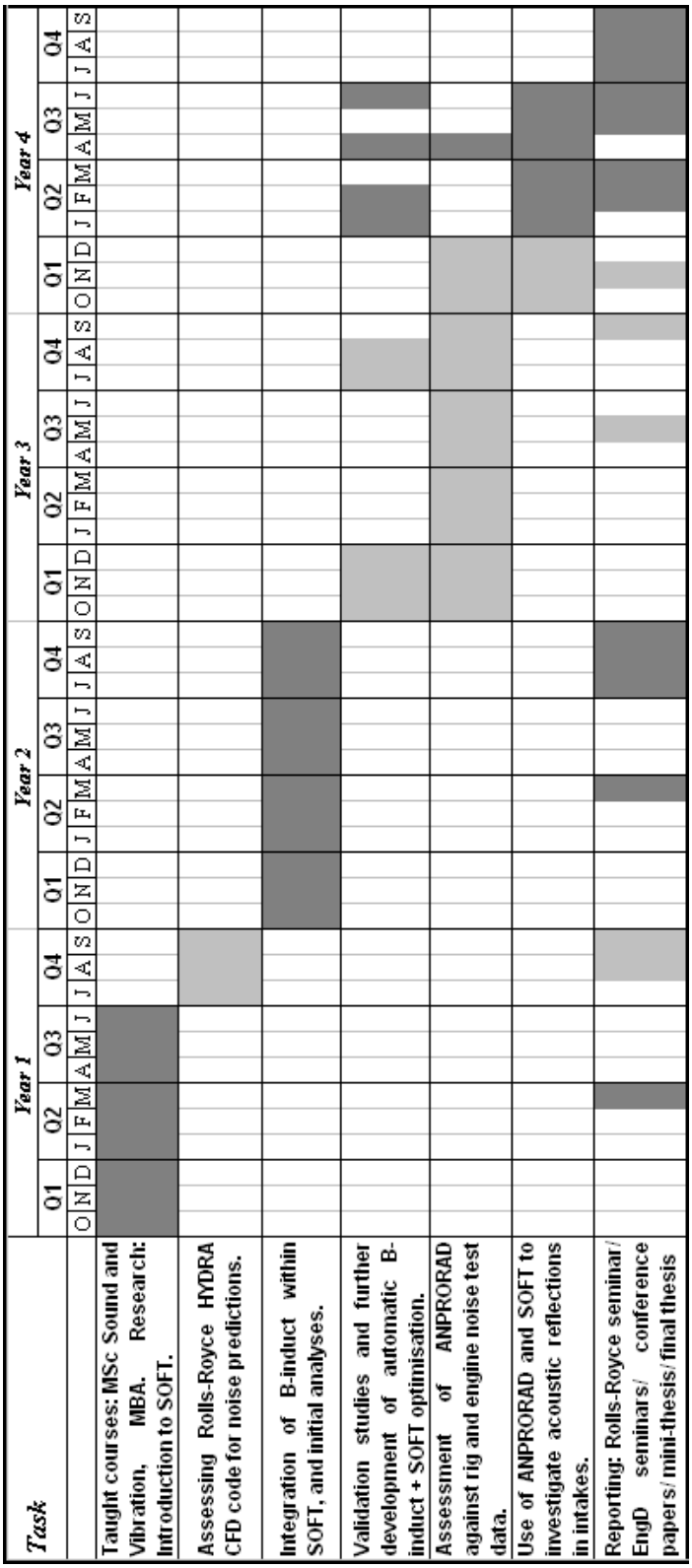

Figure 1.4: Work plan. Tasks in dark grey are carried out at ISVR and tasks in light grey are carried out at Rolls-Royce.

number of automated liner impedance optimisations for a uniform bypass duct using B-induct within SOFT is then presented. The optimisations are performed to maximise the liner insertion loss in the duct, for single and multiple impedance segments using single and multi-frequency sources. In this chapter an A-weighted insertion loss cost function is introduced which is used in Chapter 5 to perform a liner impedance optimisation for a real bypass geometry. Results from this study are benchmarked against results from an EPNL optimisation.

In chapter 6 an overview of fan noise, and a summary of the methods used in this thesis to predict its propagation in the intake and its radiation into the far field are presented. In chapter 7 the validation of the ANPRORAD intake model using rig and engine noise data is detailed, making use in-duct measured data to describe the noise source and absolute levels for input into ANPRORAD. In Chapter 8, ANPRORAD is used to assess the effect of the intake on fan blade stability. An automatic impedance optimisation using ANPRORAD and SOFT is used, to minimise acoustic reflections.

In Chapter 9, overall conclusions and recommendations for future work are presented.

Chapter 2

Literature review

2.1 Introduction

Research in the field of aeroacoustics over the last two decades has enabled researchers to gain a significant understanding of noise generation by aeroengines. However, improved prediction methods and noise reduction technologies are still required if initiatives such as, the Strategic Research Agenda of the Advisory Council for Aeronautics Research in Europe (ACARE) [8] which targets a 10 dB reduction in aircraft noise for new aircraft entering service between 2000 and 2020 is to be achieved. In modern high bypass ratio turbofan engines, improved acoustic treatment within the intake, bypass and core ducts has been an effective way of reducing fan noise, one of the major sources of aircraft noise.

In the first section in this chapter the literature on analytical and computational methods for predicting sound propagation in aeroengine ducts and its radiation into the far field is reviewed. In the next section the literature on optimisation techniques including local and global optimisation algorithms as well as alternative optimisation methods, for subsequent application to liner design are reviewed. In the final section in this chapter the literature on liner optimisation techniques to reduce aircraft noise, is examined. The key design parameter is the acoustic impedance of the liner. The impedance comprises of a real resistive part responsible for removing energy from the acoustic wave and converting

it to other forms, and an imaginary reactive part that represents the ability of air to store the kinetic energy of the acoustic wave as potential energy due to its compressibility.

2.2 Prediction methods for aeroacoustics

The term aeroacoustics is used to describe the generation and propagation of sound in a moving flow. The aeroacoustic sound field radiated by a turbofan engine can be characterised as flow noise or interaction noise. Flow noise is generated by unsteady motion far away from bounding surfaces, whereas interaction noise is generated from the interaction of unsteady flow with stationary or moving objects. In aeroengines, jet mixing noise is an example of flow noise, whereas fan noise is dominated by interaction noise. Methods that exist to predict aeroengine noise broadly fall into two categories: analytical methods and computational methods. Both are heavily dependent on calibration by measured data.

In the study presented in this thesis, the focus is on the propagation of sound in moving flows. Hence, the methods presented in the subsequent sections deal with modelling fan noise propagation into the far field, and not its generation.

2.2.1 Analytical methods

Analytic methods for fan noise propagation were first developed in the 1960s and 70s. Many are based on the description of the sound field in aeroengine ducts in terms of acoustic modes, following the pioneering work of Tyler and Sofrin [12]. They are generally applied to axisymmetric cylindrical (intake) and annular (bypass) geometries. Also, in these methods the source is considered to be known and independent of the propagation and radiation models. Such methods include, lined duct eigenvalue solutions for sound absorption, mode matching, ray tracing techniques and radiation models such as the Wiener-Hopf solution for cylindrical and annular ducts for sound radiation.

Mode matching which involves matching modes in different lined segments of a uniform duct, was first used by Lansing and Zorumski [13] to investigate the effect of impedance

discontinuities on sound transmission through ducts. In ducts where impedance discontinuities exist, acoustic scattering can be caused by the change in the impedance. In addition, the sound field in each impedance segment can be expressed in terms of modes, hence mode matching schemes are very useful in the practical design of liners. Examples of their application in the optimisation of axially segmented liners are given in references [14–18]. Most mode matching schemes match the pressure and axial velocity at the matching planes where impedance discontinuities exist. McAlpine *et al.* [14] used this formulation to optimise the impedances of adjacent liner segments. This was achieved by minimising the scattering of acoustic energy (at supersonic fan tip speeds) into the first radial mode which is the least attenuated mode. One of the disadvantages of this formulation is that it does not predict the large wall pressure fluctuations present at liner discontinuities. Astley *et al.* [19] have proposed an alternative mode matching formulation including additional terms to deal more accurately with axial impedance discontinuities. This formulation is used by Brooks [17] to calculate the sound transmission in ducts with different shear flow profiles. The results show that with a linear shear flow profile, significant effects of sound refraction are obtained due to the fact that the refraction is not only limited to the boundary layer at the duct wall. In as much as mode matching schemes play an important role in practical liner design in aeroengine ducts, they can require considerable computational effort at high frequencies. In addition, at high frequencies where many modes are present, identifying and tracking modes can be very difficult. In such cases, a simpler approach such as ray acoustics can be used.

Ray acoustics is a high frequency approximation in which when the acoustic wavelength is much smaller than the inhomogeneity of the flow, the acoustic waves can be likened to particles moving through the fluid (like rays in optics). Kempton [20–22], Tester [23, 24] and Boyd *et al.* [25] have investigated ray acoustics models for duct acoustics. In reference [21] Kempton compared measurements and intake liner predictions using ray theory and mode theory, and showed a good agreement. He concluded that diffraction and interference effects were required to improve the ray theory approach. In the study by Boyd *et al.* [25], taking these effects into account gave a good agreement between ray

theory predictions and other results for a two-dimensional duct with no flow. When ray acoustics is used, the correct prediction of the diffraction of sound waves around duct edges and corners requires the use of, methods such as the geometric theory of diffraction (GTD) [26] studied by Chapman *et al.* [27, 28]. Ray acoustics models are useful in duct acoustics because they are computationally inexpensive and robust. They can readily be applied to complex duct geometries, but require the addition of GTD or some other technique to model diffraction correctly.

In aeroengines, the prediction of the liner attenuation of sound propagating through intake and bypass ducts is required. This leads to the need to calculate eigenvalue solutions to obtain the imaginary part of the axial wave number and hence the attenuation for lined ducts. However, the determination of lined duct eigenvalues is non-trivial. Several methods have been used to calculate lined duct eigenvalues. A review of some these methods can be found in reference [29]. More recently, Brooks [30] calculates eigenvalues for a lined rectangular duct by using the rigid duct eigenvalues as initial values, and then using numerical integration and iteration techniques to obtain the lined duct eigenvalues.

With regards to estimating the far field noise radiated from aeroengine ducts, the description of a sound field in terms of acoustic modes provides a convenient way of defining the radiated sound field within the duct using analytical models. Homicz and Lordi [31] derived exact theoretical expressions for the modal sound radiation from a semi-infinite, hard-walled, unflanged circular duct, including extensions that consider mean flow and an annular duct. Rice [32, 33] extended ideas of modal cut-off ratio to the radiation problem and derived approximate expressions for the radiated sound field as functions of the modal cut-off ratios of the duct modes. In reference [32] Rice derived an explicit equation for multimodal radiation patterns from a flanged cylindrical duct. The multimodal radiation pattern is obtained from contributions for single mode radiation patterns, and for arbitrary power distributions in the modes. More recently, Joseph and Morfey [34] used an approach similar to Rice's [32] to obtain the multimodal radiation pattern from an unflanged cylindrical duct, proposing a weighting function based on physical source models rather than using empirical weighting functions. With the exception of the method by

Homicz and Lordi [31], the methods examined so far do not include mean flow effects. The inclusion of mean flow effects can make modelling realistic duct flows very challenging.

Gabard and Astley [35] have derived an exact solution that describes the sound field radiated from a semi-infinite axisymmetric annular duct with a subsonic jet. The exact solution takes into consideration both a variable jet and free stream velocity, and an infinitely long centre body. This work is an extension to the original study performed by Munt [36, 37] who considered a semi-infinite hollow cylinder in which the inner and outer mean flows had different Mach numbers, and Rienstra [38] who used the Wiener-Hopf method to derive the general solution for a semi-infinite duct with an infinite centre body, and uniform flow across the jet and bypass streams.

Gabard and Astley [35] applied their analytical model to study the effect of the ambient Mach number, the centre body and the shed vorticity (obtained by satisfying the Kutta condition which requires the pressure to be finite at the lip of the duct) on sound radiation. The noise source used was a multi-mode 'broadband' source represented by uncorrelated modes with equal power in each mode. Considering the directivity patterns of single modes, as the Mach number of the ambient stream decreases, the refraction produced by the vorticity mismatch across the vortex sheet increases thereby shifting the lobe of the directivity patterns away from the jet axis. This creates a cone of silence between the first lobe and the jet axis. The directivity pattern for multi-mode 'broadband' sources do not have lobes [35], since the summation over all the cut-on modes smooths the curve which will otherwise have peaks and troughs for single modes. The effect of the centre body was investigated by varying the hub to tip ratio. For low order modes, a reduction in the hub to tip ratio causes more radial modes to propagate, hence an increase in the number of lobes in the directivity pattern. For higher order modes the same trend is observed to a lesser extent. For equal power broadband modes there is no general trend in the radiation pattern as the hub to tip ratio varies. Examining the effect of shed vorticity from this theoretical model shows that the latter has no effect on the main lobe of the directivity pattern. However, in the rear arc, as the amplitude of the vorticity increases and its phase reduces, the sound pressure level increases. The vorticity

shed has a negligible effect on the directivity pattern of a broadband multi-mode source.

2.2.2 Computational methods

Over the last decade, Computational Aeroacoustics (CAA) methods have been developed in parallel with the more established Computational Fluid Dynamics (CFD) methods. CAA methods must deal with computational issues which are often not present in CFD [39]. Acoustic waves have small amplitudes compared to the mean flow, and hence to compute the sound field accurately, the numerical scheme must have low levels of numerical dissipation and dispersion. This is particularly important in aeroengine ducts where there is a general interest in the radiated sound field and an accurate far field solution is required.

While CAA methods used for modelling the generation of noise in aeroengines include non-linear models [40], such as Direct Numerical Simulation (DNS), Large Eddy Simulation (LES) and Reynolds Averaged Navier-Stokes (RANS) calculations, propagation models are usually based on the numerical solution of simpler inviscid equations such as the linearised or full Euler equations.

In this thesis, the focus is on numerical solutions of the Linearised Euler Equations (LEE). These can be obtained either in the time domain or the frequency domain. Time-domain solutions provide directly a full range of space-time data as opposed to frequency-domain methods which can only provide results at a single frequency. Time-domain and frequency-domain approaches commonly used in propagation models are described below.

Time-Domain Linearised Euler Equations (LEE) Methods

Solutions of the LEE can be applied to problems with either rotational or irrotational mean flows and are hence suitable both for intake and exhaust flow problems. However, the use of a time domain solution of the LEE triggers Kelvin-Helmholtz instabilities [41] when shear flow is present, as in the case of propagation through an exhaust flow. Numerical methods used to solve the LEE in the time domain can either be called structured

or unstructured depending on the type of grid which is used. Structured methods are generally easier to implement numerically than unstructured methods. However, unstructured methods are better for modelling complex geometries. Zhang *et al.* [42] have used a structured high-order compact scheme to solve the LEE to calculate the wave propagation and diffraction through intake and exhaust flows. In order to suppress shear layer instabilities in the case of exhaust flows, they removed the mean shear terms in the LEE which are responsible for the Kelvin-Helmholtz instabilities in the propagating sound field, and assume that this will not significantly reduce the accuracy of the solution. Richards *et al.* [43] have applied the same method to an intake problem including three-dimensional swirling mean flow effects, as well as the effect of an acoustic liner modelled using a time domain impedance boundary condition formulated by Ozyoruk *et al.* [44]. Other structured methods include, high-order, Dispersion Relation Preserving (DRP) finite difference methods [39]. This method of discretisation leads to a preservation of the dispersion relation so that different phases of an acoustic wave propagate with the same group velocity. For complex geometries, the generation of a good quality structured mesh can be a challenging exercise. To address this problem, overlapping (Chimera) grids can be used. This technique has been implemented by Schoenwald *et al.* [45, 46], based on the DRP scheme [39].

Unstructured grids are however, highly desirable for complex geometries. Unstructured, high-order, Discontinuous Galerkin Methods (DGMs) [47–49] have been used for such applications. These methods use finite elements with a discontinuity of the numerical solution at each element interface. Their adaptive spatial order gives a high order model with good dispersion characteristics and gives the user more flexibility in the mesh generation process than the structured methods mentioned previously.

Frequency-Domain Linearised Euler Equations (LEE) Methods

The Kelvin-Helmholtz instabilities that occur in the time-domain LEE solutions for sheared mean flows can be avoided by assuming a time-harmonic response and solving the LEE in the frequency domain, as shown by Agarwal *et al.* [41]. Zhao and Morris [50] devel-

oped a frequency-domain method to solve the LEE. The technique used is the Streamline Upwind Petrov Galerkin (SUPG) method [51, 52]. This is a continuous finite element (FE) method which can be applied to several mean flows. Similarly, Ozyoruk [53] developed a frequency-domain finite difference code (FLESTURN) based on a high order finite difference approach, for predicting the radiation of turbofan tones both for intake and exhaust problems. The LEE in the frequency domain must however be solved by using a direct matrix solver. Ozyoruk [53] has used the MUMPS direct sparse solver in a parallel implementation. In his model, the geometry is assumed to be axisymmetric.

Full Euler Equations Methods

The full Euler equations can also be used as the basis for numerical solutions of the propagation problem. Obtaining the solution of the full Euler equations avoids the problem of Kelvin-Helmholtz instabilities which occur in linear time-domain schemes for sheared mean flows, and enables accurate modelling of non-linear acoustic scattering and shock waves in aeroengine ducts. Redonnet *et al.* [54] solve the full Euler equations to obtain the aft radiated fan noise through a realistic exhaust geometry which includes the effect of the pylon and internal bifurcations. The code used (*sAbrinA.v0*) developed by ONERA[1] , uses a high-order finite difference scheme for the spatial discretisation and a Runge-Kutta time-marching scheme. This is a more computationally demanding approach than the solution of the linearised equations but current computing times are acceptable for one-off studies. Ozyoruk and Long [55] developed a three-dimensional Euler solver and applied it to radiation problems for realistic intake geometries. This method has the capability of modelling non-uniform background flow effects, as well as high amplitude non-linear effects which occur close to the fan at high power settings.

[1]Office National d'Etudes et de Recherches Aéronautique.

Frequency-domain methods for irrotational mean flows - the convected Helmholtz equation

In aeroengine ducts at modest power settings where non-linear effects are less significant, the propagation problem can be satisfactorily modelled by the numerical solution of the Linearised Euler Equations. This problem is simplified in the intake where the mean flow is largely irrotational, and the propagation problem can be formulated in terms of a convected wave equation in the acoustic velocity potential. This problem can be solved numerically in the frequency domain. High-order Finite and Infinite elements (FE/IE) [56–59] are commonly used. This approach is implemented in a number of commercial codes such as ACTRAN/TM [9], where infinite elements are used to directly compute the far field solution as part of the near field solution. ACTRAN/TM is used extensively in this thesis within two shell programs, B-induct [4] for bypass ducts, and ANPRORAD[2] for intake ducts [60, 61]. The details of these shell programs are discussed later on in this thesis.

Sugimoto *et al.* [62–65] have used B-induct to predict the propagated and radiated sound fields in hard-walled and lined bypass ducts and validated the results with measured data. In these studies, the effects of flow and three-dimensional geometry effects on sound propagation and radiation have also been investigated. In a detailed geometry study, McAleer *et al.* [66] use B-induct to investigate the effect of the curvature of the bypass duct on the radiated sound field. It was established that a shorter and more curved bypass duct can provide a similar insertion loss benefit to a typical bypass duct with a greater liner area.

Boundary element methods

Boundary element methods (BEM) are commonly used for intake problems [67, 68], however they are restricted by assumptions of uniform or zero mean flow. The boundary element method is a numerical technique where in the governing equation in a problem

[2]Developed within a collaborative partnership between the ISVR and IHI Corporation.

domain is transformed into a surface integral equation over the surface that bounds the problem domain. The surface integral equation is then solved by discretising the surface into smaller segments called boundary elements. One advantage of the boundary element method over the finite element method (FEM) is that the discretisation occurs only on the surface rather than over the entire problem domain. For three-dimensional problems especially, the BEM results in a very much smaller problem size, but the coefficient matrix is full and the computational cost is not necessarily smaller than for comparable FE models. On the other hand, use of the BEM introduces issues associated with non-unique solutions for exterior problems, and the surface integral equations require the integration of singular terms.

Lidoine *et al.* [67] have used a BEM to investigate the effects of scattering and the presence of flow in realistic intakes. The BEM was validated with an analytical method based on mode theory and the Wiener-Hopf's technique. Montetagaud and Montoux [68] use a BEM to assess the acoustic performance of a negatively scarfed intake at low frequencies, and validate the results using measured data from rig tests.

2.3 Optimisation techniques

In this section, an overview of optimisation techniques is summarised. A more detailed exposition of the optimisation techniques presented here can be found in, 'Computational Approaches for Aerospace Design' by Keane and Nair [69].

Optimisation is the process of finding inputs $\mathbf{x}$ $(x_1, x_2, ...)$, that give the maximum or minimum value of an output $f(\mathbf{x})$, subject to constraints. Constraints are conditions that solutions to an optimisation problem must satisfy, they can either be inequality or equality. For example, given the problem to maximize $f(\mathbf{x}) = x_1 + x_2^3$ subject to $x_1 \geq 1$ and $x_2 = 2$, $x_1 \geq 1$ and $x_2 = 2$ are inequality and equality constraints respectively. Optimisation will generally use numerical techniques to find such values (optima). Problems can be differentiated based on the nature of the input, the nature of the output and the relationship between the input and output functions. The inputs can either be numeric or

non-numeric. If the input is non-numeric, the optimisation process becomes an optimal selection. Numeric inputs can be further classified into discrete or continuous. Discrete input values can only take a given set of values, such as the number of blades on a fan, meanwhile continuous input values can take any value within a given range, such as liner depth.

Distinctions can also be made based on the nature of the output. There can either be a single objective function to be minimised or maximised or there can be multiple objectives, in which case a weighting can be applied between the objectives. Problems can also be differentiated based on the functional relationship between the inputs and the outputs, which can either be linear, non-linear or discontinuous. Linear relationships can give efficient solutions using linear programming techniques, meanwhile discontinuous relationships can make the optimisation process difficult. However, in most aerospace applications such as noise optimisation, non-linear relationships are common [69]. In this regard, this section focuses on non-linear optimisation methods.

Non-linear optimisation methods cover a very broad field and can be divided into three main themes [69]: the classical hill climbers of the 1960s, the evolutionary approaches of the late 1970s and response surface modelling of the 1980s and 1990s. Each of these methods can be fitted into a general optimisation sequence which comprises of sampling, fitting, exploring and exploiting. These categories are summarised in the sub-sections which follow.

2.3.1 Hill climbing methods

Hill climbing methods seek to move 'uphill' or 'downhill' on the cost function surface in the direction of a maximum or minimum value for the cost function. The two basic issues these methods have to deal with are, the direction in which to move and the step size to take. To determine the direction in which to move, they could either use the local gradient (gradient-based methods) or intelligent guesses (pattern or direct searches). In this thesis, the focus is on gradient-based methods.

Gradient-based methods use gradient information to identify the direction of steepest descent or ascent in order to move in that direction. Methods of evaluating gradients are commonly based on the idea that in the vicinity of an optimum point in two-dimensions, the function is an ellipsoid and can thus be approximated by a quadratic function. An example of such a method is sequential quadratic programming (SQP) [70,71] in which a cost function F is represented by a quadratic function. In the general problem, $F = (1/2)\, X^T H X + C^T X + \alpha$, where X is a vector with input variables x_1, $x_2 ... x_n$, H is a symmetric matrix called the Hessian, C is a vector of constants and α is a scalar constant. The idea is to find input variables x_1, $x_2 ... x_n$, such that F is a minimum, so that its gradient G is zero, $G = HX + C = 0$ which implies $X = -H^{-1}C$. Values of the Hessian are estimated using the evaluation of the cost function from the initial value. Successive evaluations are then used to improve the Hessian matrix.

Another example of a gradient based method is the dynamic hill climbing (DHC) method of Yuret and de la Maza [72] which is used for many of the optimisations performed in this thesis. The DHC method comprises of an inner loop and an outer loop. The inner loop consists of an efficient hill climbing technique for locating local optima and the outer loop focuses the inner loop to search random regions of the design space so that the design space is well explored. When the algorithm within the inner loop converges, the inner loop exits and the outer loop re-initialises the inner loop with a randomly chosen starting point. In the hill climbing technique, for an n-dimensional problem, the inner loop maintains a list of $2n$ vectors $\vec{v}$, n of which form an orthogonal basis set for the search space and the other n are the negations of these vectors. Also included are two additional vectors called gradient vectors that are functions of the last two directions the algorithm has moved in. These are required to track the curvature of the design space.

The list of vectors (including the gradient vectors) is used to determine the next evaluation point in the DHC algorithm. Starting from a current point $\vec{x}$, the function f is evaluated at a new point $\vec{x} + \vec{v}_i$, where $\vec{v}_i$ is the vector with the largest magnitude. The value of the function f at the new point $\vec{x} + \vec{v}_i$ is then compared to the value of the function at the current point $\vec{x}$. In a minimisation problem, if $f(\vec{x} + \vec{v}_i) < f(\vec{x})$, then

$\vec{x} + \vec{v}_i$ becomes the new point, and the process is repeated, again starting with the vector that has the greatest magnitude. If $\vec{v}_i$ is chosen twice, its magnitude is doubled. However if $f(\vec{x} + \vec{v}_i) \geq f(\vec{x})$, the magnitude of $\vec{v}_i$ is halved and the vector with the next largest magnitude is used. The algorithm continues to update the magnitudes of the vectors and the current point until if finds a point from which the function cannot be further decreased. This occurs when the magnitudes of all the vectors reach a minimum threshold set by the user. The random re-start capability of the outer loop in the DHC method provides a stochastic capability of the method which can be useful for functions with multiple peaks (multimodal functions). The next section examines stochastic methods in a bit more detail.

Gradient-based methods are generally very efficient when dealing with smooth functions. However, when the function is not smooth (noisy), gradient-based methods need to be used carefully since step sizes need to be chosen so that, they are larger than any spurious oscillations in the function.

2.3.2 Stochastic and evolutionary methods

These are methods which seek to find the global optimum through the use of random number sequences to sample the design space. Consequently, they are able to accept poor designs in the search of improved designs. Commonly used stochastic and evolutionary methods include simulated annealing (SA) [73] and genetic algorithms (GAs) [74].

Simulated annealing (SA) first introduced by Kirkpatrick *et al.* [73] in the 1980s is a random search algorithm that mimics the principle of statistical thermodynamics where by the atoms in crystalline structures take up minimum energy states if cooled sufficiently slowly from a high temperature T. In this method, the cost function is mapped to the energy level E at a given temperature T, and the configuration of the atoms is mapped to the design variables. The aim of this process is therefore to obtain the configuration of atoms that gives a minimum energy level E [73].

At each evaluation in the algorithm, the current configuration is replaced with a new

random configuration if the latter is better. If the new configuration is worse, it still has a chance of being chosen with a probability that depends on the energy level E and the temperature parameter T that is gradually decreased during the process. The dependency is such that the current solution changes almost randomly when T is large, but increasingly accepting only a better design as T tends to zero. This allowance for accepting poorer designs at large T prevents the method from becoming stuck in local optima.

Genetic algorithms (GAs) [74] are random search algorithms that emulate evolutionary ideas of natural selection and genetics. They iteratively transform a set of designs, known as a population (usually randomly generated), into a new population of hopefully improved offspring designs. In GAs, the design variables can either be mapped to binary code (binary-coded GAs) or to real numbers (real-coded GAs). The key concepts in GAs include fitness and crossover [74]. The fitness of a design is a classification of how good the design is with respect to other designs in a population as determined by the cost function. Using the survival of the fittest concept in natural selection, the designs in a population that are better than average, are more likely to contribute (through the process of crossover) to the next generation of designs. A simple way of choosing the designs to produce the next generation is by roulette wheel sampling [74] in which the selection of designs is random but dependent on their fitness. Having selected two designs for the next generation, a 'single point binary crossover' can be used in which information at a single point can be swapped between the binary encodings of two designs.

Other features used in GAs include mutation and elitism [74]. Mutation is a process whereby random changes are introduced into a design with the idea of exploring the whole search space. This is usually done by a random flip of a bit in a fixed length binary character string, the probability of this can be specified by the user. Elitism (preservation for the next generation) which has no biological analogy, ensures that the best designs are guaranteed survival to the next generation. This is to ensure that the optimisation process can benefit from gains it has made.

2.3.3 Response surface modelling

Response surface modelling is an optimisation technique that facilitates the tackling of complex and computationally expensive problems. It essentially replaces calls to an expensive computational code with a curve fit that aims to correctly represent the computed values. This process is twofold and the first stage is called design of experiment (DoE) in which data is generated using the real code to get information on the nature of the function. The second stage is a curve fit through the data to create an approximate surface (response surface). As part of the curve fit process, in order to obtain an accurate response surface, the DoE points may need to be updated and the response surface re-estimated until there is a converged solution between the real code and the approximated function. This optimisation technique can be fitted into a generic optimisation sequence which involves: data sampling (DoE), curve fitting (response surface), exploring (global search) and exploiting (local search).

Design of experiments originated from the need to design physical experiments such as agricultural analysis in the 1930s [75]. Consequently, classical DoE techniques were developed for laboratory and field experiments which are susceptible to random error and non-repeatability. In classical DoE techniques, sample points are usually placed at the bounds of the parameter space since these designs can offer a better overall trend of the design space in non-repeatable experiments. In computer simulations however, the results are not subject to non-repeatability issues and hence do not require the classical DoE techniques. A review article by Giunta *et al.* [76] presents DoE techniques appropriate for computer simulations. These include, Monte Carlo sampling, Latin Hypercube sampling and orthogonal array sampling.

The Monte Carlo technique was invented by Stanislaw Ulam (1946). Monte Carlo techniques use a random number generator to sample the design space, hence the need for a random number algorithm. Such a simple DoE technique generates sample points without taking into account previously generated sample points. Considering the use of a random number algorithm there is a possibility for some areas of the design space to be

densely sampled meanwhile other areas are sparsely sampled. Variants of the Monte Carlo technique include quasi-Monte Carlo sampling. This is implemented in the quasi-random sequence generator LPτ [77], which uses a minimum discrepancy algorithm to generate data points. The discrepancy of a design space is a measure of how much a distribution of design points differs from a uniform distribution. The LPτ method generates a deterministic sequence of points. Although these points are not uniformly distributed, they generally give a good spread over the design space.

Latin hypercube sampling (LHS) was invented by Mckay *et al.* (1979) as an alternative to Monte Carlo methods used in computer simulations. For a p - dimensional problem, the basic principle is to partition the range of each design variable into n bins of equal probability such that there are a total of n^p bins in the design space. Once the bins have been created, n samples are generated so that for each design variable there is only one value in each bin.

In orthogonal sampling [78], the design space is divided into equally probable subspaces. Each of the subspaces is then sampled simultaneously with equal density such that the entire design space is a latin hypercube sample. Orthogonal sampling therefore ensures that the randomly generated sample points have a very good spread over the design space.

Once the DoE points have been generated, the construction of a response surface is the next phase of the response surface modelling process. Two popular methods for constructing response surfaces are approximations based on, polynomial models and on radial basis functions.

In the case of polynomial response surfaces, first and second order models are most commonly used. This is because, in experiments where data generation is expensive and data points are few, linear and quadratic models work best [69]. However, in modelling complex input-output relationships, quadratic response surfaces for example will not be able to capture multiple peaks and troughs of the original function. Consequently, polynomial models are only useful in approximating input-output relationships in a small region of the design space.

Alternative methods for constructing response surfaces use basis functions which are more flexible when dealing with multiple peaks and troughs. One of these involves the use of radial basis functions. Radial basis functions are real valued functions whose value depends only on the distance from the origin, or some other arbitrary point called the centre. They have been developed for deterministic and random data interpolation. Commonly used radial basis functions include linear splines, cubic splines, multiquadrics, thin plate splines and Gaussian functions, details of which can be found in reference [79]. The choice of radial basis function will clearly depend on the nature of the function to be approximated.

More complex response surface modelling techniques include kriging [80], named after a South African mining engineer who first developed the method in the 1950s. Similar to the use of basis functions, kriging models are a generalisation of the Gaussian method. However, contrary to the Gaussian method in which the local character of the approximation is fixed, kriging methods have hyper-parameters than can be tuned to adjust the smoothness and the variation of the response surface over the design space.

2.4 Liner optimisation

During approach and take-off, fan noise is one of the dominant noise sources for a turbofan powered aircraft [50]. Fan noise and jet noise are dominant at take-off. Fan noise and airframe noise are dominant at approach. Several noise treatment techniques exist to reduce fan noise. Acoustic treatment within the intake, bypass and core ducts has been one of the most successful [2]. Acoustic liner optimisation therefore plays a very important role in the design of low noise engines. Liners can be optimised with respect to their physical parameters to minimise or maximise a cost function. The optimum liner design will depend on the choice of the cost function.

In an optimisation study carried out by Lafronza *et al.* [18], an approximate calculation of the perceived noise level (PNL) [81] was used as the cost function. A mode-matching solution was used for the acoustic analysis. The perceived noise level (PNL) metric mea-

sured in PNdB, gives a rating of the noisiness of sounds which have similar durations and which do not contain strong discrete frequency components [82]. The aim of the study in reference [18] was to investigate the potential increase in noise attenuation using an axially segmented liner as opposed to a uniform liner. The optimisation technique used was the response surface modelling method [83]. This involves selecting a number of points at which simulations are run using design of experiment techniques and then fitting the data with a response surface. An LPτ [77] DoE technique was used, and a kriging method was used to construct the response surface. In order update the kriging model and tune the hyper-parameters, a Genetic Algorithm (GA) search followed by a Dynamic Hill Climbing (DHC) search was used. When a satisfactory accuracy of the response surface was attained, the latter was searched using a hybrid search (GA search followed by a DHC search) to obtain the optimum. Results from the study by Lafronza *et al.* indicated that, axially segmented liners are beneficial over uniform liners only when a limiting number of propagating modes is present. In this thesis, the benefit of axially segmented liners, as well as different liner impedances on the inner and outer duct walls, will be assessed by using a computational scheme for the acoustic analysis.

In addition to axially segmented liners, a study carried out by Robinson and Watson [84] using a finite element model for a rectangular duct with uncertain impedances, showed that for a multimodal noise source, checkerboard liners had less than a 25 percent chance of outperforming uniform liners with moderate levels of uncertainty. The uncertainty in liner impedances arises from the manufacturing and installation procedures. However, in deterministic liner designs the checkerboard liner showed a significant improvement over a similarly designed uniform liner [84]. This study did not include the effect of mean flow. It is also important to note that since a gradient-based optimisation method was used to design the checkerboard liner, a global optimum was not necessarily found.

Highlighting the importance of the cost function in liner optimisation, Law and Dowling [85] showed that optimising with respect to, say, an acoustic power cost function does not necessarily translate into a reduction in perceived noise level at an observer on

the ground. They carried out optimisation studies with single and double layer liners using a perceived noise level cost function based on radiation patterns. The use of this cost function was found to be beneficial for double layer liners but not for single layer liners. In reference [15] Law and Dowling show that the negative effect of scattering on the effectiveness of multiple segment liners can be countered by the arranging the liner segments so that, the more effective liners are placed in the upstream liner segments and the less effective liners are placed in downstream liner segments. This will result in effective sound attenuation in the upstream liner segments such that the effects of scattering further downstream are negligible.

Copiello and Ferrante [86] use a multi-objective optimisation algorithm and an analytical prediction method to design zero-splice liners for aeroengine intakes. In their study, two cost functions are used: the effective perceived noise level (EPNL) at the approach and cutback conditions. The optimisation method used is a Non-Dominated Sorting Genetic Algorithm II (NSGA-II) [87]. The results from this study were validated using results from the well established empirical 'impedance matching' method. This automated liner design procedure provides a quick method of choosing liner properties at the preliminary design stage. In order represent realistic engine conditions during the liner design process, more advanced prediction methods such as numerical methods can be used.

2.5 Summary

In order to meet the ACARE requirements for aircraft noise by 2020, further reductions in the overall aircraft noise will be needed. This implies that, major contributors such as fan noise, jet noise and airframe noise will have to be considerably reduced over the next decade. Fan noise, which is a major noise source at approach and take-off, can be reduced either at source, or by acoustic treatment in the intake and bypass ducts. The prediction of noise attenuation by acoustic treatment can be achieved by using analytical or computational methods. The most commonly used computational method is the finite element method. For irrotational flows, the propagation of sound in intake and bypass

ducts can be formulated in terms of a convected wave equation in velocity potential.

Many optimisation techniques can be used to optimise the properties of acoustic treatment used in intake and bypass ducts to minimise the radiated sound power. Several methods have been proposed to incorporate analytical and computational prediction methods within optimisation methods.

Chapter 3

Introduction to SOFT: Application to model problems

3.1 Introduction

The aim of this chapter is to introduce the use of an automatic optimisation tool to be integrated with acoustic analysis. SOFT (Smart Optimisation For Turbo-machinery) [10] is an in-house Rolls-Royce optimisation system which provides a link between simulation code(s) and optimisation algorithms. SOFT currently provides four optimisation libraries, namely, local and global optimisers, Design of Experiments, ANOVA (ANalysis Of VAriation) and RSM (Response Surface Modelling). Although there are many optimisation algorithms provided within each of these libraries, there is not a single algorithm that is best suited to all engineering problems. In order to find an appropriate optimisation strategy for acoustic engineering problems, a number of algorithms have been applied to simple acoustic engineering model problems with known solutions.

In this chapter, the acoustic absorption by a layer of material placed at the end of a uniform straight duct is maximised by using optimisation algorithms within SOFT. The acoustic absorption coefficient is defined as the ratio of the absorbed to the incident acoustic power and therefore a good measure for assessing the performance of sound absorbing

materials. When the incident acoustic power is perfectly absorbed this value is maximum.

The first model problem is plane wave propagation in a uniform duct terminated with a sound absorbing layer. The acoustic property of the terminating surface is described by the (specific) acoustic impedance, which is the ratio of the acoustic pressure and the particle velocity. The normal incidence absorption coefficient of the termination is maximised by varying real and imaginary parts of the complex acoustic impedance (namely resistance and reactance, respectively), by using different optimisation algorithms. To verify the solution obtained by the optimisation algorithms in SOFT, a two-dimensional contour plot of the absorption coefficient against acoustic resistance and reactance, is used to illustrate the exact location of the optimum impedance.

The second problem is that the absorption coefficient of an acoustic absorbing termination of a uniform duct for a diffuse sound field incidence is optimised. The diffuse sound field consists of many acoustic duct modes with different mode angles. For this problem, a single cavity liner commonly used for aeroengine ducts is considered as the acoustic termination. A single cavity liner consists of a honeycomb layer with an impervious backing sheet and a porous facing sheet. The facing sheet resistance and the liner depth of the single cavity liner at the duct end are optimised to maximise the acoustic absorption. The optimisation exercises are performed firstly for a single frequency, and secondly for multiple frequencies.

The liner resistance and depth optimised by using SOFT algorithms are verified by comparison with contour plots obtained by calculating the cost function at grid points over the design space.

3.2 SOFT algorithms

The optimisation algorithms in SOFT used in this study fall into two main categories, local search algorithms which are suitable for single peak (unimodal) functions, and global search algorithms which are suitable for multimodal functions. The local search algorithms applied in this chapter are Dynamic Hill Climbing (DHC) and Sequential Quadratic Pro-

gramming (SQP). The global search algorithms include, Genetic Algorithm (GA), Adaptive Range Multi-Objective Genetic Algorithm (ARMOGA) and Simulated Annealing (SA). In addition to these search algorithms, a Response Surface Modelling (RSM) technique is also used. These algorithms are reviewed in the previous chapter and only features specifically related to the current study using SOFT are explained here.

3.2.1 Dynamic Hill Climbing

The DHC [72] algorithm in SOFT comprises of an inner loop and an outer loop. The inner loop consists of an efficient hill climbing technique for locating local optima and the outer loop focuses the inner loop to search random regions of the design space so that the design space is well explored. When the search within the inner loop converges, the search terminates and the outer loop re-initialises the inner loop with a randomly chosen starting point (see previous chapter for description of the inner loop algorithm).

In the DHC algorithm in SOFT the following parameters control the efficiency and accuracy of the method: initial step size, minimum step size and the number of random runs (for multimodal functions). The initial step size is the step of the first trial move, the minimum step size is the smallest step size by which a design variable can change and the number of random runs is the number of automatic restarts from a randomly selected initial value, after the algorithm has converged for a given initial step size and minimum step size.

3.2.2 Sequential Quadratic Programming

In SOFT, the SQP method is based on Schittkowski's non-linear programming methodology [88]. The efficiency and accuracy of this method implemented within SOFT is controlled by the 'desired accuracy' and the 'finite difference delta' parameters. When the change in the cost function is less than the 'desired accuracy' the optimisation process terminates. The 'finite difference delta' is the value by which the input variables are varied (perturbed). The cost function evaluations using the perturbed input variables are

then used to estimate the Hessian matrix. A line search is also performed in the design space in order to ensure an overall convergence of the method.

3.2.3 Genetic Algorithm

In the GA implemented within SOFT, which is based on the formulation by Holland (1973) [89], the performance of the method is controlled by two main parameters, the population size and the number of generations. The population size represents the number of randomly chosen designs and the number of generations is determined by the number of times these randomly chosen designs are transformed. The total number of evaluations in the GA is given by the product of the population size and the number of generations.

3.2.4 Adaptive Range Multi-Objective Genetic Algorithm

The ARMOGA method developed and implemented by Sasaki [90, 91] within SOFT, is a GA search which has the ability to change the search region based on the best designs obtained from previous generations. This ability to change the search region comes from the 'adaptive range' capability of the algorithm [90, 91]. It makes use of a set of optimal solutions called a Pareto set, which is a group of optimal solutions obtained from assigning different weights to a combination of cost functions. The 'adaptive range' capability is not used in this thesis, because the optimisation studies carried out here are all for single objectives, in which case an ARMOGA search reduces to a basic GA search based on the formulation in references [90, 91]. Throughout this thesis, this method is still referred to as, an ARMOGA search. The performance of the ARMOGA method in SOFT is controlled mainly by the population size and number of generations. The population size represents the number of randomly chosen designs and the number of generations is determined by the number of times the initial population is transformed.

3.2.5 Simulated Annealing

In SOFT, the SA algorithm is based on the Ingbar code [92]. In this method, the 'Initial Parameter Temperature' (IPT) and the 'Temperature Anneal Scale' (TAS) control the performance of the method. The IPT determines the range of acceptable designs. At a high IPT the range of configurations which may be accepted is large. The TAS determines the rate at which the initial temperature is reduced. At a high TAS, the initial temperature is reduced at a slower rate.

The termination of the algorithm is determined by three parameters: the 'accepted to generated ratio', 'maximum cost repeat' and the 'cost precision'. The 'accepted to generated ratio' is the least allowable ratio of the accepted configurations to generated configurations. As the optimisation process evolves, this ratio gets smaller. The 'maximum cost repeat' is the maximum number of times the cost function repeats itself within the limits defined by a value called the 'cost precision', before the algorithm terminates. This 'maximum cost repeat' parameter is used when the ratio of accepted configurations to generated configurations is less than the 'accepted to generated ratio', in order to avoid convergence in a local minimum.

3.2.6 Response Surface Modelling

The accuracy of RSM depends on how well the response surface approximates the values from the real code. In this light, in SOFT, having created a response surface from a number of DoE points, further updates may be required to obtain an accurate response surface. The update points are obtained by taking the optimum input variables from searching the latest response surface and then feeding this value back into the real code to get the output. The input and output values from the real code are then used to update the DoE points and a new response surface created. This process is repeated until convergence is achieved between the optimum cost function obtained from searching the response surface and the output from the real code, using the optimum input variables.

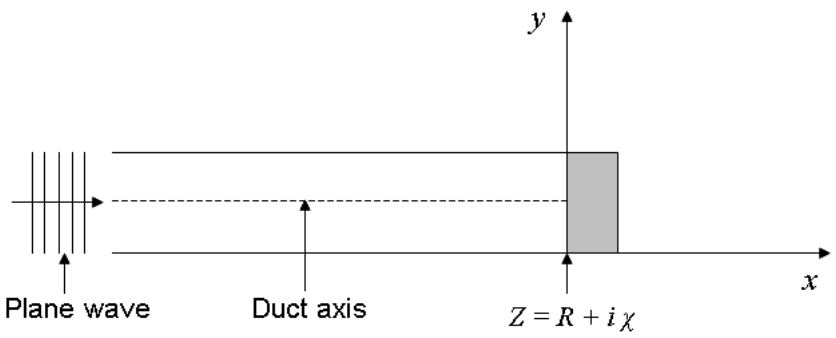

Figure 3.1: Sketch of uniform tube showing absorbing termination with complex acoustic impedance Z, where R is the resistive part and χ is the reactive part.

3.3 Model problem 1: Acoustic absorption for normal incidence

A sketch of the configuration for problem 1 is shown in Figure 3.1. A plane wave is propagating in a uniform tube with an absorbing layer. The absorbing surface is locally reacting, which means that the pressure at a point on the surface depends only on the acoustic variables at that point. The specific acoustic impedance is defined by the ratio of the pressure to the particle velocity at a point. The axis of the tube is denoted by x, and y is the transverse coordinate. Incident sound propagates in the tube from left to right, and is partially absorbed by the absorbing layer. The rest is reflected back at the surface and propagates from right to left.

3.3.1 Analytical solution

In this problem, it is assumed that the acoustic pressure, p in the tube satisfies the one-dimensional wave equation given by,

$$\frac{d^2p}{dx^2} - \frac{1}{c^2}\frac{d^2p}{dt^2} = 0. \tag{3.1}$$

For a time harmonic wave, $p(x,t) = p(x)e^{i\omega t}$, where $p(x)$ is a complex pressure amplitude, x denotes the axis of the impedance tube, t is time, ω is the angular frequency and c

is the speed of sound. Substituting this into Equation (3.1) gives the one-dimensional Helmholtz equation:

$$\frac{d^2p}{dx^2} + k^2p = 0, \tag{3.2}$$

where $k = \omega/c$ is the wave number. The general solution of Equation (3.2) is given by

$$p(x) = Ae^{-ikx} + Be^{ikx}, \tag{3.3}$$

where A and B are the complex amplitudes of the plane wave propagating in the positive and negative x directions respectively. From the linearised momentum equation,

$$\frac{du}{dt} + \frac{1}{\rho}\frac{dp}{dx} = 0, \tag{3.4}$$

where u is the particle velocity and ρ is the density. This implies that

$$u = -\frac{1}{i\omega\rho}\frac{dp}{dx}. \tag{3.5}$$

From Equations (3.3) and (3.5),

$$u = \frac{1}{\rho c}\left(Ae^{-ikx} - Be^{ikx}\right). \tag{3.6}$$

The specific acoustic impedance Z is the ratio of the acoustic pressure to the particle velocity. For convenience, taking the position of the absorbing surface to be at $x = 0$ gives,

$$Z = \frac{p}{u} = \rho c\left(\frac{A+B}{A-B}\right). \tag{3.7}$$

Therefore,

$$B = A\left(\frac{z-1}{z+1}\right) \tag{3.8}$$

where $z = Z/\rho c$ is the non-dimensional impedance.

3.3.2 The absorption coefficient

The absorption coefficient η of the acoustic absorbing termination is given by

$$\eta = \frac{I_+ - I_-}{I_+}, \tag{3.9}$$

where I_+ and I_- are the time-averaged intensities of the incident and reflected waves respectively. The time-averaged intensity is given by,

$$I = \overline{\langle pu \rangle} \tag{3.10}$$

where p and u are the acoustic pressure and particle velocity respectively and the 'bar' sign over p and u denotes averaging over one period. The complex notations for acoustic pressure and velocity, for a time-harmonic wave are written as:

$$p = \mathrm{Re}\left\{ [p_r + ip_i]\, e^{i\omega t} \right\} = p_r \cos\omega t - p_i \sin\omega t, \tag{3.11}$$

$$u = \mathrm{Re}\left\{ [u_r + iu_i]\, e^{i\omega t} \right\} = u_r \cos\omega t - u_i \sin\omega t, \tag{3.12}$$

and therefore,

$$pu = p_r u_r \cos^2\omega t + p_i u_i \sin^2\omega t - p_r u_i \cos\omega t \sin\omega t - p_i u_r \cos\omega t \sin\omega t.$$

The time-averaged intensity is thus given by,

$$I = \frac{1}{T}\int_0^T pu dt = \frac{1}{2}\left(p_r u_r + p_i u_i\right), \tag{3.13}$$

where $T = 2\pi/\omega$ is the period. This can be calculated as either,

$$I = \frac{1}{2} p u^*, \tag{3.14}$$

or

$$I = \frac{1}{2} p^* u. \tag{3.15}$$

From Equations (3.3) and (3.6), the time-averaged intensities I_+ and I_- for incident and reflected waves, respectively, can be calculated by,

$$I_+ = \frac{1}{2} A e^{-ikx} \left(\frac{1}{\rho c} A e^{-ikx} \right)^* = \frac{|A|^2}{2\rho c},$$

and

$$I_- = \frac{1}{2} B e^{-ikx} \left(\frac{1}{\rho c} B e^{-ikx} \right)^* = \frac{|B|^2}{2\rho c}.$$

From expression (3.9),

$$\eta = \frac{|A|^2 - |B|^2}{|A|^2} = 1 - \left|\frac{B}{A}\right|^2 . \tag{3.16}$$

By using expression (3.8), the absorption coefficient of the absorbing termination can also be expressed as,

$$\eta = 1 - \left|\frac{z-1}{z+1}\right|^2 . \tag{3.17}$$

Note that $\eta \leq 1$, and $\eta = 1$ only when $z = 1$. This corresponds to $Z = \rho c$ which is the impedance of a plane wave traveling without any reflection. Clearly, this is the optimum impedance to maximize η.

The expression for the absorption coefficient given in (3.17) was evaluated over the design space, for different combinations of non-dimensional resistance r $(=R/\rho c)$ and non-dimensional reactance χ' $(=\chi/\rho c)$. Figure 3.2 shows a contour plot of the calculated values, in which the maximum of the absorption coefficient is seen to occur at (r, χ')=(1, 0) corresponding to a dimensional impedance $Z = \rho c$.

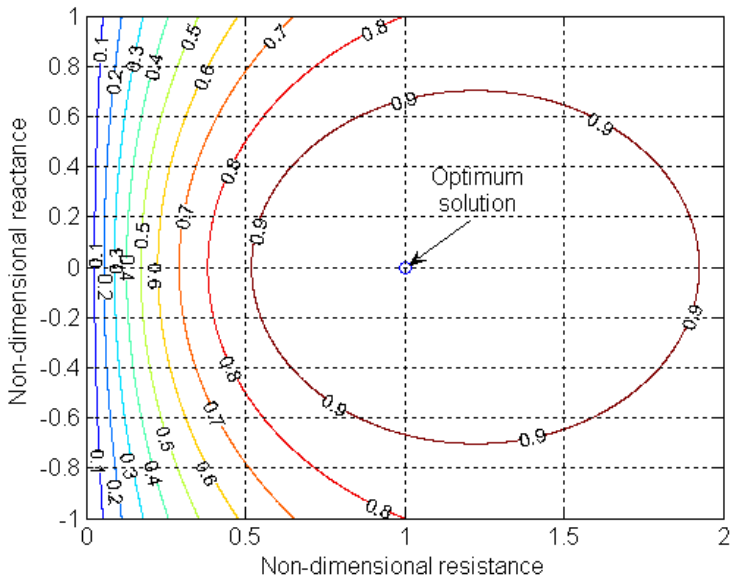

Figure 3.2: Contours of absorption coefficient η, plotted against non-dimensional resistance and non-dimensional reactance. ○: optimum $(1 + 0i)$.

3.3.3 SOFT optimisation

The optimisations are performed using the SOFT optimisation program, on a computer with a 2.00 GHz processor and 1.0 GB of RAM. The CPU time for each evaluation in the optimisation is approximately four seconds, which is a very low evaluation cost in comparison to computations for real applications.

Note that within SOFT, the bounds of the design variables are normalised such that they either vary from 0 to 1, or -1 to 1. This is important to improve the uniformity of the search over the design space. In this thesis, even for cases in which the range of design variables shown in the results figures is neither from 0 to 1 nor from -1 to 1, it is normalised in the optimisation process. This implies that a given step size within SOFT will be different for each of the design variables.

Figure 3.2 shows that the cost function, the normal absorption coefficient η has a single optimum (unimodal). In this light, either local or global optimisers from could be used to achieve this optimum. In addition, this is a trivial exercise since the solution is known. In SOFT, two local and three global search algorithms are tested on this problem. The local methods are SQP and DHC, and the global methods are, GA, ARMOGA and SA.

In all optimisations, some criterion needs to be put in place to terminate the process. For local searches, such as DHC and SQP, the process terminates when the current design cannot be further improved in the local region, within the limits set by the user (see sections 3.2.1 and 3.2.2). However, in a global search, no such criterion can be made since the there is always a chance that some region in the design space exists, which when searched may contain a better design. In a local search the process can be said to have converged meanwhile in a global search a different criterion is required to terminate the process. In a situation where the cost of an evaluation is high, it may be necessary to terminate even a local search before it is fully converged. In this light, the main concern when assessing the efficiencies of different local and global searches, is the improvement of the search with each new evaluation. In what follows, results are presented for op-

timisation algorithms: DHC, SQP, GA, ARMOGA and SA. The cost function, normal incidence absorption coefficient to two decimal places is calculated by using expression (3.17).

3.3.3.1 DHC search

Figure 3.3 shows the traces of a two-dimensional DHC search starting from a non-dimensional impedance of $0.5 + 0.2i$ and finding the maximum absorption coefficient ($\eta = 1.00$) at an impedance of $1 - 0.05i$. The initial and minimum step sizes are chosen to be 0.25 for the resistance and 0.5 for the reactance, considering the normalised ranges $[0, 1]$ and $[-1, 1]$ for resistance and reactance, respectively. Figure 3.4 shows the search history, with the 'best solution so far' versus the evaluation number. It shows the rate of improvement of the cost function with each new evaluation, and in this case the optimum is found after 6 evaluations.

3.3.3.2 SQP search

Figure 3.5 shows the traces of a two-dimensional SQP search, starting from an impedance of $0.5 + 0.2i$ and finding the maximum absorption coefficient ($\eta = 1.00$) at $0.96 - 0.0014i$. The point clusters show variations in the design variables by an amount defined by the 'finite difference delta', so that the quadratic approximation at each evaluation can be updated. The SQP search pattern also shows a number of line searches which ensure a global convergence of the method. In this problem, the 'desired accuracy' of the cost function is set to 0.001 and the 'finite difference delta' is set to 0.01 for the resistance and 0.02 for the reactance. Figure 3.6 shows the rate of improvement of the cost function with each new evaluation. The maximum value for the cost function is found after 22 evaluations.

3.3.3.3 GA search

Figure 3.7 shows results for a two-dimensional GA search. The population size is 50 and the number of generations is 2. The open circles represent the randomly generated initial population, and the filled circles represent the second generation. In this GA search, the distribution of designs in the second generation is limited to a region close to the global optimum, such that in the second generation the GA search resembles a local method. However, a maximum absorption coefficient ($\eta = 0.99$) at an impedance of $1.26 + 0.069i$ is found in the initial population, and the accuracy is not further improved in the second generation. Similarly, Figure 3.8 shows a limited distribution of designs in the second generation as the computed values for the cost function are similar, though not improved from the global optimum in the initial population.

3.3.3.4 ARMOGA search

In the ARMOGA search in Figure 3.9, the population size is 50 and the number of generations is 2. The open circles represent the initial population with 50 designs and the filled circles represent the second generation with another 50 designs. In this search, the maximum absorption coefficient ($\eta = 1.00$) at an impedance of $0.93 + 0.054i$ is found in the randomly generated designs in the initial population. In the second generation, even though the optimum from the initial population is not improved further, the designs are well spread out around the optimum value. This indicates that, this search can be very efficient in finding the global optimum for practical applications, where functions with multiple peaks are common. Figure 3.10 again shows the spread of the designs in the second generation as the cost function has a wide variation range.

3.3.3.5 SA search

Figure 3.11 shows designs generated from random perturbations applied to the initial design and subsequent accepted designs in the SA process. The SA search finds the maximum absorption coefficient ($\eta = 1.00$) at an impedance of $0.88 + 0.037i$ from a

random starting impedance value of $0.64 + 0.35i$. Figure 3.12 shows that this optimum is found after 64 evaluations. In this SA search the ITP is set to 1 and the TAS is set to 100.

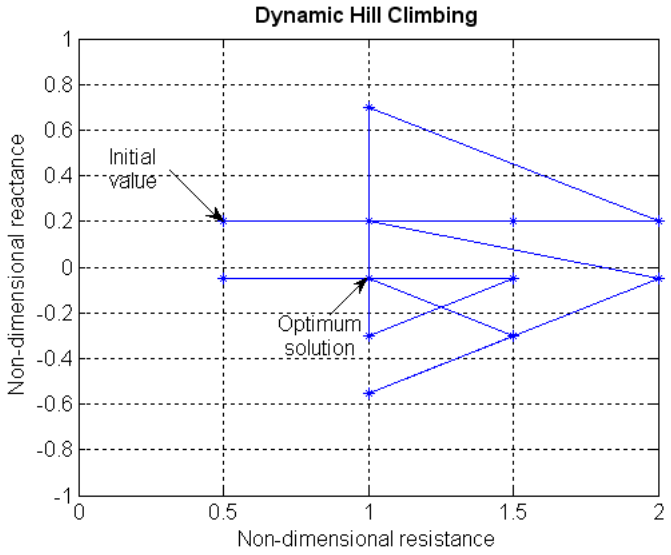

Figure 3.3: DHC search in two dimensions showing initial value of $0.5 + 0.2i$ and optimum impedance of $1 - 0.05i$.

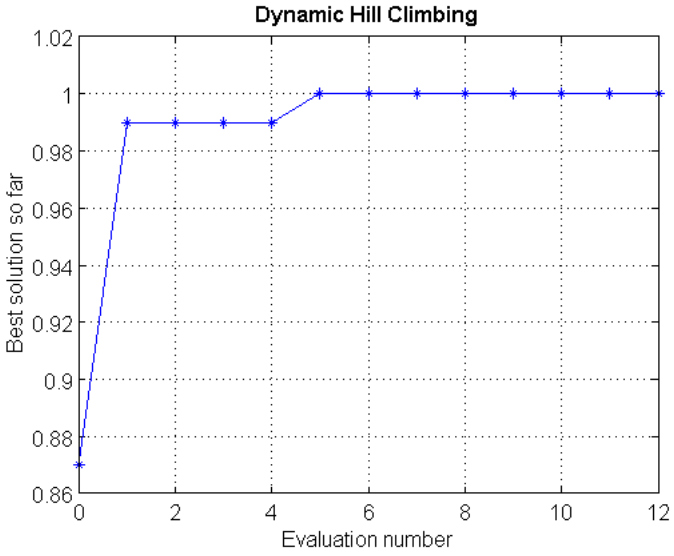

Figure 3.4: Search history for the DHC method, showing the rate of improvement of the cost function (absorption coefficient for plane wave incidence).

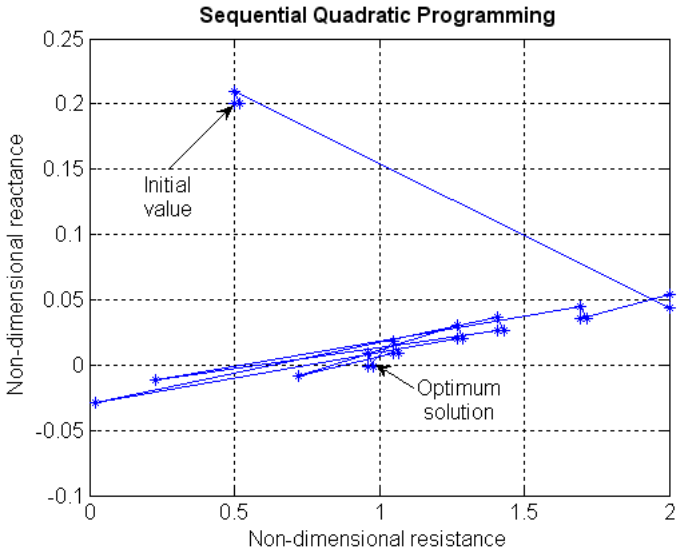

Figure 3.5: SQP search in two dimensions showing initial value of $0.5 + 0.2i$ and optimum impedance of $0.96 - 0.0014i$.

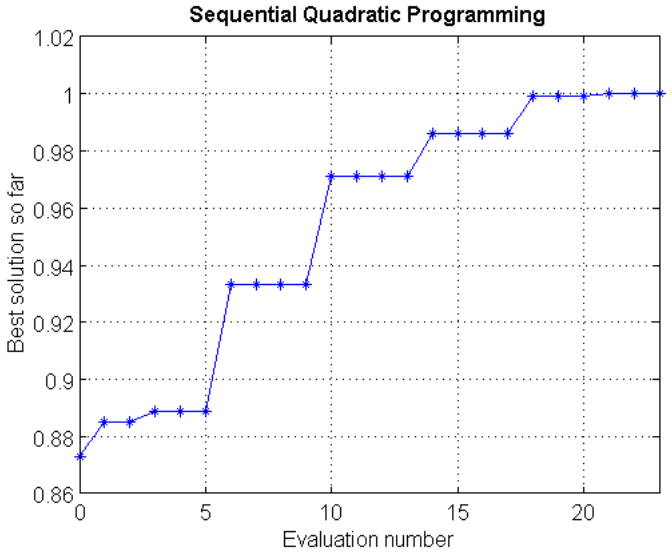

Figure 3.6: Search history for the SQP method, showing the rate of improvement of the cost function (absorption coefficient for plane wave incidence).

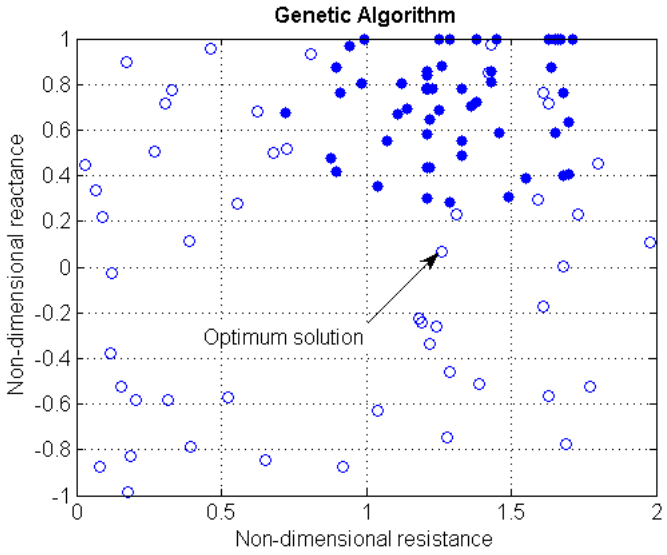

Figure 3.7: GA search in two dimensions showing optimum impedance of $1.26 + 0.069i$. Open circles represent designs in initial population and filled circles represent designs in second generation.

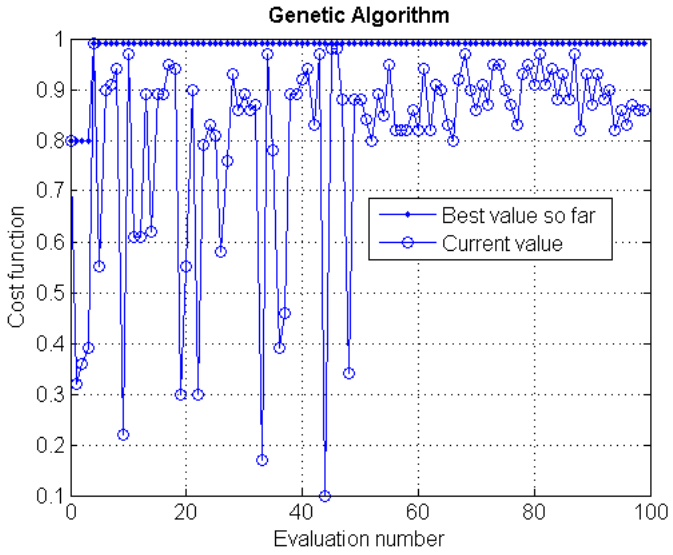

Figure 3.8: Search history for the GA method, showing the rate of improvement of the cost function (absorption coefficient for plane wave incidence).

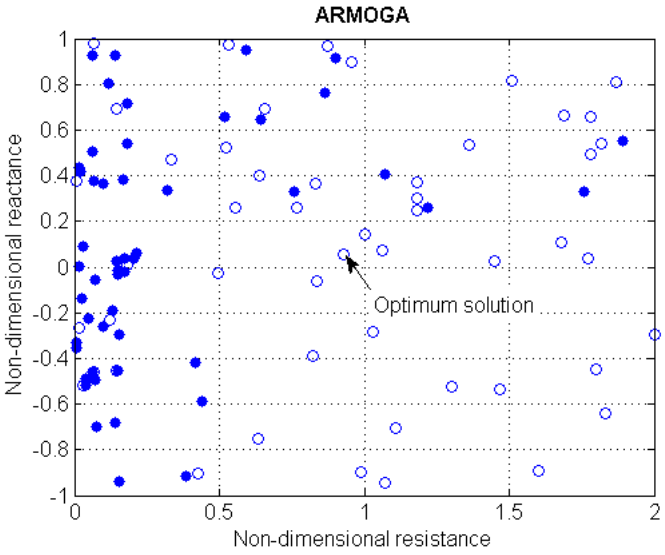

Figure 3.9: ARMOGA search in two dimensions showing optimum impedance of $0.93 + 0.054i$. Open circles represent designs in the initial population and filled circles represent designs in the second generation.

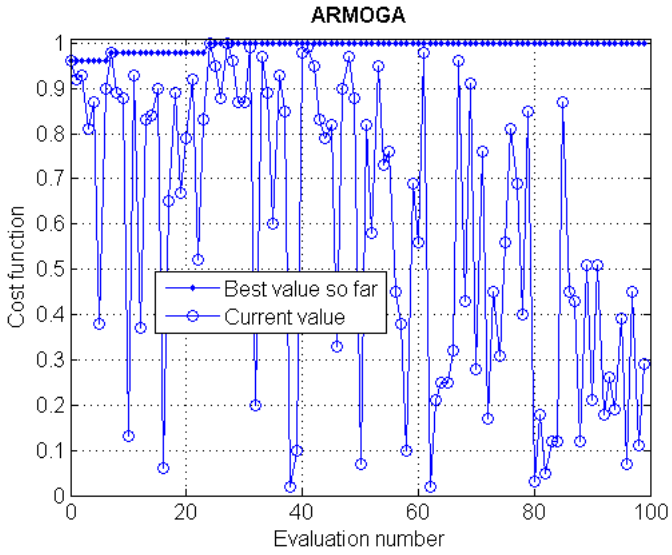

Figure 3.10: Search history for the ARMOGA method, showing the rate of improvement of the cost function (absorption coefficient for plane wave incidence).

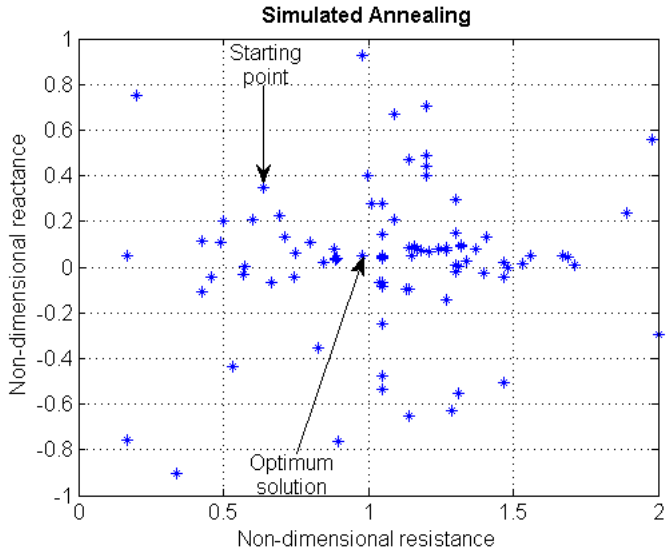

Figure 3.11: SA search in two dimensions showing starting point of $0.64 + 0.35i$ and optimum impedance of $0.88 + 0.037i$.

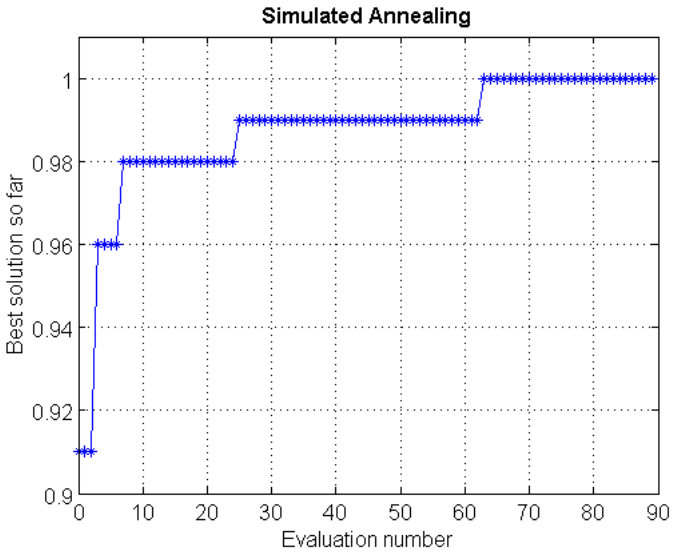

Figure 3.12: Search history for the SA method, showing the rate of improvement of the cost function (absorption coefficient for plane wave incidence).

3.3.4 Discussion

In the simple model problem considered in this section, five optimisation algorithms in SOFT have been used; DHC, SQP, GA, ARMOGA and SA. The maximum absorption coefficient and the corresponding impedance achieved by all five methods are in close agreement with the true solution. However, it has been shown that due to the unimodal nature of the function, the local search methods (DHC and SQP) are more efficient than the stochastic methods (GA, ARMOGA and SA). This is because in the local methods, the progress of the search depends on the nature of the function being searched, such that functions which have a single peak (unimodal) are easy to exploit. This is not the case with the global methods which all have a stochastic component and do not take into account the nature of the function being searched.

Using the DHC and SQP methods, the optimum was found in 6 and 22 evaluations respectively (Figures 3.4 and 3.6). In the GA and ARMOGA searches, an initial population size of 50 designs is used. This initial population is transformed once to obtain the second generation which further explores the design space (see Figures 3.7 and 3.9 respectively). Both the GA and ARMOGA searches find the global optimum for this very simple problem as expected, despite a less accurate optimum from the GA search. In addition, it has been shown that the good spread of the designs in the ARMOGA search in the second generation is promising to provide a useful tool when dealing with multimodal functions. In the SA algorithm a global optimum is found after 64 evaluations as shown in Figure 3.12.

It is important to note that there is a slight variation in the optimum impedances obtained from each of the search methods. This is due to the fact that the function being searched has a very gentle slope at the optimum absorption coefficient, such that slightly different impedances give virtually the same maximum absorption coefficient.

Therefore, the global methods all explore the design space to obtain a reasonably sufficient value, as the maximum absorption coefficient, $\eta = 1.0$. However, with functions that have sharper peaks, to obtain a more accurate solution, a global search would

need to be improved by applying a local search (DHC or SQP) once the general location of the global optimum is found. The choice of the local search method will depend on prior knowledge of the design space. For example, SQP is more suitable for representing quadratic functions as opposed to DHC which has a more simplistic yet robust algorithm that is less dependent on the nature of the design space. In most engineering problems the nature of the design space is not known, in which case DHC would be more suitable than SQP.

3.4 Model problem 2: Acoustic absorption for diffuse field incidence

A sketch of the model problem is shown in Figure 3.13. The axis of the duct is denoted by x, y is the transverse coordinate, and H is the height of the duct. In this problem, it is assumed that the sound field within the duct is diffuse. Such a sound field can be modelled as a superposition of sound fields produced by many duct modes with different propagation angles. In the current study all the modes which are cut-on for a given duct height and frequency are considered as the sound source. All these modes contain equal power. The duct is terminated with a locally reacting, single cavity liner.

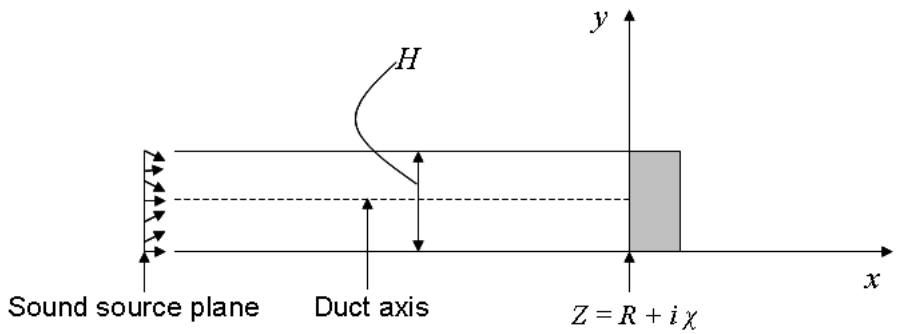

Figure 3.13: Sketch of uniform duct subject to a multi-mode noise source, showing absorbing termination with complex acoustic impedance Z, where R is the resistive part and χ is the reactive part.

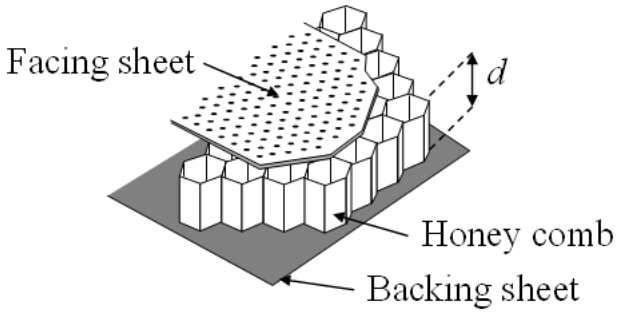

Figure 3.14: Sketch showing single cavity liner with depth, d.

3.4.1 The single cavity liner

Single cavity liners [82] are commonly used as an acoustic treatment within turbofan engine intake and bypass ducts. As shown in Figure 3.14 it consists of a honey comb shell with an impervious backing sheet and a porous facing sheet. The liner impedance model used in this study is the simple Single Degree Of Freedom (SDOF) model given by $Z = R + i\chi$, where R is the acoustic resistance which is constant and independent of frequency, and χ is the acoustic reactance which is expressed as:

$$\chi = \rho c(kl - \cot(kd)), \tag{3.18}$$

where k is the wave number, d is the liner depth, and l is the mass inertance. The acoustic reactance is therefore dependent on frequency. With an idealised single cavity liner with a small mass reactance, maximum sound absorption occurs when the liner depth d, is close to odd multiples of one-quarter of the wavelength, of the sound wave, because when such a condition is satisfied, the velocity through the facing sheet is maximum and the dissipation of energy through the facing sheet becomes greatest.

3.4.2 Analytical solution for a single higher order mode

For a rectangular duct of height $H = 1$ shown in Figure 3.13, the complex pressure amplitude p must satisfy the two-dimensional Helmholtz equation:

$$\frac{\partial^2 p}{\partial x^2} + \frac{\partial^2 p}{\partial y^2} + k^2 p = 0. \tag{3.19}$$

For the acoustic wave propagation in the positive x direction, the pressure can be expressed in the form: $p(x, y) = g(y)e^{-ik_x x}$, where $g(y)$ describes the pressure variation in the y direction and k_x is the axial wave number. Substituting this into Equation (3.19) leads to,

$$\frac{\partial^2 g}{\partial y^2} + k'^2 g = 0, \tag{3.20}$$

where $k'^2 = k^2 - k_x^2$. The general solution of Equation (3.20) is given by,

$$g(y) = C \cos k'y + D \sin k'y. \tag{3.21}$$

Using boundary conditions at the duct walls,

$$\frac{\partial p}{\partial y} = 0 \quad \text{at} \quad y = 0 \quad \text{and} \quad y = H, \tag{3.22}$$

gives,

$$g(y) = C_n \cos\left(\frac{n\pi}{H}\right) y \quad \text{for} \quad n = 0, 1, 2... \tag{3.23}$$

The expression for complex pressure can therefore be written as,

$$p_n(x, y) = C_n e^{-ik_x^n x} \cos\left(\frac{n\pi}{H}\right) y, \tag{3.24}$$

where,

$$k_x^n = \pm\sqrt{k^2 - \left(\frac{n\pi}{H}\right)^2}. \tag{3.25}$$

This implies,

$$p_n(x, y) = C_n e^{-ik_x^n x} \cos\left(\frac{n\pi}{H}\right) y + D_n e^{ik_x^n x} \cos\left(\frac{n\pi}{H}\right). \tag{3.26}$$

For convenience, taking the position of the absorbing surface to be at $x = 0$ gives,

$$p_n = C_n \cos k_n y + D_n \cos k_n y. \tag{3.27}$$

From the linearised momentum equation,

$$u_n = \frac{1}{\rho\omega}\left(k_x^n C_n \cos k_n y - k_x^n D_n \cos k_n y\right). \tag{3.28}$$

Therefore, the specific acoustic impedance,

$$Z = \frac{p_n}{u_n} = \frac{\rho\omega(C_n + D_n)}{k_x^n(C_n - D_n)} \quad \text{where} \quad k_x^n = k\sqrt{1 - \left(\frac{cn\pi}{\omega H}\right)^2} = k\lambda_n. \tag{3.29}$$

Expressing C_n in terms of D_n gives

$$C_n = \frac{D_n(\rho c + Z\lambda_n)}{(Z\lambda_n - \rho c)}. \tag{3.30}$$

3.4.3 The absorption coefficient for a single higher order mode

By using an argument similar to that leading to expression (3.16), the absorption coefficient can be written as:

$$\eta_n = 1 - \left|\frac{D_n}{C_n}\right|^2 = 1 - \left|\frac{Z\lambda_n - \rho c}{\rho c + Z\lambda_n}\right|^2, \tag{3.31}$$

where, $\lambda_n = \sqrt{1 - \left(\frac{n\pi}{kH}\right)}$.

3.4.3.1 Single frequency

For a single frequency when the source consists of N propagating modes each having unit power, the total incident power P_I=N and the total absorbed power P_A by the acoustic termination can be written in terms of the absorption coefficient for each mode so that, $P_A = \eta_1 + \eta_2 + \eta_3 + ... + \eta_N$, with the absorption coefficients for each mode. This implies that, the total absorption coefficient η_{tot} for all N modes is given by,

$$\eta_{tot} = \frac{P_A}{P_I} = \frac{(\eta_1 + \eta_2 + ... + \eta_N)}{N}. \tag{3.32}$$

The total absorption coefficient η_{tot} is used as the cost function to be maximised in the optimisation exercises. Figure 3.15 shows contours of the absorption coefficient against non-dimensional resistance r and cell depth d at 5 kHz. The maximum absorption coefficient is 0.96, and occurs at a non-dimensional resistance r, of 1.3 and a liner depth d of 5

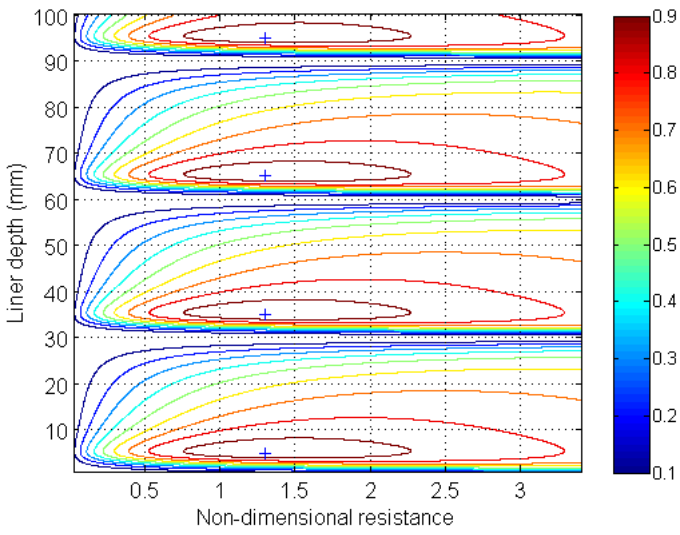

Figure 3.15: Contours of absorption coefficient with a noise source at 5 kHz, + : Optima; $r = 1.3$ and $d = 5.5$ mm, 35.5 mm, 65.5 mm and 95.5 mm.

mm. A hill-like pattern of contours is repeated in the direction of the 'd' axis with a cycle of 30 mm. This periodicity occurs as a result of the cotangent term in the expression for the reactance of a single cavity liner, given by expression (3.18) which has a periodicity of π/k for d. This implies that, when performing a single frequency optimisation, to prevent the search from exploring repeats of the same function, the liner depth d can be restricted to vary only in the range, $0 < d \leq \pi/k$.

'Diffuse field' model

To confirm the expression for the absorption coefficient derived for a single frequency source, a 'diffuse field' model is also used to obtain an expression for the absorption coefficient (details are included in Appendix A). Two-dimensional contours of absorption coefficient versus facing sheet resistance and liner depth are then generated using the expression obtained from the 'diffuse field' model. A comparison is then made between the contours obtained by using the expression of total absorption coefficient derived from considering 'all propagating modes' (expression (3.32)) and contours obtained by using an expression derived from a 'diffuse field' model. In a 'diffuse field' model, it is assumed that

all points in the sound field may be considered to be made up of mutually uncorrelated plane waves that propagate in all directions with equal probability. The absorption coefficient of the absorbing termination in the diffuse field is then calculated from the total power absorbed per unit area of a surface, integrated over all angles of incidence. This comparison between both methods is possible because for the single frequency source, higher order modes can be considered as plane waves propagating in different directions, hence approximating a diffuse field.

3.4.3.2 Multiple frequencies

For a range of frequencies, the mean absorption coefficient is used as the cost function in the optimisation. At each frequency within the range, the absorption coefficient is calculated by using expression (3.32). The mean absorption coefficient for a frequency range $[f_1,\ f_2]$, is given by:

$$\overline{\eta}(R,\chi) = \frac{1}{(f_2 - f_1)} \int_{f_1}^{f_2} \eta(f,R,\chi) df, \tag{3.33}$$

where the integral is evaluated using the trapezium rule. Figure 3.16 shows contours of absorption coefficient with a multiple frequency noise source (20 Hz to 1920 Hz in steps of 100 Hz). Multiple peaks exist due to the fact that the source contains multiple frequencies. The maximum absorption coefficient of 0.75 occurs at a non-dimensional resistance r, of 1.7 and a liner depth d, of 57 mm. A local optimum exists at a non-dimensional resistance of 1.7 and a liner depth of 140 mm.

3.4.4 SOFT optimisation (single frequency multiple modes)

The optimisations within SOFT in this section have been carried out using the same computer as described earlier in section 3.3.3, this time for a multiple mode source at 5 kHz. The cost function for the optimisation is the total absorption coefficient for all modes given by expression (3.32), with the non-dimensional resistance r, and the liner depth d as design variables. The cost function is evaluated at a frequency of 5 kHz and the

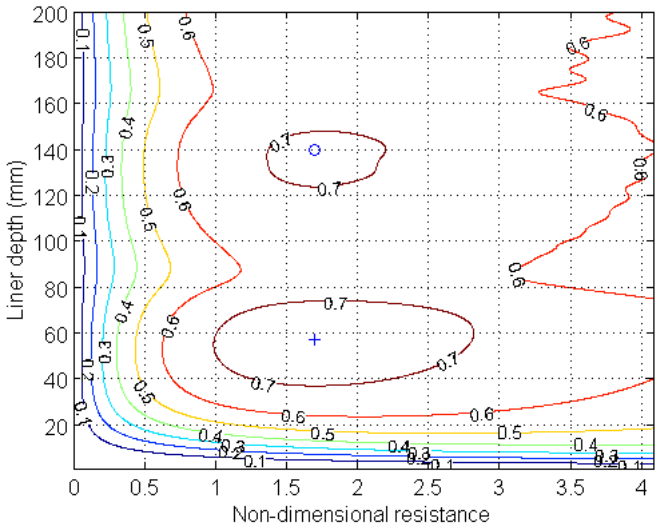

Figure 3.16: Contours of absorption coefficient for a multiple frequency source (20 Hz to 1920 Hz in steps of 100 Hz), global optimum (+ : $r = 1.7$ and $d = 57$ mm) and local optimum (∘ : $r = 1.7$ and $d = 140$ mm).

duct height H is set to 1 m which gives a Helmholtz number kH of 104.7. Each evaluation takes approximately four seconds. The non-dimensional resistance is constrained to vary between 0 and 3 and the liner depth is constrained to vary between 0 and 30 mm due to the periodicity of the function with cell depth. However, within the optimisation process in SOFT, both variables are normalised so that they vary between 0 and 1.

In this problem three search methods are used, a DHC search, an SQP search and an ARMOGA search. The results from these search algorithms are compared to the result obtained from a contour plot of the absorption coefficient shown in Figure 3.15 which gives a maximum optimum absorption coefficient of 0.96 occurring at, $r = 1.3$ and $d = 5$ mm.

3.4.4.1 DHC search

Figure 3.17 shows a DHC search starting from, $r = 2.5$ and $d = 27$ mm. The optimum is found at $r = 1.4$ and $d = 6$ mm. In this DHC search, the initial step size is 0.75 for r and 7.5 mm for d. The minimum step size is 0.004 for r and 0.04 mm for d. Figure 3.18 shows

the convergence of the DHC search to the maximum absorption coefficient of 0.96 after 34 evaluations. This value is the same as the result obtained from contours of absorption coefficient in Figure 3.15, even though slight variations in the optimum r and d exist due to the existence of a fairly level region around the maximum absorption coefficient.

3.4.4.2 SQP search

Figure 3.19 shows the traces of the SQP search, highlighting the initial (r: 2.5 and d: 27 mm) and optimum (r: 1.2 and d: 6 mm) absorbing termination configurations. In this search, the 'finite difference delta' for the perturbation of the design variables is 0.03 for r and 0.3 for d, and the 'desired accuracy' for the absorption coefficient is 0.001. The maximum absorption coefficient of 0.96 is found after 40 evaluations as shown in Figure 3.20. This SQP result of 0.96 is the same as the result from the contours of absorption coefficient in Figure 3.15. Slight variations in the optimum r and d exist for the same reasons mentioned earlier.

3.4.4.3 ARMOGA search

In the ARMOGA search (see Figure 3.21), an initial population of 50 designs transformed once to give a total of 100 designs, is used to explore the design space. In this search the global optimum is found at $r = 1.6$ and $d = 5$ mm in the second generation. This corresponds to a maximum absorption coefficient of 0.95 which is found after 55 evaluations (see Figure 3.22). Due to the exploratory nature of the ARMOGA method, the optimum is not as accurate as the optima obtained from the local DHC and SQP methods, considering that the ARMOGA search finds a maximum absorption coefficient of 0.95 and not 0.96.

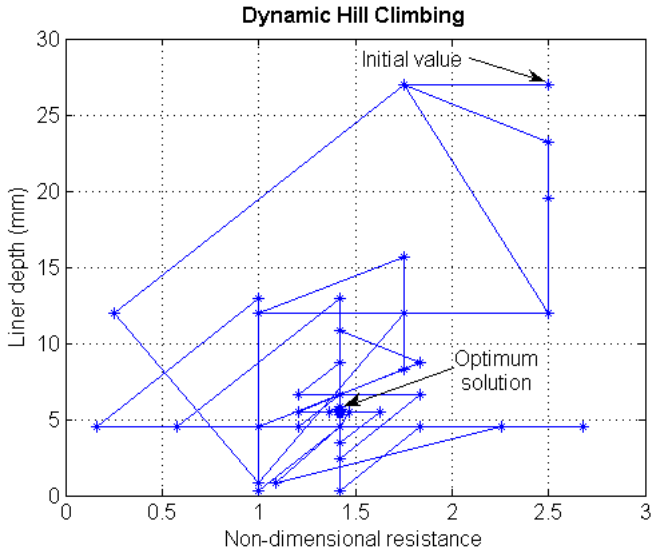

Figure 3.17: DHC search in two dimensions showing initial ($r = 2.5$ and $d = 27$ mm), and optimum ($r = 1.4$ and $d = 6$ mm) characteristics for the absorbing termination.

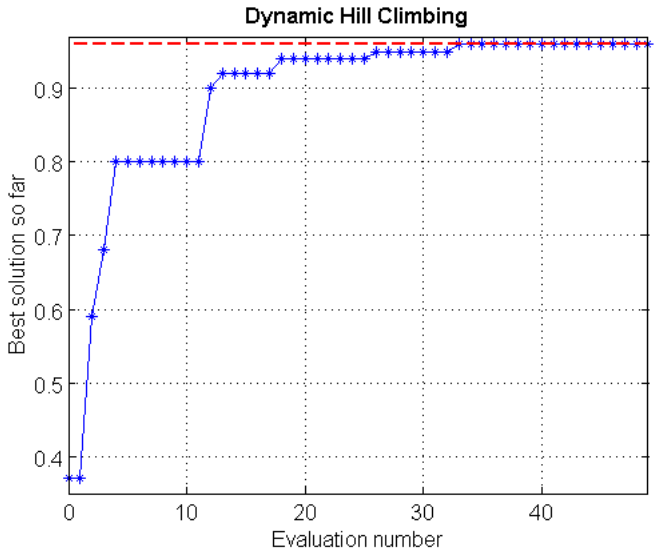

Figure 3.18: Search history for the DHC method, showing the rate of improvement of the cost function (absorption coefficient for single frequency multiple mode incidence) Dashed (red) line shows maximum at 0.96.

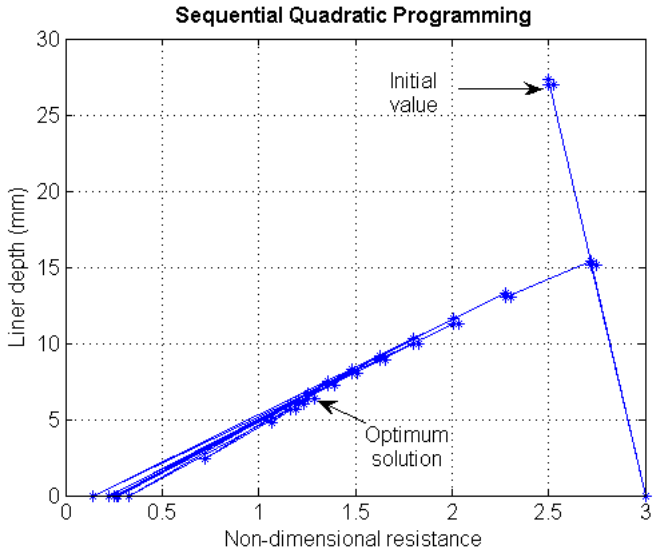

Figure 3.19: SQP search in two dimensions showing initial ($r = 2.5$ and $d = 27$ mm), and optimum ($r = 1.2$ and $d = 6$ mm) characteristics for the absorbing termination.

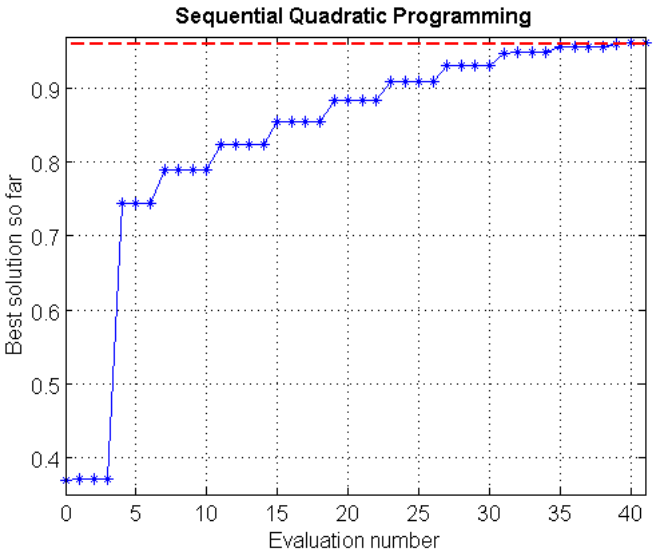

Figure 3.20: Search history for the SQP method, showing the rate of improvement of the cost function (absorption coefficient for single frequency multiple mode incidence). Dashed (red) line shows maximum at 0.96.

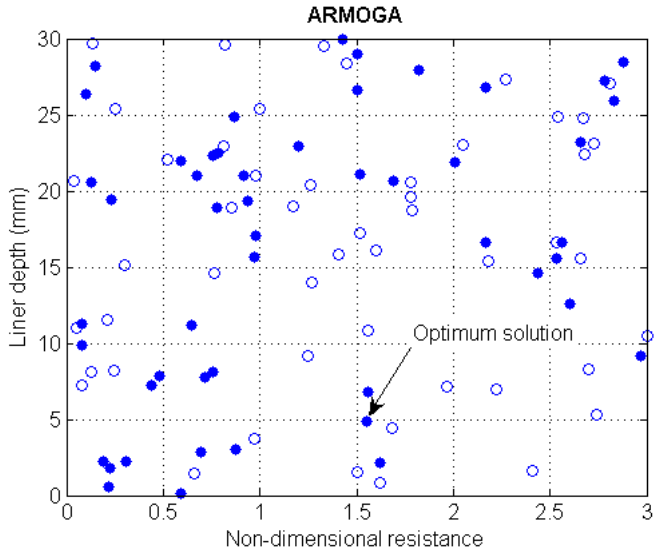

Figure 3.21: ARMOGA search in two dimensions showing optimum solution ($r = 1.6$ and $d = 5$ mm). Open circles represent designs in the initial population and filled circles represent designs in the second generation.

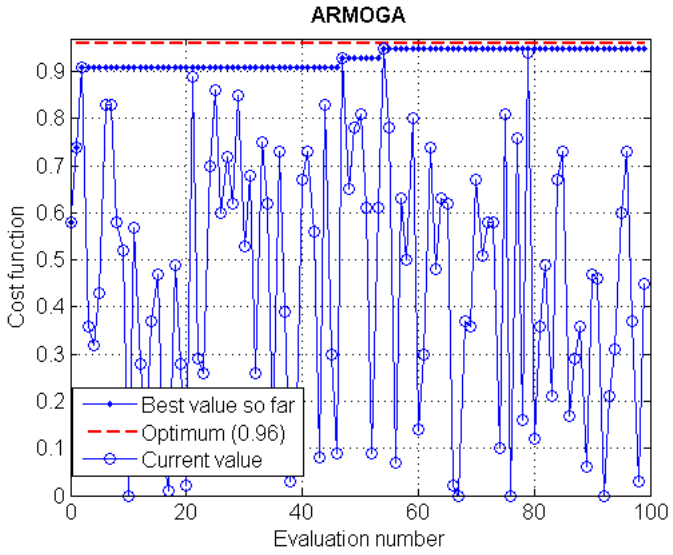

Figure 3.22: Search history for the ARMOGA method, showing the rate of improvement of the cost function (absorption coefficient for single frequency multiple mode incidence). Dashed (red) line shows maximum at 0.96.

3.4.5 SOFT optimisation (multiple frequencies multiple modes)

In this section, an optimisation study using a multiple frequency, multiple mode source is performed using SOFT and the same computer as described earlier in section 3.3.3. The cost function is the mean absorption coefficient for multiple frequencies from 20 Hz to 1920 Hz in steps of 100 Hz calculated by using expression (3.33). The input variables are the non-dimensional resistance and the liner depth, and each evaluation in the optimisation process takes approximately four seconds. The resistance r is constrained to vary between 0 and 4 and the liner depth d is constrained to vary between 0 and 200 mm. Within the SOFT optimisation process both variables are normalised so that they vary between 0 and 1.

In the SOFT optimisation process the following algorithms are used: DHC, SQP and ARMOGA. An ARMOGA search followed by a DHC search (hybrid search) is also used in this problem. In addition to these search methods, RSM is also applied to this problem. In the RSM method, evaluation points from the initial random population of the ARMOGA search are used as the DoE points to generate a response surface using a linear radial basis function. The response surface was then explored using an ARMOGA search. In general, to generate an accurate response surface, several updates of the DoE points are required. This is not the case in this simple model problem where a large number of evaluations are possible such that an accurate response surface can be obtained in the first trial. The number of DoE points required to generate an accurate response surface will clearly depend on the complexity of the function to be approximated. However, in this problem which has a function with a smooth multimodal variation shown in Figure 3.16, 50 DoE points are enough to accurately represent the function, even though constructing an accurate response surface can be a non-trivial exercise.

3.4.5.1 DHC

Figure 3.23 shows a two-dimensional DHC search starting from an initial value, $r = 3.5$ and $d = 120$ mm. In this search, for the initial step size, $r = 1.0$ and $d = 50$ mm, and for the minimum step size, $r = 0.5$ and $d = 25$ mm. Since the function is multimodal, the aim of this local search is to find which of the peaks the method locates rather than performing a finely tuned search, hence the large minimum step size. The DHC search finds the global peak at $r = 1.5$ and $d = 45$ mm after 18 evaluations (see Figure 3.24).

3.4.5.2 SQP

In the SQP search however, starting from the same initial value as the DHC search, the method finds a local peak at $r = 1.8$ and $d = 139$ mm (see Figure 3.25) after 20 evaluations as shown in Figure 3.26. In this search, the 'finite difference delta' is set to 0.04 for r and 2 mm for d. The 'desired accuracy' is set to 0.001. When dealing with multimodal functions, a global search followed by a local search is more appropriate.

3.4.5.3 ARMOGA

In Figure 3.27, an ARMOGA search (initial population of 50 designs transformed once) is used to explore the design space. A global optimum at $r = 1.7$ and $d = 61$ mm ($\bar{\eta} \approx 0.74$) is found in the initial population (see Figure 3.28).

3.4.5.4 Hybrid search (ARMOGA + DHC)

Figure 3.29 shows DHC traces in the refinement of the ARMOGA search. In the DHC search, the minimum step size is 0.125 for r and 6.25 mm for d. Figure 3.30 shows the improvement in the accuracy of the global optimum by the DHC search to obtain an absorption coefficient $\bar{\eta} \approx 0.75$, corresponding to the global optimum in the contour plot in Figure 3.16.

3.4.5.5 RSM using ARMOGA DoE

Figure 3.31 shows DoE points obtained from the initial population of the ARMOGA search. Using a linear RBF, the DoE points are used to construct a response surface. Figures 3.32(a) and 3.32(b) show the real function and the corresponding response surface which is explored using an ARMOGA search. The ARMOGA search of the response surface finds a global optimum at $r = 1.7$ and $d = 61$ mm where $\bar{\eta} \approx 0.74$. The agreement of this result with the result from exploring the real function, confirms the accuracy of the response surface used in this problem.

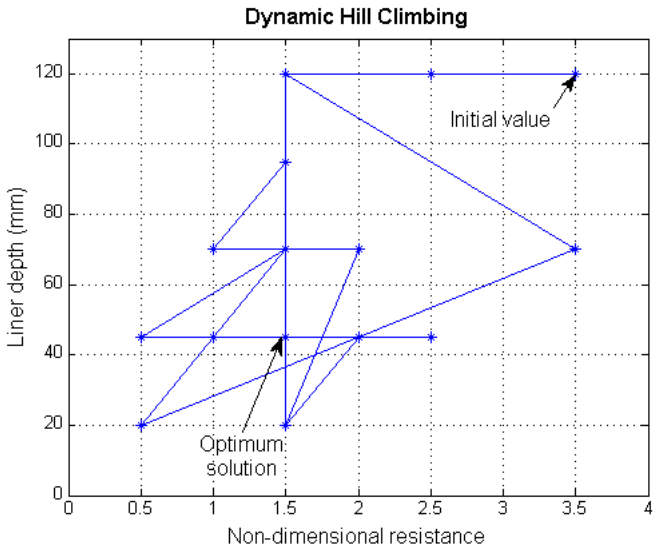

Figure 3.23: DHC search in two dimensions showing initial ($r = 3.5$ and $d = 120$ mm), and optimum ($r = 1.5$ and $d = 45$ mm) characteristics for the absorbing termination.

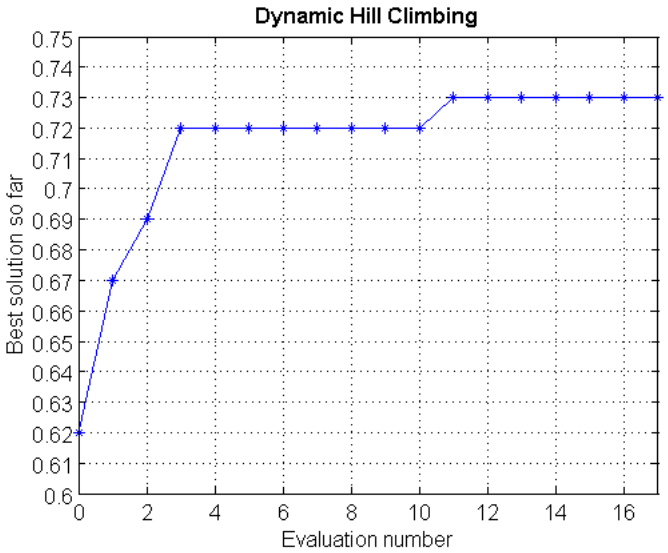

Figure 3.24: Convergence of DHC search towards global optimum absorption coefficient $\bar{\eta} = 0.75$.

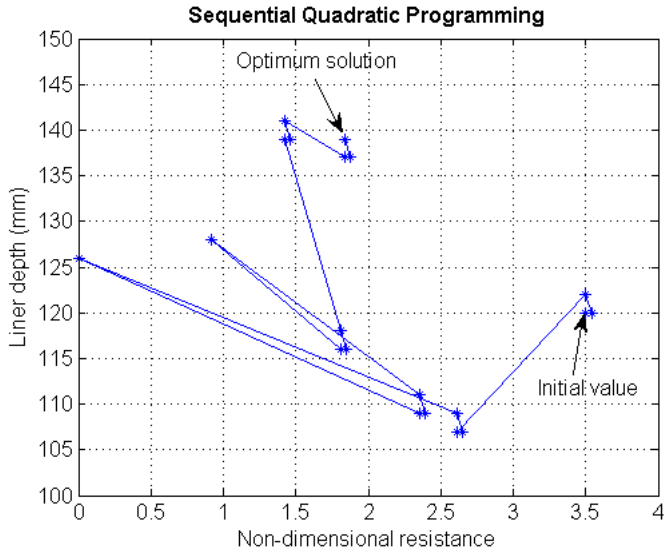

Figure 3.25: SQP search in two dimensions showing initial ($r = 3.5$ and $d = 120$ mm), and optimum ($r = 1.8$ and $d = 139$ mm) characteristics for the absorbing termination.

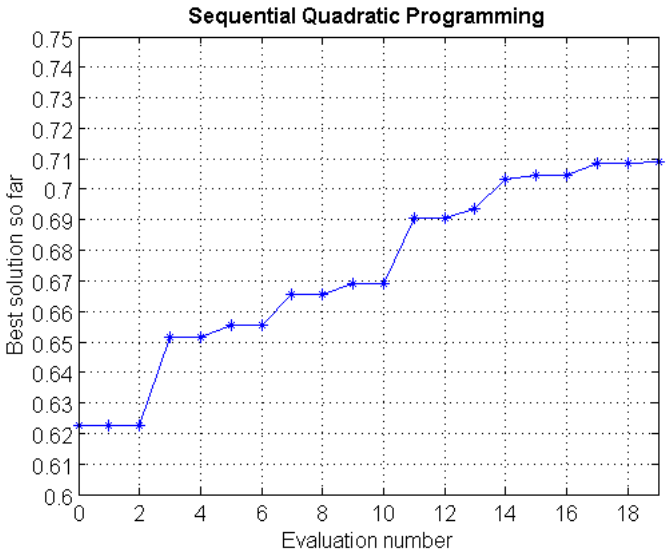

Figure 3.26: Convergence of SQP search towards local optimum absorption coefficient $\bar{\eta} = 0.71$.

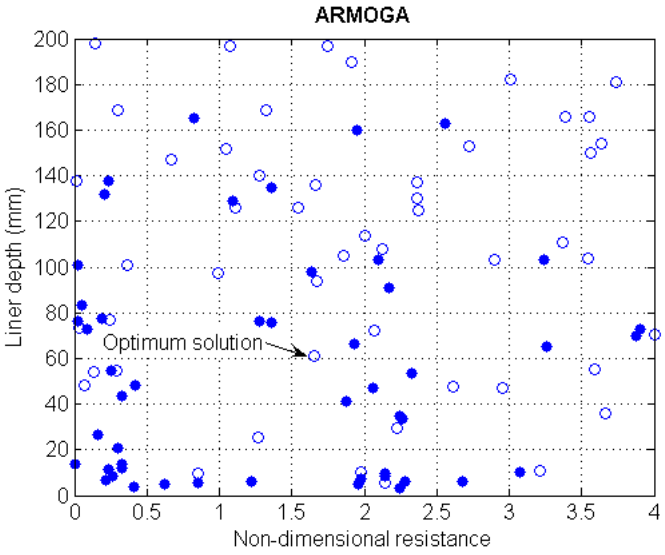

Figure 3.27: ARMOGA search in two dimensions showing starting value ($r = 1.5$ and $d = 126$ mm) and optimum solution ($r = 1.7$ and $d = 61$ mm). Open circles represent designs in initial population and filled circles represent designs in second generation.

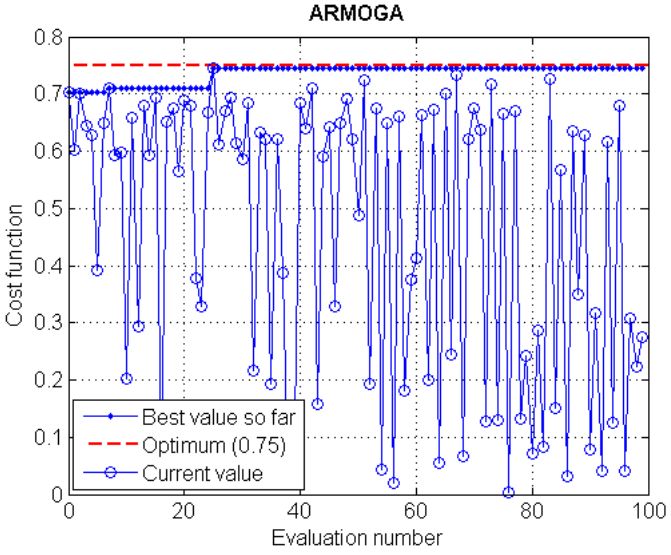

Figure 3.28: Search history for the ARMOGA method, showing the rate of improvement of the cost function (absorption coefficient for multiple frequency multiple mode incidence).

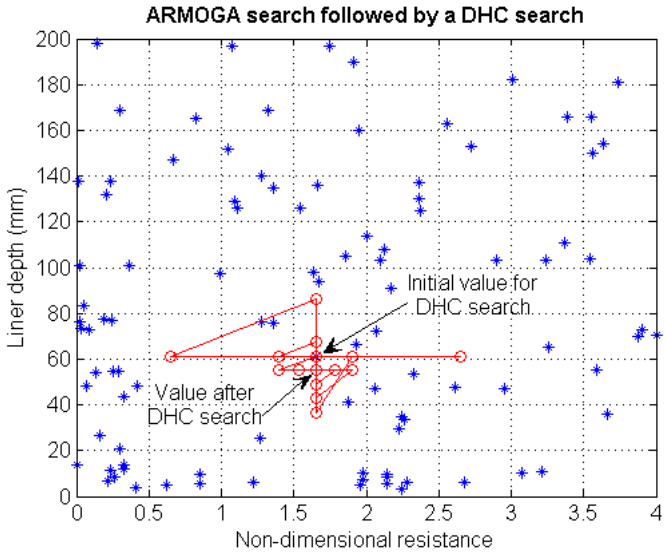

Figure 3.29: ARMOGA search (same as in Figure 3.27), followed by a DHC search with initial step size ($r = 1.0$ and $d = 50$ mm), and minimum step size ($r = 0.125$ and $d = 6.25$ mm).

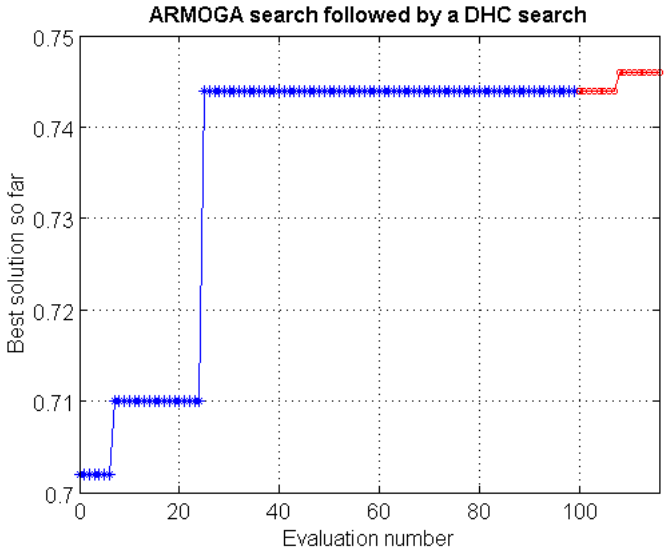

Figure 3.30: ARMOGA search (blue) crosses followed by a DHC search (red) circles, showing refinement of global search with local DHC search to obtain $\bar{\eta} = 0.746 \approx 0.75$.

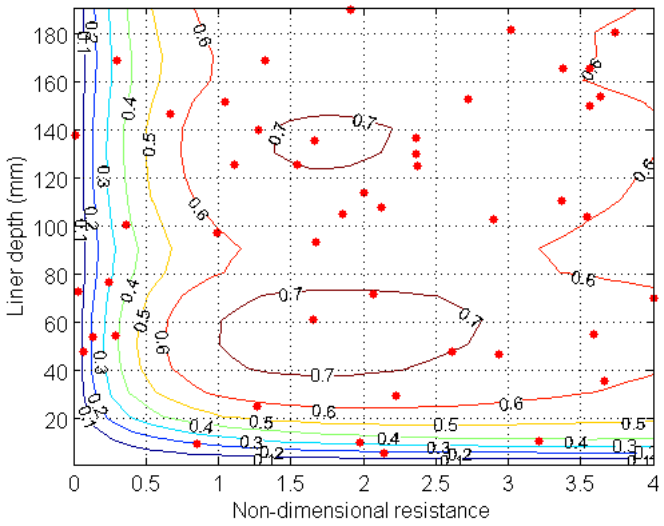

Figure 3.31: Contours of absorption coefficient including 50 DoE points (red dots) from initial population of ARMOGA search.

3.4.6 Discussion

In this section, the resistance and depth of a single cavity liner at the end of a uniform duct have been optimised for the maximum attenuation for diffuse sound field incidence, for a single frequency of 5 kHz, and for a range of frequencies from 20 Hz to 1920 Hz in steps of 100 Hz. For both problems, three search methods are used: DHC, SQP and ARMOGA. A hybrid search consisting of an ARMOGA search followed by a DHC search is also applied for the case of multiple frequencies. In addition, a response surface model is constructed (see Figure 3.32(b)) and then an ARMOGA search is used to search the approximated function to obtain the global optimum, still for the multiple frequency case.

In the single frequency optimisation at 5 kHz, the local methods (DHC and SQP) give maximum absorption coefficients and corresponding optimum impedances that are in good agreement with the result obtained from the contour plot in Figure 3.15. The optimum from the ARMOGA search is in good agreement with the result from the contour plot, even though the local methods (DHC and SQP) are more accurate than ARMOGA as expected. It is worth noting that, because the searches are only performed between a cell

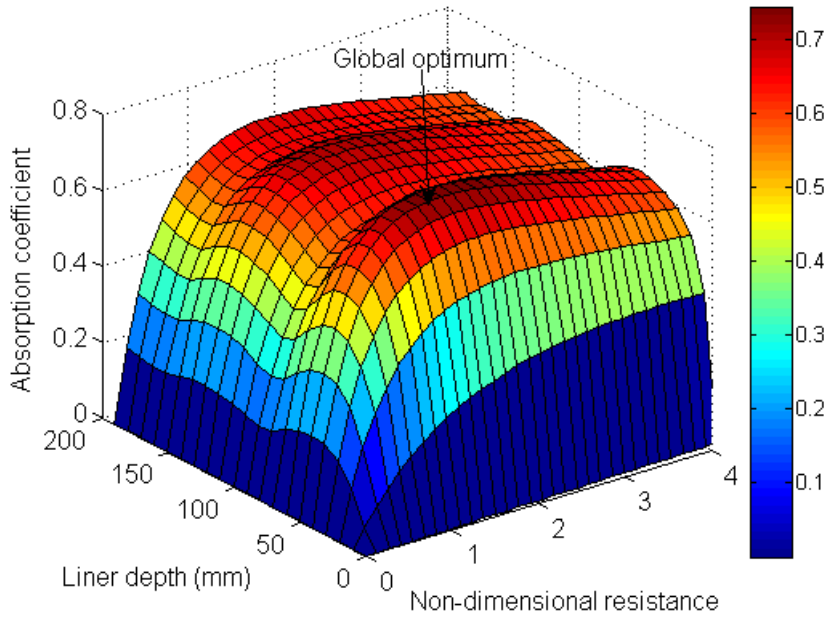

(a) Real function.

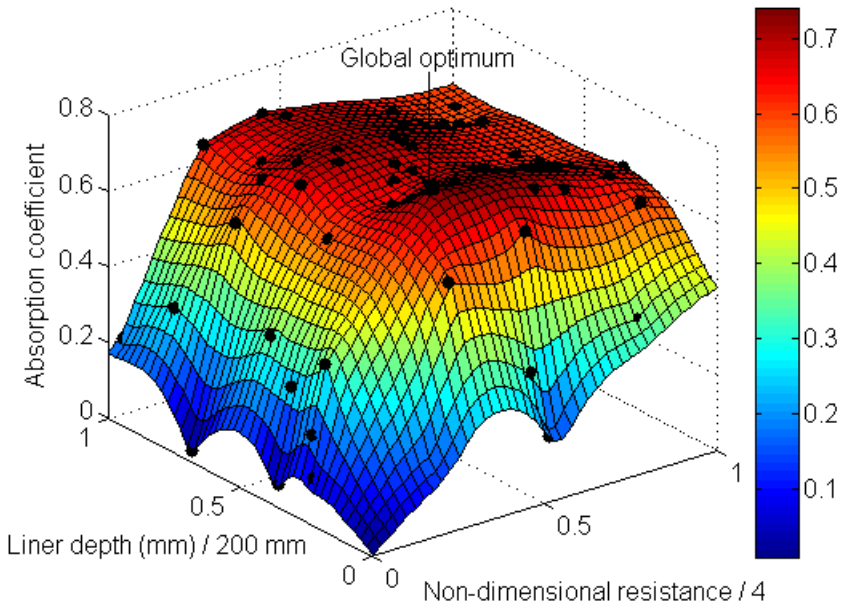

(b) Response surface using linear RBF and DoE points (dots) from Figure 3.31.

Figure 3.32: Real function and response surface constructed using a linear RBF.

depth of 0 mm and 30 mm, the cost function is unimodal, and therefore local searches work satisfactorily effectively. Using the DHC and SQP search methods, the optimum was found after 34 and 40 evaluations respectively (see Figures 3.18 and 3.20). With an ARMOGA search, the optimum was found within 100 evaluations (initial population size of 50 transformed once) as shown in Figure 3.22.

In the multiple frequency optimisation between 20 Hz and 1920 Hz, the local methods (DHC and SQP) are not suitable due to the multimodality of the function. In this light, using either of these methods could lead to the optimiser getting trapped in a local optimum. In the current case, the DHC search found a global peak (Figure 3.23), this is not the case for the SQP method (see Figure 3.25) but it could easily be different depending on the choice of initial values. However, with an ARMOGA search, a global optimum is found within 100 evaluations as shown in Figure 3.28 although the result can be less accurate. A more accurate solution can be obtained using a hybrid search, in which once the global peak is found by ARMOGA, the result can be refined by a local DHC search (see Figures 3.30 and 3.29).

3.5 Conclusion

In this chapter, optimisation algorithms implemented within SOFT have been applied to simple acoustic engineering model problems with known solutions. The aim of this study was to assess the performance of different optimisation algorithms and to establish a robust technique that can be used for similar acoustic optimisation problems in more realistic applications. The following optimisation methods were used in this chapter: DHC, SQP, GA, ARMOGA, SA and RSM. The optimum solution found by the methods in SOFT were benchmarked against results presented in the form of two-dimensional contour plots.

The optimisation results show that the suitability of a method or combination of methods for a given problem clearly depends on the topology of the design space. In cases where the function has a unimodal response, DHC and SQP methods are more efficient than the global methods. The direction taken by local methods such as DHC

and SQP is determined by the topology of the design space in the local vicinity. On the contrary, global methods such as GA, ARMOGA and SA all have some random element which enables them to explore the design space more globally such that they are less likely to get stuck in local optima. For the simple multimodal function, it has also been shown that response surface modelling techniques can be used. However, for complicated design topologies, constructing an accurate response surface can be a non-trivial exercise and usually requires a few updates to the DoE database.

In most practical applications, problems have multiple peaks and hence require a robust optimisation strategy. Using a local method in a multimodal design space, will imply that the end result will heavily depend on the initial value, which is usually a guess. Such an approach is therefore not a robust method of finding the global optimum in problems where multiple optima exist. A more robust approach is an ARMOGA search, which explores the whole design space. Due to the exploratory nature of a global search, the solution is usually not very accurate. In order to obtain a more accurate solution, a global search can be followed by a local search whose level of accuracy can be determined by the input parameters of the algorithm. The use of a hybrid search (a global ARMOGA search followed by a local DHC search) avoids the problem of getting trapped in local optima, at the same time providing a solution of a desired accuracy.

It is important to note that, there is no single optimisation method that is best suited to all problems. Consequently, a good understanding of the problem and sometimes prior knowledge of the design space is essential in choosing a suitable optimisation method. From the assessment of different optimisation algorithms applied to simple acoustic model problems in this chapter, it can be concluded that a hybrid (ARMOGA+DHC) search will make a suitable method to tackle similar problems in this thesis.

Chapter 4

Automatic liner optimisation for bypass ducts

4.1 Introduction

An effective way of reducing aeroengine noise is by using acoustic liners. Acoustic liners are generally made up of a honeycomb panel sandwiched between a porous facing sheet and a rigid backing sheet. In turbofan engines, liners are commonly used in the intake and bypass ducts. The effectiveness of the liner in absorbing sound depends on the frequency and nature of the noise source. However, the honeycomb cell depth and the facing sheet resistance can be tuned to optimise the liner performance for a given engine condition. In this chapter, a finite element shell program B-induct [4], used to predict the liner insertion loss in a bypass duct, has been integrated within a Roll-Royce optimisation suite, SOFT [10], to assess the feasibility of automatic liner optimisation for bypass ducts. The aim is to optimise the resistance and depth of several liner segments simultaneously to maximise the liner insertion loss in a given bypass duct. In the propagation model, the source is assumed to be multimodal with all the propagating modes at each frequency carrying equal acoustic power. To begin with, an idealised (uniform annular) bypass duct is considered and results are obtained for optimising single and multiple liner segments

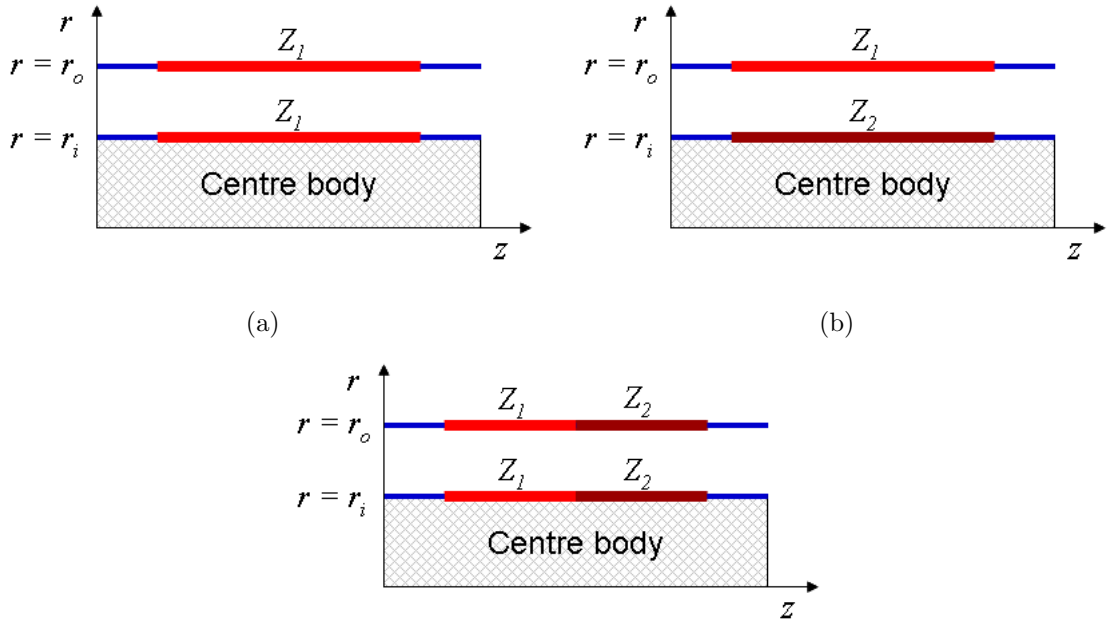

Figure 4.1: Sketch of inner and outer wall of a uniform bypass duct with inner and outer radii r_i and r_o respectively, showing different arrangements of liner impedances Z_1 and Z_2.

by considering the liner insertion loss as a cost function, evaluated at single and multiple frequencies.

A uniform annular duct with different liner distributions is shown in Figure 4.1. Where a single liner segment with two design variables is considered (Figure 4.1(a)), the results from the automatic liner optimisation can be validated by using two-dimensional contour plots of the liner insertion loss as a function of liner resistance and depth. Where multiple liner segments with more than two design variables are considered, the results cannot be validated with two-dimensional contour plots. In this case, the effectiveness of the procedure can be partially validated and assessed by using the fact that, the optimised liner insertion loss for the multiple liner segment optimisation should be the same if not greater than that of the single liner segment optimisation. Results are presented for the following cases:

- A single liner impedance segment on the inner and outer walls (Figure 4.1(a)).

- Two liner impedance segments on opposite sides of the duct walls (Figure 4.1(b)).
- Two liner impedance segments sequentially placed (Figure 4.1(c)).

For these cases, the liner impedances are optimised to maximise the liner insertion loss evaluated at a single frequency.

For the cases with two liner impedances, an alternative approach is also used whereby one of the impedances is fixed at the single liner segment impedance optimum and the other liner impedance optimised. The new optimum is then fixed as the other liner is re-optimised. This iteration is done once and the results are compared to results obtained by optimising two liner impedances simultaneously.

Optimisations are also performed over a range of frequencies. The liner insertion loss is then evaluated at one-third octave centre frequencies. The attenuations evaluated at these frequencies are then used to construct a cost function to optimise the impedance over the frequency range. This will be detailed in section 4.4. Initially, the attenuation is evaluated at one-third octave centre frequencies from 500 Hz to 3150 Hz. A source is assumed with equal acoustic power in each one-third octave band (referred to as a 'uniform power distribution' in this chapter). The cost function can also be modified to include an A-weighting. As a final modification of the cost function, the maximum limit of the frequency range is increased to 10 kHz. The cost of evaluating the sound field increases significantly with frequency, and for this reason a high frequency approximation is used at one-third octave centre frequencies above 3150 Hz. In the next section, the methodology used in this chapter for predicting duct acoustics propagation is reviewed.

4.2 Duct acoustics propagation model

Modern turbofan engines tend to have high bypass ratios (of the order of 10 or greater). The bypass ratio is the ratio of the air mass flow rate through the bypass duct, to the air mass flow rate through the engine core. Fan noise radiated from the bypass duct is therefore a very significant noise source since the bypass duct provides a large open

channel for fan noise to propagate and radiate into the far field. The prediction of sound propagation through bypass ducts depends upon the duct geometry, the mean flow, the acoustic treatment and the noise source. In this section, a finite element method based on the solution of the convected wave equation is used to describe the acoustic field in the bypass duct and to predict the transmission of acoustic power from the fan stage to the exhaust plane. If the mean flow is assumed to be irrotational, the problem can be formulated in terms of a convected wave equation in the acoustic velocity potential, and solved in the frequency domain using finite elements [56–58]. The liner impedance boundary condition on the duct walls is applied by assuming an infinitely thin boundary layer over the impedance surface [93].

4.2.1 Liner model

The most common construction for a turbofan liner is a curved panel formed from a layer of honeycomb material which is separated from the flow by a porous facing sheet (as shown in Figure 4.2). The basic mechanism of sound absorption by turbofan duct liners depends on the conversion of acoustic energy to heat by viscous dissipation. An acoustic pressure field due to an acoustic disturbance incident on an acoustically lined portion of the duct wall drives air through apertures in a porous facing sheet. Acoustic energy is either dissipated directly by viscous forces in the aperture or converted into vortical kinetic energy. The device is locally reacting since the pressure field in each cell is independent of that in its neighbours. The basic absorption mechanism for a pressure disturbance propagating along the surface is illustrated in Figure 4.2. The acoustic performance is characterised by the specific acoustic impedance, $Z(\omega)$ defined as the ratio p/u where p and u are the complex pressure amplitude at the surface, and the complex mean velocity amplitude normal to the surface, respectively, for pressure fluctuations at a given frequency ω. For a single cavity liner as shown in Figure 4.2,

$$Z\left(\omega\right)/\rho c = r + i\left(kl - \cot(kd)\right) \tag{4.1}$$

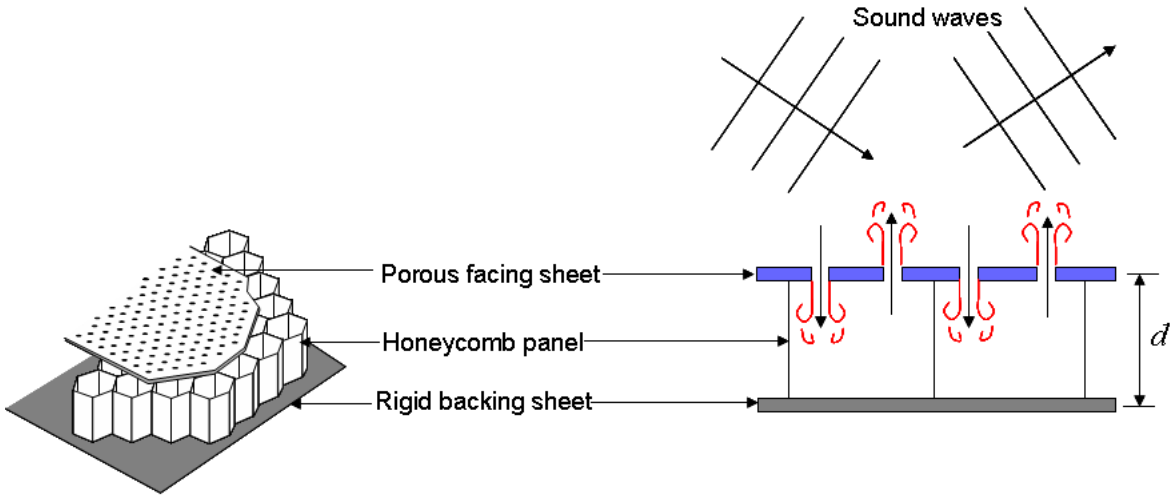

Figure 4.2: Single cavity liner model showing, movement of sound waves in and out of perforate holes.

where r is the (non-dimensional) resistance of the facing sheet, $k(=\omega/c)$ is the acoustic wave number, l is the mass inertance of the facing sheet, d is the cavity depth, ρ is the density and c is the sound speed. The acoustic performance of the liner depends upon frequency (through the parameter k) and can be tuned to absorb acoustic energy from specific regions of the source spectrum by judicious choice of cell depth and the facing sheet resistance. The mass inertance l, depends on the thickness and porosity of the facing sheet (see Motsinger and Kraft [94]). In the results presented in this chapter, a mass inertance $l = 0.014$ m, typical of current liner designs is used. The resistance r depends on a number of parameters including the percentage open area, the hole diameter, facing sheet thickness, grazing flow Mach number and normal velocity amplitude [94].

4.2.2 Governing equations

The fundamental physical principles of fluid dynamics and acoustics are, the conservation of mass, the conservation of momentum and the conservation of energy. In the case of a compressible gas, an equation of state is also required. The assumption of a perfect gas (intermolecular forces are negligible), is often used. For a compressible fluid the full set

of governing flow equations including the equation of state are referred to as the Navier-Stokes equations.

The equation of continuity of mass (continuity equation) can be written as:

$$\frac{\partial \rho^*}{\partial t} + \mathbf{u}^* \cdot \nabla \rho^* + \rho^* \nabla \cdot \mathbf{u}^* = 0 \tag{4.2}$$

where $\mathbf{u}^*$, ρ^* and p^* are the total unsteady velocity, density and pressure respectively and t is time. In the Navier-Stokes equations for a viscous flow, the transport phenomena of friction, thermal conduction and/or mass diffusion are included. With these transport phenomena, the entropy of the flow will always increase due to their dissipative nature.

In an inviscid flow however, where these transport phenomena can be neglected, the Navier-Stokes equations reduce to the Euler equations. The momentum equations for an inviscid flow in the absence of body forces can therefore be written as:

$$\frac{\partial \mathbf{u}^*}{\partial t} + \mathbf{u}^* \cdot \nabla \mathbf{u}^* = -\frac{1}{\rho^*} \nabla p^*. \tag{4.3}$$

In all that follows, it will be assumed that the total unsteady flow variables can be decomposed into a steady mean flow component and a small-amplitude, unsteady perturbation component. This implies that the total unsteady flow variables u^*, ρ^* and p^* can be expressed as:

$$\mathbf{u}^*(\mathbf{x}, t) = \mathbf{u}_0(\mathbf{x}) + \mathbf{u}(\mathbf{x}, t), \tag{4.4}$$

$$p^*(\mathbf{x}, t) = p_0(\mathbf{x}) + p(\mathbf{x}, t), \tag{4.5}$$

$$\rho^*(\mathbf{x}, t) = \rho_0(\mathbf{x}) + \rho(\mathbf{x}, t), \tag{4.6}$$

where $\mathbf{u}_0$, p_0 and ρ_0 are the steady mean flow variables and $\mathbf{u}$, p and ρ are the small-amplitude unsteady perturbations, and $\mathbf{x}$ is a position in space. By linearising the small-amplitude unsteady perturbation on the steady mean flow and ignoring second and higher order terms, the linearised continuity and momentum equations, or the Linearised Euler Equations (LEE) are obtained. The linearised continuity equation can be written as:

$$\frac{\partial \rho}{\partial t} + \nabla \cdot (\mathbf{u}_0 \rho + \rho_0 \mathbf{u}) = 0. \tag{4.7}$$

Similarly, the linearised momentum equation can be written as:

$$\frac{\partial \mathbf{u}}{\partial t} + (\mathbf{u}_0 \cdot \nabla)\mathbf{u} + (\mathbf{u} \cdot \nabla)\mathbf{u}_0 + \frac{\rho}{\rho_0}(\mathbf{u}_0 \cdot \nabla)\mathbf{u}_0 = -\frac{1}{\rho_0}\nabla p. \tag{4.8}$$

For an irrotational flow (zero vorticity), the total unsteady velocity $\mathbf{u}^*$ can be expressed as the gradient of the total unsteady velocity potential ϕ^*, such that:

$$\mathbf{u}^* = \nabla\phi^*, \tag{4.9}$$

$$\mathbf{u}_0 = \nabla\phi_0, \tag{4.10}$$

$$\mathbf{u} = \nabla\phi. \tag{4.11}$$

For isentropic gas flow, the equation of state reduces to:

$$p^* = K\rho^{*\gamma}, \tag{4.12}$$

where K is a proportionality constant and γ is the ratio of specific heats in the usual notation, C_P/C_V (specific heat capacity at constant pressure/specific heat capacity at constant volume). The unsteady pressure and density perturbations are then related by:

$$p = c_0^2\rho \tag{4.13}$$

where c_0 is the local sound speed in the mean flow and $c_0^2 = \gamma p_0/\rho_0$.

Substituting Equations (4.10) and (4.11) into Equation (4.7) gives the irrotational acoustic continuity equation in terms of the acoustic velocity potential ϕ:

$$\frac{\partial \rho}{\partial t} + \nabla \cdot (\rho\nabla\phi_0 + \rho_0\nabla\phi) = 0. \tag{4.14}$$

The linearised momentum equation can be replaced by the unsteady form of Bernoulli's equation [95]:

$$-\rho_0\left(\frac{\partial \phi}{\partial t} + \nabla\phi_0 \cdot \nabla\phi\right) = p. \tag{4.15}$$

Using Equations (4.13), (4.14), (4.15) the convected Helmholtz equation is given by:

$$(i\omega + \mathbf{u}_0 \cdot \nabla)\left[\frac{\rho_0}{c_0^2}(i\omega + \mathbf{u}_0 \cdot \nabla)\phi\right] - \nabla \cdot (\rho_0\nabla\phi) = 0. \tag{4.16}$$

The impedance boundary condition

In a bypass duct with hard or lined walls, in order to obtain the solutions of the acoustic field equations, the boundary condition of the wall needs to be specified. For a duct lined with a locally reacting liner, the relationship between the acoustic pressure p and normal component of the acoustic particle velocity u at the duct wall is given by:

$$\frac{p}{u} = Z \tag{4.17}$$

where Z is the specific acoustic impedance of the liner. For a hard-walled duct u is zero at the wall and $|Z| \to \infty$.

In this chapter, the effect of acoustic liners in the prediction is based on the presence of an infinitely thin boundary layer at the impedance surface, which is modelled by Eversman's [96] implementation of the Myers [93] boundary condition. For time-harmonic dependence, the complex acoustic pressure varies like $e^{i\omega t}$ and the Myers boundary condition is given by:

$$\mathbf{u} \cdot \mathbf{n} = \nabla\phi \cdot \mathbf{n} = \frac{p}{Z} + \left(\frac{1}{i\omega}\right) \mathbf{u}_0 \cdot \nabla \left(\frac{p}{Z}\right) - \left(\frac{p}{i\omega Z}\right) \mathbf{n} \cdot (\mathbf{n}.\nabla \mathbf{u}_0), \tag{4.18}$$

where $\mathbf{n}$ is a normal vector on the impedance surface and ω is the angular frequency of excitation.

Solution of Equation (4.16) for uniform mean flow

For the case of a uniform mean flow along the duct axis where,

$$\mathbf{u}_0 = (0, 0, U_0) \tag{4.19}$$

Equation (4.16) reduces to:

$$\nabla^2\phi - \frac{1}{c_0^2}\left(\frac{\partial}{\partial t} + U_0\frac{\partial}{\partial z}\right)^2 \phi = 0. \tag{4.20}$$

For time-harmonic dependence where the acoustic velocity potential varies like $e^{i\omega t}$, this reduces to the convected Helmholtz equation:

$$\nabla^2\phi - M^2\frac{\partial^2\phi}{\partial z^2} - 2ikM\frac{\partial\phi}{\partial z} + k^2\phi = 0, \tag{4.21}$$

where $k = {}^{\omega}/_{c_0}$ is the wave number of the acoustic wave and $M = {}^{U_0}/_{c_0}$ is the axial Mach number. In cylindrical coordinates (r,θ,z) as illustrated in Figure 4.3, the equation can be written as follows:

$$\frac{\partial^2\phi}{\partial r^2} + \frac{1}{r}\frac{\partial\phi}{\partial r} + \frac{1}{r^2}\frac{\partial^2\phi}{\partial\theta^2} + (1-M^2)\frac{\partial^2\phi}{\partial z^2} - 2ikM\frac{\partial\phi}{\partial z} + k^2\phi = 0. \tag{4.22}$$

It can be shown that the same equation holds when ϕ is replaced by the acoustic pressure p.

Duct modes

In a uniform duct, the sound field can be expressed in specific solutions called modes. Consider a cylindrical duct with an annular cross-section (as in a bypass duct) as shown in Figure 4.3. The solution of Equation (4.22) for the acoustic velocity potential can be obtained as a summation of modes (see reference [9] for details):

$$\phi(r,\theta,z) = \sum_{m=-\infty}^{\infty}\sum_{n=1}^{\infty}\left(AJ_{|m|}(k_{rmn}r) + BY_{|m|}(k_{rmn}r)\right)e^{im\theta}\left(a^{+}_{mn}e^{-ik^{+}_{zmn}z} + a^{-}_{mn}e^{-ik^{-}_{zmn}z}\right), \tag{4.23}$$

where m is the circumferential mode order, n is the radial order, J_m and Y_m are Bessel and Neumann functions of order m, respectively, k_{rmn} is the radial wave number, while ${k^{+}}_{zmn}$ and ${k^{-}}_{zmn}$ are axial wave numbers. Consider a single mode (m, n), the '$+$' and '$-$' superscripts represent a mode propagating in the positive and negative z-directions respectively, with mode amplitude a_{mn}.

For a given mode (m, n),

$$\phi_{mn}(r,\theta,z) = A^{\phi}_{mn}N_{mn}(AJ_{|m|}(k_{rmn}r) + BY_{|m|}(k_{rmn}))e^{im\theta}e^{-ik_{zmn}z}, \tag{4.24}$$

or terms of acoustic pressure:

$$p_{mn}(r,\theta,z) = A^{p}_{mn}N_{mn}(AJ_{|m|}(k_{rmn}r) + BY_{|m|}(k_{rmn}))e^{im\theta}e^{-ik_{zmn}z}, \tag{4.25}$$

where N_{mn} is a normalisation factor and A^{ϕ}_{mn} and A^{p}_{mn} are modal amplitudes corresponding to the velocity potential and pressure respectively, where A^{ϕ}_{mn} and A^{p}_{mn} are related through:

$$A^{\phi}_{mn} = \frac{A^{p}_{mn}}{-i\rho_0 c_0\left(k - Mk_{zmn}\right)}. \tag{4.26}$$

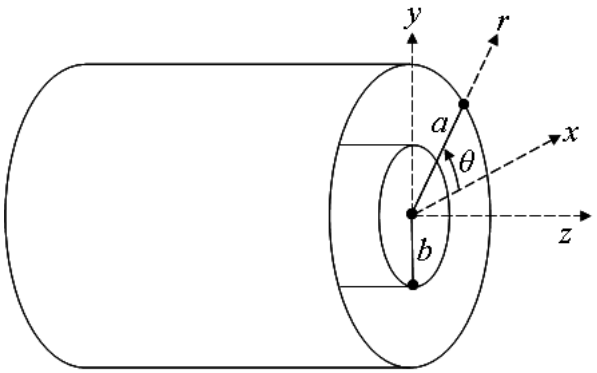

Figure 4.3: Uniform annular duct with outer radius a and inner radius b.

For an annular duct, with a hard wall at the outer radius a and at the inner radius b, the radial wave number k_{rmn}, can be obtained by imposing hard wall boundary conditions at $r = a$ and $r = b$:

$$\left.\frac{\partial\phi}{\partial r}\right|_{r=a} = 0, \tag{4.27}$$

$$\left.\frac{\partial\phi}{\partial r}\right|_{r=b} = 0. \tag{4.28}$$

Once the radial wave number k_{rmn} has been obtained, the axial wave numbers ${k^+}_{zmn}$ and ${k^-}_{zmn}$ can be determined by using the dispersion relation:

$$k^+_{zmn} = \frac{-kM + \sqrt{k^2 - \beta^2 k^2_{rmn}}}{\beta^2}, \tag{4.29}$$

$$k^-_{zmn} = \frac{-kM - \sqrt{k^2 - \beta^2 k^2_{rmn}}}{\beta^2}, \tag{4.30}$$

where $\beta = \sqrt{1 - M^2}$.

From Equations (4.29) and (4.30), the axial wavenumber can either be real or imaginary depending on the value of the free-space wave number k in the term $k^2 - \beta^2 k^2_{rmn}$. For a given mode, when this term is positive and the axial wave number is purely real the mode is propagating (cut-on). When this term is negative and the axial wave number has a non-zero imaginary part, the mode is evanescent (cut-off).

It follows that, for a given mode (m, n), the minimum frequency (cut-off or cut-on

frequency) ω_{co}, at which a mode is said to be propagating is given by:

$$\omega_{co} = c_0 k_{rmn} \sqrt{1 - M^2}. \tag{4.31}$$

Modal intensity

The average modal intensity [97] for a mode (m, n) is given by:

$$I_{mn} = \frac{1}{2} \frac{\left|A^p_{mn}\right|^2}{\rho_0 c_0 \left|k - M k_{mn}\right|^2} \left(\mathrm{Re}\left(k_{mn}\right) k \left(1 + M^2\right) + M \left|k - M k_{mn}\right|^2 - M^3 \left|k_{mn}\right|^2 \right). \tag{4.32}$$

From Equations (4.25) and (4.32), the average modal intensity I_{mn} is proportional to the square of the magnitude of the modal acoustic pressure p_{mn}:

$$I_{mn} \propto \left|p_{mn}\right|^2. \tag{4.33}$$

This relationship is used later in this thesis to modify modal power distributions used in the propagation model, to match measured data.

The modes described by Equations (4.24) and (4.25) are orthogonal, which implies that the total acoustic power for a number of modes can be obtained simply by summing the powers of individual modes since cross-terms are zero. This is used later in this chapter to calculate the total incident and transmitted acoustic powers in the bypass duct.

4.2.3 Computational method

As shown in section 4.2.2, a sound field within a uniform bypass duct can be described in terms of acoustic modes. Analytical solutions of the acoustic pressure field in such a bypass duct can be represented as summations of modes for hard-walled and lined duct configurations. The ease of obtaining analytical solutions of the acoustic pressure field in this way is however limited to uniform circular and annular duct geometries with axisymmetric liners. For axially non-uniform duct geometries and/or non-axisymmetric liners, analytical solutions for the acoustic pressure field cannot be obtained in this way. In such cases numerical methods must be used to solve the governing flow equations. In this chapter, a numerical procedure developed for arbitrary duct geometries and axisymmetric liners is used to predict sound propagation and absorption in bypass ducts, for the

purposes of optimising liner impedances.

The numerical scheme is based on a finite element model [98] for the duct. The solution domain is divided into smaller regions called finite elements in which the acoustic field equations can be represented in terms of values at specified nodal points. This is termed a finite element model. The behaviour over the entire domain can then be determined by assembling a set of global equations with contributions from each element. The process of dividing the domain into a finite number of elements is known as discretisation. The elements are connected at points called nodes, and a requirement of the discretisation is that the solution is continuous across the boundaries of adjacent elements.

In the rest of the chapter, a brief explanation of the application of the finite element (FE) method is presented. The FE method is used to solve the acoustic field equations within a bypass duct. Results from impedance optimisations performed using the FE method integrated within the SOFT optimisation suite are presented.

The variational formulation

The FE model is based on a variational formulation. To obtain an approximate solution of the convected wave equation, the equation and boundary conditions need not be satisfied at every point in the domain. A solution which satisfies the equations in an approximate way can be found such that the weighted average of the error is zero. This is achieved by using a weighted residual technique [99] applied to the irrotational acoustic continuity equation (Equation (4.14)). The linearised momentum equation (4.15) is explicitly satisfied by the approximate solution. For time-harmonic dependence where the acoustic variables p, ρ and ϕ vary like $e^{i\omega t}$, Equation (4.14) can be re-written as:

$$i\omega\rho + \nabla \cdot (\rho \mathbf{u_0} + \rho_\mathbf{0} \nabla\phi) = 0. \tag{4.34}$$

If $\tilde{\rho}$ and $\tilde{\phi}$ are approximate solutions of Equation (4.34), then:

$$i\omega\tilde{\rho} + \nabla \cdot \left(\tilde{\rho}\mathbf{u_0} + \rho_\mathbf{0} \nabla\tilde{\phi}\right) = \varepsilon \neq 0, \tag{4.35}$$

where ε is the error (or residual) when the approximate solution is substituted into the equation. A solution can be obtained by ensuring that the weighted average of the residual

is zero over the computational domain. This is achieved by multiplying Equation (4.35) by the weighting function $W(\mathbf{x})$ and integrating over the domain volume V to give:

$$\int_V W\left(i\omega\tilde{\rho} + \nabla\cdot\left(\tilde{\rho}\mathbf{u_0} + \rho_\mathbf{0}\nabla\tilde{\phi}\right)\right)dV = 0, \quad \forall W. \tag{4.36}$$

Applying the divergence theorem, Equation (4.36) can be re-written as:

$$\int_V \left(\nabla W\cdot\left(\tilde{\rho}\mathbf{u}_0 + \rho_0\nabla\tilde{\phi}\right) - Wi\omega\tilde{\rho}\right)dV = \int_S W\left(\tilde{\rho}\mathbf{u}_0 + \rho_0\nabla\tilde{\phi}\right)\cdot\mathbf{n}dS, \quad \forall W, \tag{4.37}$$

where S is the surface of the domain, and $\mathbf{n}$ is a normal on the surface pointing outwards.

Using the unsteady form of the Bernoulli's equation (4.14) and the equation of state (4.13), an expression for the acoustic density ρ can be obtained in terms of the acoustic velocity potential ϕ. For time-harmonic dependence the expression for the acoustic density is given by:

$$\rho = -\frac{\rho_0}{c_0^2}\left(i\omega\phi + \mathbf{u_0}\cdot\nabla\phi\right). \tag{4.38}$$

Equivalently, the approximate acoustic density $\tilde{\rho}$, is given by:

$$\tilde{\rho} = -\frac{\rho_0}{c_0^2}\left(i\omega\tilde{\phi} + \mathbf{u_0}\cdot\nabla\tilde{\phi}\right). \tag{4.39}$$

The approximate acoustic density can be substituted into Equation (4.37) to obtain a variational formulation:

$$\begin{aligned}\int_V \frac{\rho_0}{c_0^2}(c_0^2\nabla W\cdot\nabla\tilde{\phi} - (\mathbf{u}_0\cdot\nabla W)(\mathbf{u}_0\cdot\nabla\tilde{\phi}))dV \\ + \int_V \frac{\rho_0}{c_0^2}(i\omega[W(\mathbf{u}_0\cdot\nabla\tilde{\phi}) - (\mathbf{u}_0\cdot\nabla W)\tilde{\phi}] - \omega^2 W\tilde{\phi})dV \\ = \int_S \frac{\rho_0}{c_0^2}((-i\omega\tilde{\phi} - \mathbf{u}_0\cdot\nabla\tilde{\phi})W\mathbf{u}_0 + Wc_0^2\nabla\tilde{\phi})\cdot\mathbf{n}dS, \quad \forall W.\end{aligned} \tag{4.40}$$

Equation (4.40) is an integral equation for $\tilde{\phi}$ over the domain in terms of surface integrals and volume integrals. For a hard wall boundary, $\mathbf{u}_0\cdot\mathbf{n} = 0$ and $\nabla\tilde{\phi}\cdot\mathbf{n} = 0$. The right

hand side of Equation (4.40) is then zero. For a lined duct however, only $\mathbf{u}_0 \cdot \mathbf{n} = 0$ and the Myers boundary condition must be implemented for $\nabla\tilde{\phi} \cdot \mathbf{n}$ (see Equation (4.18)) [96]. At the inlet and outlet planes of the duct, $\nabla\tilde{\phi} \cdot \mathbf{n}$ is specified in terms of modes. An approximate solution for the variational problem is then obtained by assuming that the acoustic velocity potential $\tilde{\phi}$ has the form [98]:

$$\tilde{\phi} = \sum_{i=1}^{n} \alpha_i(\mathbf{x}) q_i, \tag{4.41}$$

where $\alpha_i(\mathbf{x})$ are trial functions of position $\mathbf{x}$, and q_i is an unknown parameter. The trial functions $\alpha_i(\mathbf{x})$ must be continuous over the solution domain and have a finite first derivative. The weighting function $W(\mathbf{x})$ is commonly chosen to be the same as the trial function $\alpha_i(\mathbf{x})$ (Galerkin method).

Finite element method

In the finite element model based on the above formulation, the trial functions $\alpha_i(\mathbf{x})$ are chosen to be shape functions of the mesh [100]. The variation of $\tilde{\phi}$ over the finite element problem domain can therefore be given by:

$$\tilde{\phi} = \sum_{i=1}^{n} N_i(\mathbf{x})\, \tilde{\phi}_i = [N] \left\{ \tilde{\phi} \right\}, \tag{4.42}$$

where n is the number of nodes in the problem domain, $[N]$ is a row matrix $[N_1(\mathbf{x}), N_2(\mathbf{x}) \ldots N_n(\mathbf{x})]$ with global shape functions, $\left\{ \tilde{\phi} \right\}$ is a column matrix $\left\{ \tilde{\phi}_1, \tilde{\phi}_2 \ldots \tilde{\phi}_n \right\}^T$ which contains nodal values of the acoustic velocity potential. Similarly, the weighting function is given by:

$$W_i(\mathbf{x}) = N_i(\mathbf{x}). \tag{4.43}$$

Substituting expressions (4.42) and (4.43) into the variational formulation in Equation (4.40), and putting the contribution from each element together gives an equation in terms of global matrices of the form:

$$\left[\mathbf{K} - \omega^2 \mathbf{M} + i\omega \mathbf{C} \right] \left\{ \tilde{\phi}_n \right\} = \mathbf{F} \tag{4.44}$$

where, **K**, **M**, **C** and **F** are the acoustic stiffness, mass, damping and forcing matrices respectively, which are determined by the shape functions and the boundary conditions for the problem domain. The damping matrix contains the information from the impedance boundary conditions imposed for the problem, while the forcing matrix contains information from the modal boundary conditions. The column vector $\left\{\tilde{\phi}_n\right\}$ contains nodal values of the acoustic velocity potential for the whole domain volume V. Details of this formulation can be found in reference [100].

The solution of the acoustic velocity potential can thus be obtained by solving Equation (4.44). For all results presented, a commercial FE code ACTRAN/TM [9] is used to obtain the solution for the acoustic velocity potential $\tilde{\phi}$ in the whole acoustic domain. Once the nodal values of $\tilde{\phi}$ are obtained, variables such as $\tilde{p}$ and $\tilde{\rho}$ can be calculated at any point within the computational domain. ACTRAN/TM will be used within a shell program called B-induct developed by Sugimoto [4].

4.2.4 B-induct

B-induct [4] is a shell program used to perform ACTRAN/TM [9] analysis of the induct domain of axisymmetric bypass ducts. It automatically produces input files for ACTRAN/TM from parameters specified in a simple file format, executes the ACTRAN/TM finite element code for a prescribed set of frequencies and modes and then extracts results from the ACTRAN/TM output files.

In order to run B-induct, the configuration of the problem must be defined. This is done through a number of parameters specified by the user. These parameters are prescribed in three files: a geometry file, a condition file and an impedance file. In the geometry file, the radial and axial coordinates of the inner and outer walls of the bypass duct geometry are defined. The geometry file also contains definitions of the liner extents on the duct walls and defines the appropriate impedance file. The impedance file contains non-dimensional impedance data as a function of frequency. In the condition file, the mean flow and acoustic parameters associated with the engine operating condition are

defined at the input plane. The mean flow parameters defined are: the Mach number M, the stagnation sound speed c_s and the stagnation fluid density ρ_s. In the condition file, the mesh resolution is controlled by the number of radial elements, the number of axial elements and the order of the finite elements, which can all be specified by the user. Second order quadratic elements are used to obtain the solutions presented in this thesis. Typically, ten nodes per wavelength are used to resolve the acoustic field for each frequency. In the condition file the number of azimuthal and radial mode orders to be considered in the acoustic analysis are also specified.

Once the duct configuration is defined, B-induct then creates the wall curves of the duct using B-spline interpolation. A sufficient number of points must be used for the inner and outer wall curves to accurately define the duct geometry. B-induct also creates the in-duct mesh by using 8-node quadratic quadrilateral finite elements. Figure 4.4 shows a uniform bypass duct with a regular FE mesh in the in-duct domain. Once the mesh is created the mean flow field is obtained from a steady Euler calculation. B-induct solves the compressible Euler equations by using finite element (FE) analysis to calculate the mean velocity potential. The associated mean velocity components are then interpolated unto the FE mesh to be used for the acoustic analysis.

For the acoustic analysis, ACTRAN input files are automatically created. Modal boundary conditions are imposed at the duct input and duct exhaust planes, and the sound field at each of these planes is defined in terms of hard-walled annular duct modes (see Equation (4.24)). At the input plane, the acoustic intensity for each of the incident modes is prescribed. These modes are reflected, absorbed and scattered by the geometry variation (in the case of a non-uniform duct) and lined surfaces within the bypass duct. The non-dimensional impedance data specified on the duct walls are converted to dimensional admittance values. These values are imposed on the faces of elements which bound the impedance surface to incorporate the liner impedance boundary condition in the model. ACTRAN/TM is run by B-induct for all the frequencies specified and for all the cut-on modes propagating at the duct input plane. B-induct then extracts the reflected and transmitted modal intensities at the input and exhaust planes from the AC-

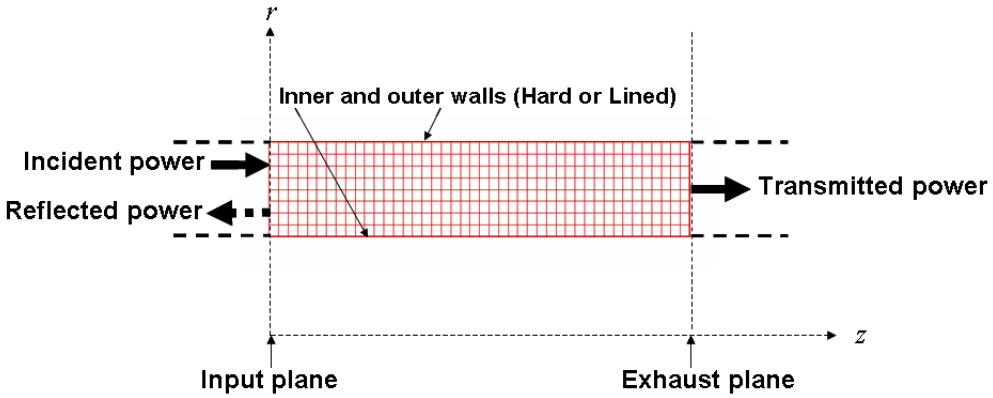

Figure 4.4: An FE mesh generated by B-induct for a uniform annular duct.

TRAN output file and writes them into a 'power transmission' file, at each frequency.

In the 'power transmission' file produced by B-induct, the incident, reflected and transmitted modal intensities from all the propagating modes are listed. The cross-sectional areas at the input and exhaust planes are also included, from which the corresponding incident modal power P_I, reflected modal power P_R and transmitted modal power P_T are obtained. In most instances the incident modes are assumed to carry equal acoustic power P and to be uncorrelated. In this study, in which the duct geometry is axisymmetric, acoustic power transfer between modes (scattering) cannot occur between circumferential mode orders m. However, scattering occurs between radial mode orders n.

Given a total incident power at the input plane P_I, and a total transmitted power at the exhaust plane P_T, the liner insertion loss of the acoustic liner is given by:

$$\Delta PWL = 10 \log_{10} \left(\frac{P_{T(HW)}}{P_{T(Lined)}} \right), \tag{4.45}$$

where subscripts 'HW' and '$Lined$' represent hard-walled and lined ducts, and the acoustic power $P = IA$ where I is the acoustic intensity and A is the cross-sectional area of the modal boundary. Since the cross-sectional area at the exhaust plane is the same for the hard-walled and lined ducts, expression (4.45) can be re-written as:

$$\Delta PWL = 10 \log_{10} \left(\frac{I_{T(HW)}}{I_{T(Lined)}} \right), \tag{4.46}$$

where I_T is the total transmitted intensity at the exhaust plane.

4.3 The source power distribution

At a given frequency, the source is assumed to consist of uncorrelated modes with equal (acoustic) power in each mode, with all the cut-on modes present. When a range of 1/3-octave centre frequencies is considered, the source is assumed to consist of a uniform power[1] distribution across 1/3-octave bands.

In the B-induct calculation, all the propagating modes at each frequency are given a unit intensity. A uniform power distribution across 1/3-octave bands can be represented by normalising this unit incident modal intensity (hence incident modal power) at each frequency by using the number of propagating modes N at that frequency (N_j say). At each frequency the normalised incident modal intensity $\tilde{I}^j$ for each mode will be given by:

$$\tilde{I}^j = \frac{1}{N_j}. \tag{4.47}$$

The total incident intensity $\tilde{I}_I^j$ at the jth frequency summed over all modes is given by:

$$\tilde{I}_I^j = \frac{1}{N_j}.N_j = 1. \tag{4.48}$$

This implies that the total incident intensity I_I for a source with a uniform power distribution summed over n 1/3-octave centre frequencies is given by:

$$I_I = n. \tag{4.49}$$

Similarly, the total transmitted intensity I_T for a source corresponding to unit total intensity at each 1/3-octave centre frequency is given by:

$$I_T = \sum_{j=1}^{n} \frac{I_T^j}{N_j}, \tag{4.50}$$

where I_T^j is the total transmitted intensity at the jth 1/3-octave centre frequency, for unit modal intensities in each mode.

[1]Uniform power in this context means, assuming equal power in each one-third octave band which is concentrated at the one-third octave centre frequency.

4.4 Cost function

The cost function used in the liner optimisation process in this chapter is the liner insertion loss ΔPWL given by expression (4.45) or (4.46).

For a single frequency, ΔPWL can be evaluated simply by substituting expression (4.50) for hard-walled and lined ducts at a given frequency into expression (4.46).

For multiple frequencies, the total transmitted intensity I_T is calculated either as the sum of transmitted intensities at each frequency or as the weighted sum of transmitted intensities using an A-weighting (see Figure 4.5), such that:

$$I_{T(HW)} = \sum_{j=1}^{n} \frac{I^j_{T(HW)}}{N_j} \quad \text{and} \quad I_{T(Lined)} = \sum_{j=1}^{n} \frac{I^j_{T(Lined)}}{N_j}, \tag{4.51}$$

or

$$I^{Awt}_{T(HW)} = \sum_{j=1}^{n} A_j \frac{I^j_{T(HW)}}{N_j} \quad \text{and} \quad I^{Awt}_{T(Lined)} = \sum_{j=1}^{n} A_j \frac{I^j_{T(Lined)}}{N_j}, \tag{4.52}$$

where the superscript 'Awt' represents A-weighted values and $A_j = 10^{a_j/10}$ where a_j is the A-weighting factor in dB at the jth frequency (see Figure 4.5).

4.5 Liner optimisation using SOFT

The liner impedance in the bypass duct problem is optimised using global and local search algorithms within the Rolls-Royce optimisation suite, SOFT. SOFT provides a link between simulation code(s) and a library of optimisation algorithms. In this chapter, the simulation code used within SOFT is B-induct. Starting from an initial liner resistance and depth, B-induct is run within SOFT to obtain the liner insertion loss in the duct (see expression (4.46)). Depending on the optimisation algorithm, the resistances and depths for successive evaluations can either be chosen deterministically or stochastically. Figure 4.6 illustrates the optimisation process using B-induct as a simulation code within the SOFT optimisation suite.

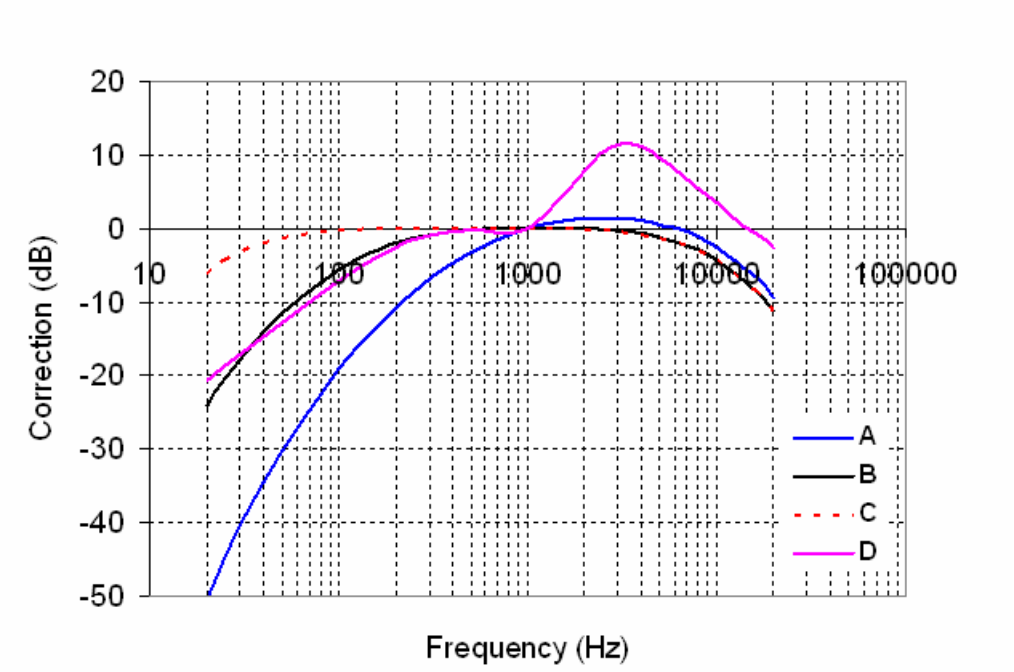

Figure 4.5: Standard weighting curves for sound level meters [3].

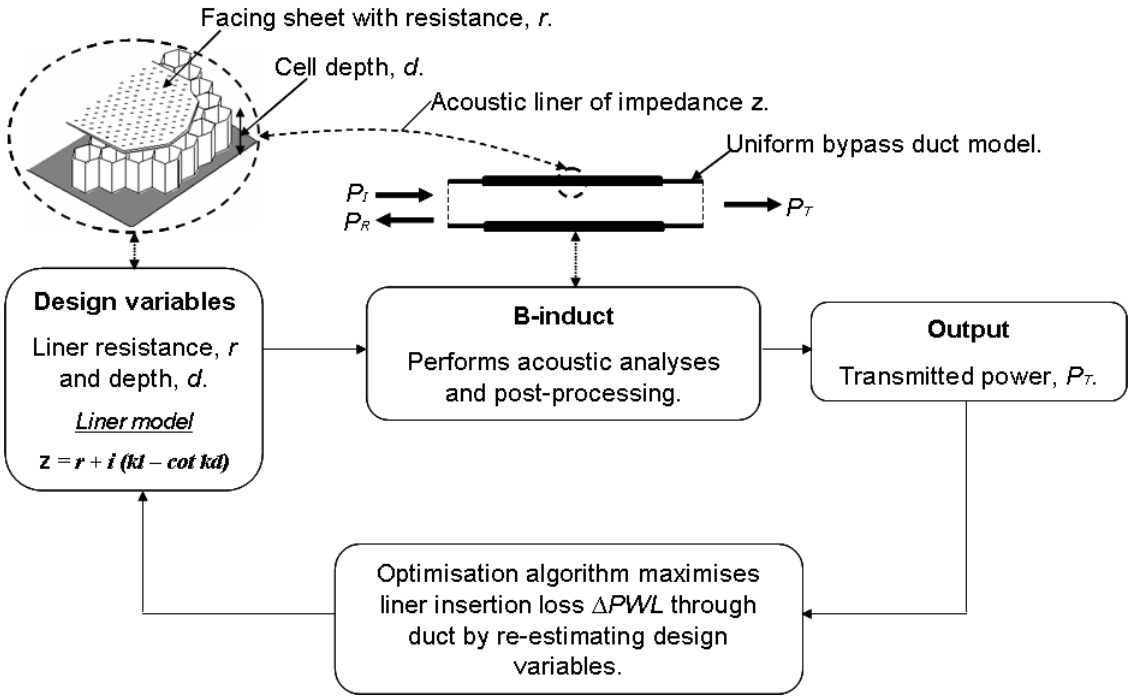

Figure 4.6: Liner impedance optimisation process, using B-induct within SOFT.

4.6 Optimisation strategy: SOFT

Within the optimisation set-up in SOFT, in addition to the choice of optimisation algorithm(s), the design range (bound constraints) for the design variables also needs to be specified. The non-dimensional resistance r, is allowed to vary between 0 and 5 typical of current liner designs for aeroengines, and the liner depth is allowed to vary between 0 and π/k when considering a source at a single frequency, where k is the wave number. The single cavity liner model used in this study, gives a non-dimensional reactance, $\chi' = kl - \cot(kd)$ which repeats for $kd > \pi$ due to the presence of the $cot(kd)$ term. The smallest liner depth is usually the most desirable, and the depth range is therefore contrained to exclude higher values. In the cases where the liner insertion loss ΔPWL is calculated over a range of frequencies, the upper bound of the liner depth is set to 50 mm (≈ 2 $inches$) which is a reasonable upper bound for current liner installations.

Considering dimensional quantities, the design range for each of the design variables is of different orders of magnitude (resistance R in kg/m^2s, $O(10^3)$ and the liner depth d in mm, $O(10^1)$). In order to improve the homogeneity of the search in all dimensions of the design space within SOFT, the design variables are normalised so that they vary between 0 and 1.

To explore and exploit the design space, a hybrid search is used. The hybrid search consists of a global ARMOGA [90] search followed by a local DHC [72] search. The global search ensures that the design space is explored so as to avoid local optima, and the local search refines the global optimum to obtain a more accurate solution. Details of the ARMOGA and DHC methods were described earlier, in Chapter 3.

In the ARMOGA search which is used in this chapter, for the single frequency cases, 50 evaluations (initial population of 25 transformed once) are used per design variable. For the multiple frequency cases which are more expensive, 20 evaluations (initial population of 10 transformed once) per design variable are used. In the DHC searches, for each normalised design variables within SOFT the initial step size is 0.1 and the minimum step size is 0.0001.

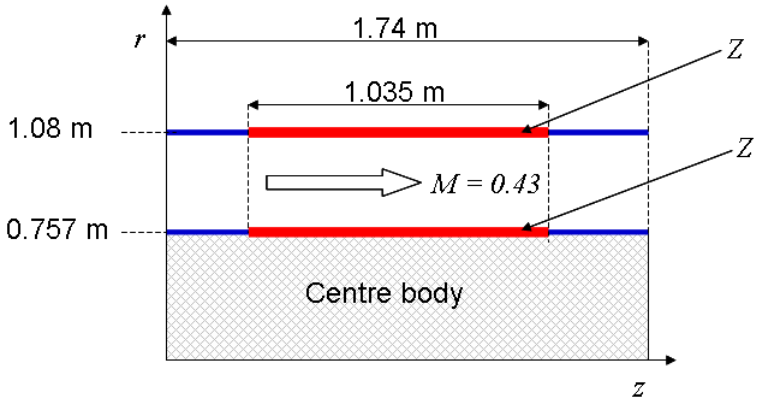

Figure 4.7: Uniform annular duct with single impedance Z.

Table 4.1: Optimised resistances and liner depths for single frequencies (500 Hz, 1 kHz, 2 kHz).

Frequency (Hz)	500	1000	2000
r $(R/\rho c)$	0.237	0.523	1.03
d (mm)	161.5	58.6	18.7
ΔPWL (dB)	57.86	36.06	15.53
CPU time	7m 55s	15m 26s	1h 5m 59s
Number of evaluations	157	156	138

4.7 Results

4.7.1 Single impedance, single frequency optimisation

The results obtained from optimising a uniform liner for an annular duct with dimensions shown in Figure 4.7 in the presence of a uniform mean flow (Mach number, $M = 0.43$) at frequencies of 500 Hz, 1000 Hz and 2000 Hz are shown in Table 4.1 and Figure 4.8. The contours shown in Figure 4.8 are obtained by evaluating the liner insertion loss from B-induct on a regular grid spanning the design space. The (red) dots are the ARMOGA points and the (blue) lines and crosses track the progress of the DHC search. For all three frequencies the SOFT optimisation correctly locates the maximum value of the liner insertion loss, as indicated by the location of the DHC target on the contours described earlier. As expected, the optimum depth of the liner decreases with frequency and is

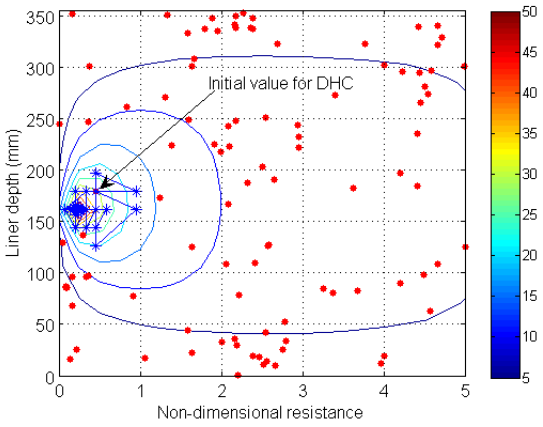

(a) 500 Hz

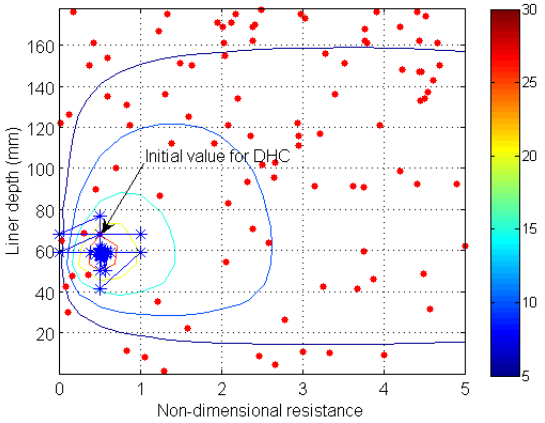

(b) 1000 Hz

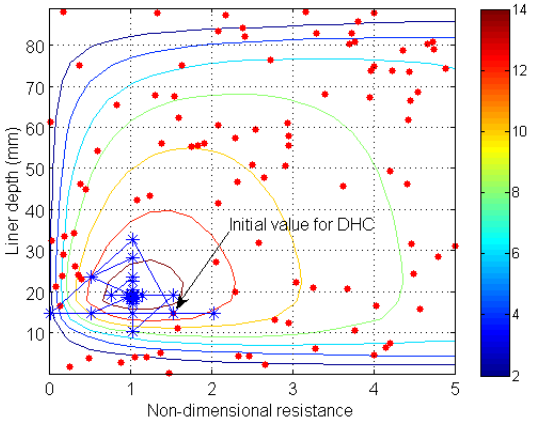

(c) 2000 Hz

Figure 4.8: Superposition of hybrid search on a two-dimensional contour plot of ΔPWL calculated for a single frequency, as a function of resistance and liner depth. (Red) dots: ARMOGA search, (blue) lines and crosses: DHC search.

somewhat smaller than the 'one-quarter' wavelength of the acoustic wave due to the effect of the mass inertance of the liner.

4.7.2 Double impedance, single frequency optimisation

4.7.2.1 Different liner impedances on inner and outer walls

The results obtained from the simultaneous optimisation of single liner segments Z_1 and Z_2, on the outer and inner walls (see Figure 4.9) are presented in Table 4.2. The liners are optimised for frequencies of 500 Hz, 1000 Hz and 2000 Hz. Four liner parameters are now present in the optimisation (real and imaginary parts of Z_1 and Z_2). The result cannot be checked against simple two-dimensional contours. However, the result obtained by SOFT is partially validated by noting that for all three frequencies the optimum values of liner insertion loss are somewhat larger than for the single liner case, as must be the case given that the latter is a subset of the former (cf. Table 4.1).

In an alternative optimisation approach, one liner impedance Z_1 is fixed at the single liner optimum (in Table 4.1) and the other liner impedance Z_2 is optimised. The new Z_2 optimum is then fixed and the impedance Z_1 is re-optimised. This iteration is done once and the results are compared to results obtained by optimising two liner impedances simultaneously. The assumption in this method is that if several iterations are performed, the result will coincide with the result from optimising two liner impedances simultaneously. In which case after one iteration as presented here, the result should move closer to the result from the simultaneous liner optimisation. Results from the two stage iterative liner optimisation process presented in Tables 4.3 and 4.4 confirm this assertion. It is also noticeable that the two liner optimisation does not produce in any case a radically different combination of impedances compared to the single liner case.

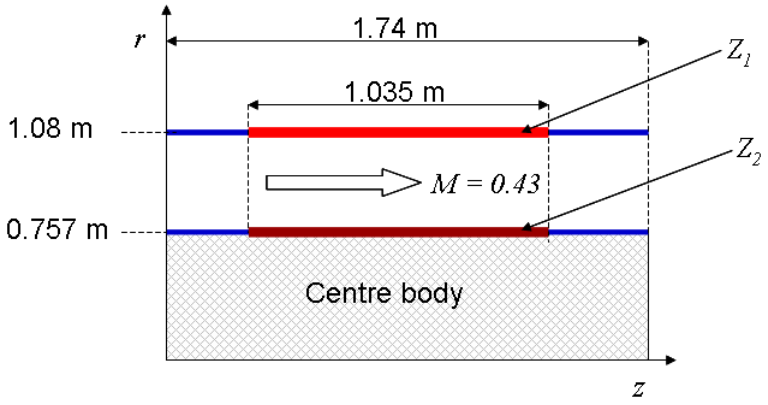

Figure 4.9: Uniform annular duct with two impedances Z_1 and Z_2.

Table 4.2: Optimised resistances and liner depths for each frequency (different inner and outer wall impedances).

Frequency (Hz)	500	1000	2000
r_1 ($R_1/\rho c$)	0.215	0.564	1.22
d_1 (mm)	163.6	59.8	21.4
r_2 ($R_2/\rho c$)	0.400	0.479	0.709
d_2 (mm)	168.0	57.9	17.0
ΔPWL (dB)	62.99	36.50	16.33
CPU time	22m 33s	29m 33s	2h 12m 31s
Number of evaluations	446	297	277

Table 4.3: Z_1 fixed at single impedance optimum and Z_2 optimised (different inner and outer wall impedances).

Frequency (Hz)	500	1000	2000
Fixed r_1	0.237	0.523	1.03
Fixed d_1(mm)	161.5	58.6	18.7
r_2	0.400	0.510	0.722
d_2 (mm)	168.9	58.3	17.3
ΔPWL (dB)	61.17	36.13	15.94
CPU time	9m 14s	15m 59s	1h 15m 34s
Number of evaluations	184	160	156

Table 4.4: Z_2 fixed at optimum from Table 4.3 and Z_1 optimised (different inner and outer wall impedances).

Frequency (Hz)	500	1000	2000
r_1	0.223	0.544	1.29
d_1(mm)	163.2	59.3	21.6
Fixed r_2	0.400	0.510	0.722
Fixed d_2 (mm)	168.9	58.3	17.3
ΔPWL (dB)	62.49	36.32	16.33
CPU time	8m 55s	15m 2s	1h 4m 49s
Number of evaluations	178	151	134

4.7.2.2 Two axial liner impedance segments

In this section results are obtained from an optimisation of a two segment liner with impedances Z_1 and Z_2 (see Figure 4.10). As in section 4.7.2.1 the results are presented for two methods used to perform the optimisation. In the first method two liner segments are optimised simultaneously, and in the second method one impedance segment is optimised while the impedance of the other segment is fixed.

The results for the simultaneous liner segment optimisation are presented in Table 4.5 and the results for the sequential liner segment optimisation are presented in Tables 4.6 and 4.7. The results presented in Table 4.5 can be partially validated using the results in Table 4.1 for a single impedance. The solutions from the single impedance optimisation (cf. Table 4.1) are subsets of the solutions from the two liner segment optimisation. A slight discrepancy occurs at 2 kHz where the optimum liner insertion loss for the single impedance case is 0.01 dB better than that of the two liner segment. However, this can be ignored as the liner insertion loss for both cases is effectively the same.

The results presented in Tables 4.6 and 4.7 confirm that in an iterative liner optimisation process, the results converge to the results at 1 kHz and 2 kHz obtained from optimising two liner segments simultaneously. However, this is not the case at 500 Hz where the benefits of scattering due to there being few cut-on modes present can be

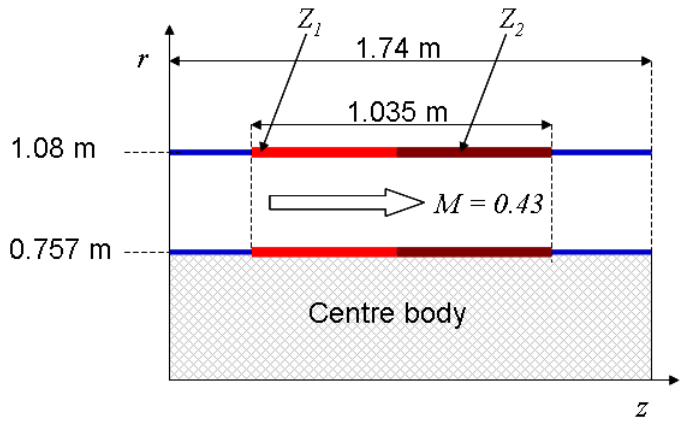

Figure 4.10: Uniform duct with two liner impedance segments Z_1 and Z_2.

exploited by a simultaneous liner segment optimisation (cf. Table 4.5). In general, optimising the liner segments simultaneously is a more efficient approach since the single impedance optimum is not required beforehand.

Table 4.5: Optimised resistances and liner depths for each frequency (two liner impedance segments).

Frequency (Hz)	500	1000	2000
r_1 $(R_1/\rho c)$	0.247	0.578	1.05
d_1 (mm)	173.6	56.1	18.4
r_2 $(R_2/\rho c)$	0.313	0.455	1.10
d_2 (mm)	159.9	60.2	19.4
ΔPWL (dB)	70.66	36.23	15.52
CPU time	30m 3s	28m 38s	2h 19m 53s
Number of evaluations	471	287	266

Table 4.6: Z_1 fixed at single impedance optimum and Z_2 optimised (two liner impedance segments).

Frequency (Hz)	500	1000	2000
Fixed r_1	0.237	0.523	1.03
Fixed d_1(mm)	161.5	58.6	18.7
r_2	0.239	0.522	0.966
d_2 (mm)	161.2	58.6	18.3
ΔPWL (dB)	57.88	36.06	15.51
CPU time	9m 56s	17m 9s	1h 9m 21s
Number of evaluations	158	174	132

Table 4.7: Z_2 fixed at optimum from Table 4.6 and Z_1 optimised (two liner impedance segments).

Frequency (Hz)	500	1000	2000
r_1	0.236	0.522	1.06
d_1(mm)	161.7	58.6	19.0
Fixed r_2	0.239	0.522	0.966
Fixed d_2 (mm)	161.2	58.6	18.3
ΔPWL (dB)	57.90	36.06	15.52
CPU time	8m 4s	17m 9s	1h 15m 27s
Number of evaluations	158	174	144

4.7.3 Single impedance, multiple frequency optimisation

4.7.3.1 Uniform power distribution ($f_{1/3}$: 500 Hz - 3.15 kHz)

In this section, results (see Table 4.8 and Figure 4.11) are presented for a single impedance optimisation to maximise the liner insertion loss ΔPWL, calculated for a uniform distribution of acoustic power at one-third octave centre frequencies $f_{1/3}$ from 500 Hz to 3.15 kHz. In this case contours of ΔPWL are plotted by evaluating ΔPWL on a regular grid over the entire design space. Expression (4.46) is used to calculate the liner insertion loss using the total transmitted intensities obtained in expression (4.51) for unit total intensity at each frequency. Figure 4.11 shows that an ARMOGA search followed by a DHC search clearly captures the global optimum indicated by the contours.

Considering that when multiple frequencies are considered, each evaluation point corresponds to computations performed at a number of frequencies (nine in this case), to compare the CPU times for such cases to those for the single frequency cases, the number of evaluations can be multiplied by the number of frequencies as shown in Table 4.8.

Table 4.8: Optimised resistance and liner depth ($f_{1/3}$: 500 Hz - 3.15 kHz, uniform power distribution).

Frequency (Hz)	$f_{1/3}$: 500 Hz - 3.15 kHz
r ($R/\rho c$)	1.50
d (mm)	43.1
ΔPWL (dB)	9.17
CPU time	37h 29m 59s
Number of evaluations	80 × 9

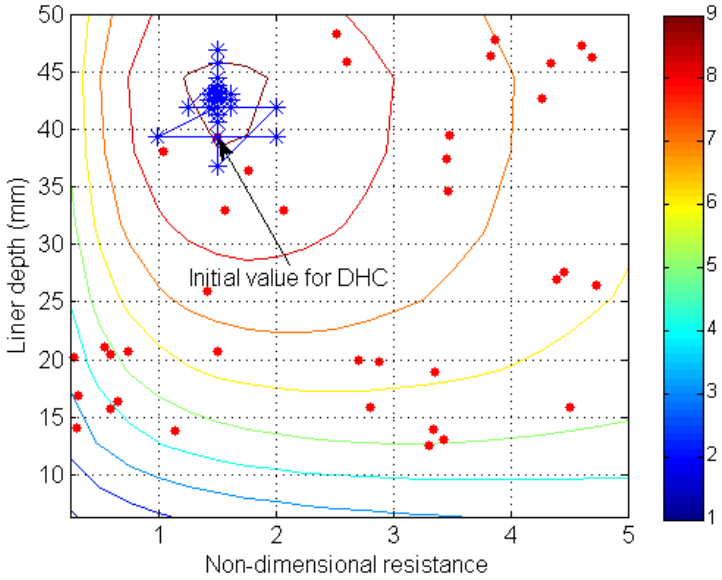

Figure 4.11: Superposition of hybrid search on a two-dimensional contour plot of ΔPWL calculated for a uniform power distribution, as a function of resistance and liner depth. (Red) dots: ARMOGA search, (blue) lines and crosses: DHC search.

4.7.3.2 A-weighted cost function for a uniform power distribution ($f_{1/3}$: 500 Hz - 3.15 kHz)

Results are also presented for an A-weighted insertion loss (ΔPWL_{Awt}) cost function for a uniform distribution of acoustic power at one-third octave centre frequencies $f_{1/3}$ from 500 Hz to 3.15 kHz, in Table 4.9 and Figure 4.12. In this case the liner insertion loss is calculated by using A-weighted transmitted intensities for hard-walled and lined ducts (expression (4.52)) in expression (4.46) to obtain an A-weighted insertion loss cost function (ΔPWL_{Awt}). The results again show that an ARMOGA search followed by a DHC search accurately locates the global optimum.

Table 4.9: Optimised resistance and liner depth ($f_{1/3}$: 500 Hz - 3.15 kHz, A-weighted ΔPWL for a uniform power distribution).

Frequency (Hz)	$f_{1/3}$: 500 Hz - 3.15 kHz
r $(R/\rho c)$	1.50
d (mm)	39.3
ΔPWL_{Awt} (dB)	9.82
CPU time	29h 32m 17s
Number of evaluations	63 × 9

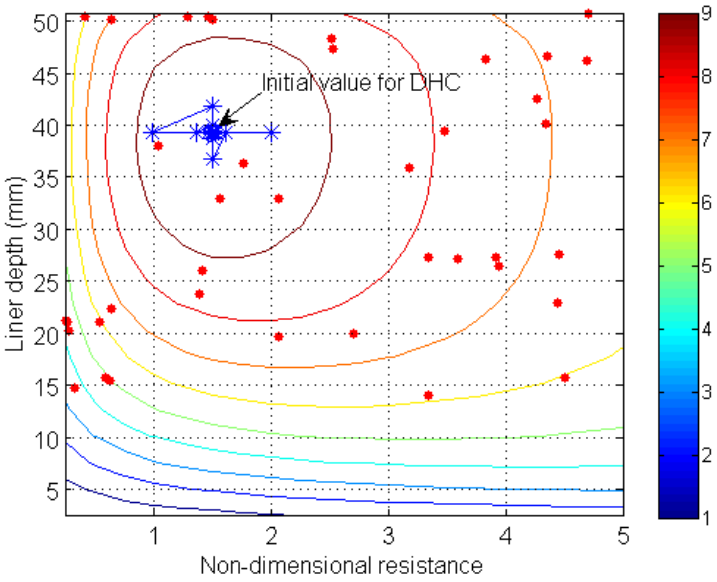

Figure 4.12: Superposition of hybrid search on a two-dimensional contour plot of ΔPWL_{Awt} for a uniform power distribution, as a function of resistance and liner depth. (Red) dots: ARMOGA search, blue lines and crosses: DHC search.

4.7.3.3 A-weighted cost function for a uniform power distribution ($f_{1/3}$: 500 Hz - 10 kHz)

In this section the liner insertion loss is evaluated using the same expression used in section 4.7.3.2, this time using a one-third octave centre frequency range from 500 Hz to 10 kHz. Above 3.15 kHz, a high frequency approximation is used to reduce computational effort. The results are presented in Table 4.10 and Figure 4.13. Figure 4.13 shows the robustness of an ARMOGA search followed by a DHC search when dealing with a design space which has multiple peaks.

From the results presented in Tables 4.9 and 4.10, it can be observed that, although higher frequencies (one-third octave centre frequencies from 4 kHz to 10 kHz) are included in the calculation of the A-weighted liner insertion loss ΔPWL_{Awt}, in Table 4.10, the optimum liner depth increases from 39.3 mm (cf. Table 4.9) to 48.1 mm. This may seem like an anomaly since, for a single frequency optimisation when the frequency is increased the optimum liner depth tends to decrease (since $d_{opt} \approx \lambda/4$, where d_{opt} is the optimum liner depth and λ is the wavelength). However, when higher frequencies are present, it seems that due to the $cot(kd)$ term in the single cavity liner model, although the previous optimum moves to a lower value of d, a new global optimum which lay beyond the original (0 - 50 mm) range has moved within the design space.

Table 4.10: Optimised resistance and liner depth ($f_{1/3}$: 500 Hz - 10 kHz, A-weighted ΔPWL_{Awt} for a uniform power distribution).

Frequency (Hz)	$f_{1/3}$: 500 Hz - 10 kHz
r $(R/\rho c)$	1.89
d (mm)	48.1
ΔPWL_{Awt} (dB)	8.57
CPU time	136h 37m 18s
Number of evaluations	80 × 14

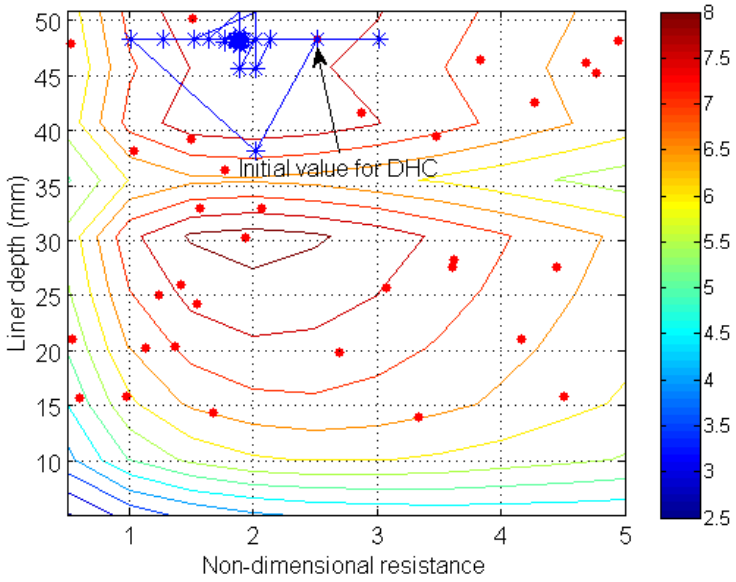

Figure 4.13: Hybrid search on multimodal design space of ΔPWL_{Awt}, as a function of resistance and liner depth. Red dots: ARMOGA search, blue crosses: DHC search.

4.8 Conclusion

In this chapter, a liner prediction scheme based on a finite element propagation code has been integrated within the Rolls-Royce optimisation suite SOFT and used to design optimum liners to maximise the liner insertion loss ΔPWL, calculated at single and multiple frequencies. An idealised (uniform) bypass was considered and the results have been fully and partially validated for one and two liner segments respectively.

From the results presented for the two impedance segment optimisation (Table 4.5), it can be seen that the two-segment liner is more effective only at 500 Hz when few propagating modes are present for a multimodal noise source. At higher frequencies (1 kHz and 2 kHz), as the number of propagating modes in the multimodal source model increases, there is little benefit from a multi-segment liner. When fewer propagating modes are present the effect of scattering is beneficial, but less so when many modes are present. The minimal benefit from multi-segment liners when many modes are present has also been highlighted by Lafronza [101]. Results presented in Table 4.2 suggest that, different

liner impedances on the inner and outer walls could be a more effective alternative to multi-segment liners for a multimodal source. These show benefits of 0.5 to 0.8 dB from 1 kHz to 2 kHz.

Figures for CPU times are also shown in the tables of results presented in this chapter. These figures are given for for computations on a single processor. They do not make use of more advanced solvers which are now available within ACTRAN/TM.
It is likely that the times presented here can be reduced significantly with little additional effort if repeated for example with the MUMPS[2] [102] solver which is now available in ACTRAN/TM. This would bring the CPU time for the final A-weighted optimisation to less than one day, which is well within acceptable limits for industrial applications in this type of approach. It is also worth noting that while the current computations have been performed on a uniform annular duct, no additional computational effort is involved in applying this procedure to realistic axisymmetric, bypass duct geometries. However, full validation of the results for realistic multi-segment liners will be more difficult since obvious benchmark cases no longer exist.

In the next chapter, a liner optimisation exercise is however performed for a realistic bypass duct geometry. The cost function is the A-weighted insertion loss for a uniform power distribution evaluated at one-third octave centre frequencies from 500 Hz to 10 kHz (see section 4.7.3.3).

[2]MUltifrontal Massively Parallel sparse direct Solver

Chapter 5

Case study: Liner optimisation for a realistic bypass duct geometry

5.1 Introduction

In the previous chapter, optimum liners have been designed to maximise the liner insertion loss ΔPWL and the A-weighted liner insertion loss ΔPWL_{Awt}, in a uniform bypass duct using a finite element code ACTRAN/TM within a shell program B-induct [4], integrated within a Rolls-Royce optimisation suite SOFT. The method was applied to a test problem in which the annular duct cross-section was uniform. In this chapter an optimum liner is designed to maximise the A-weighted liner insertion loss ΔPWL_{Awt} for a realistic bypass duct geometry, in which the cross-section varies along the axis of the duct.

The use of a realistic bypass duct geometry adds to the complexity of the sound field in the duct as modal scattering and reflections occur due to its curvature, even though the overall effect of these geometry changes on the transmission loss through the duct might be small [1, 103]. In order to use the liner optimisation method discussed in the previous chapter in practical applications, the method must be applicable to realistic geometries.

In the study presented in this chapter, the 'highly curved' bypass duct geometry investigated by McAleer [1] is used. A sketch of this geometry including an FE mesh

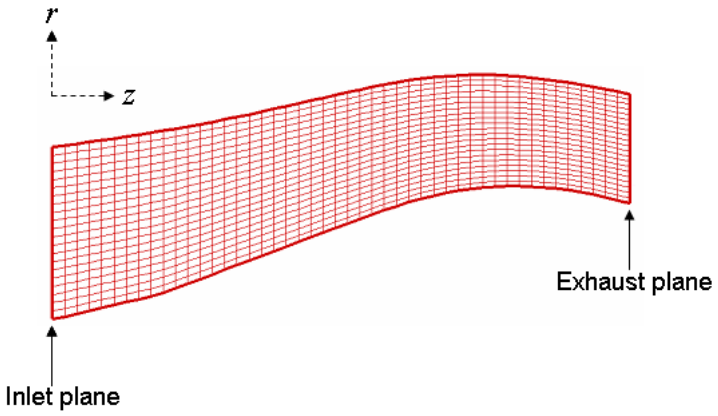

Figure 5.1: Highly curved bypass duct geometry showing FE mesh generated by B-induct [4].

in the in-duct domain is shown in Figure 5.1. The aim of this study is to compare results from the automatic liner optimisation method introduced in Chapter 4, to results obtained by McAleer using a different approach in which an EPNL cost function which takes into account other noise sources is used. Even though differences exist between the cost function in each case, it will be shown that the current automatic optimisation method predicts an optimal liner which is not dissimilar to that obtained by McAleer in reference [1].

5.2 The benchmark problem of McAleer [1]

The liner configuration for the highly curved bypass duct consists of two Inner Fixed Structure (IFS) liners on the inner wall and two Outer Fixed Structure (OFS) liners on the outer wall, as shown in Figure 5.2. In the study performed by McAleer, the cost function used for the bypass duct liner optimisation was the EPNL for the whole aircraft. The EPNL calculation is performed by an in-house Rolls-Royce 'whole engine' model which incorporates other noise sources, and requires the liner insertion loss to be evaluated at a wide range of frequencies.

McAleer [1] used ACTRAN/TM within the shell program B-induct to calculate the liner insertion loss ΔPWL for use in the 'whole engine' EPNL model. In the liner

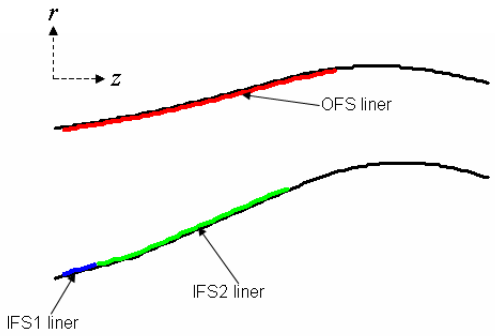

Figure 5.2: Sketch of bypass duct showing liner configuration used in reference [1].

optimisation process, for the three liners she optimised the impedance of each liner one at a time. This was achieved by generating a table of liner insertion loss values for different combinations of resistances R and reactances χ for one liner, while the impedances of the other liners were kept fixed. The liner insertion loss tables were generated for one-third octave frequencies from 50 Hz to 4000 Hz and used as reference tables to optimise the liner impedance using EPNL as the cost function.

The impedance model used for the optimisation was the model described in Figure 4.2, in which the impedance Z in terms of R and χ is obtained for a given cell depth d and porosity (percentage open area (POA)) of the facing sheet. The liner insertion loss for a given porosity and depth is then obtained by interpolation from the reference tables mentioned earlier.

The values at a grid of liner depths and $POAs$ are then used in the 'whole engine' model to obtain contour plots of EPNL against liner depth and porosity. Contours of the difference in EPNL (ΔEPNL) between the hard-walled and the lined duct configurations plotted against cell depth and porosity then indicate the optimum cell depth and porosity.

The first optimised liner impedance is then fixed by this process and it is repeated for the next liner with the third liner impedance still fixed at an initial value. The optimisation process is complete when all the liners have been optimised individually. This optimisation is performed separately at three certification conditions: approach, cutback and sideline. From the EPNL contours for each condition, the optimal overall

Table 5.1: Optimum liner impedances for 'highly curved' bypass duct geometry [1].

Liner	$POA(\%)$	Resistance, $r(R/\rho c)$	Liner depth, d (inches)
IFS1 liner	12	1.05	2
IFS2 liner	12	1.05	2
OFS liner	10	1.40	2

liner specification is chosen. In the results presented in reference [1] this corresponds to the optimum at the cutback condition. The values are shown in Table 5.1 together with the equivalent liner resistance. In the current study the cutback condition is chosen for comparison to McAleer's study [1].

5.3 A-weighted ΔPWL cost function.

In this section, the liners in the 'highly curved' bypass duct geometry shown in Figure 5.1 are optimised by using A-weighted liner insertion loss ΔPWL_{Awt} as a cost function. The liner insertion loss is calculated for an assumption of uniform acoustic power distribution over one-third octave bands with centre frequencies $f_{1/3}$, ranging from 500 Hz to 10 kHz, as described in the previous chapter.

McAleer optimised three liner impedances in turn, but predicted liner depths which showed little variation (see Table 5.1). The computational cost of optimising for six input variables (two design variables per liner) in the automated procedure used in this section would be high and for this reason, all three liners are now assumed to have the same impedance Z (see Figure 5.3). This reduces the size of the optimisation problem from one with six input variables to one with two input variables. The input variables in this study are therefore: a single facing sheet non-dimensional resistance r $(=R/\rho c)$, and a single liner depth d. The liner model used to relate the physical properties of the single cavity liner and acoustic impedance Z is given in Equation (4.1).

In the current study, the A-weighted liner insertion loss is used as a cost function. This is the same cost function as used in section 4.7.3.3 for a uniform bypass duct (in

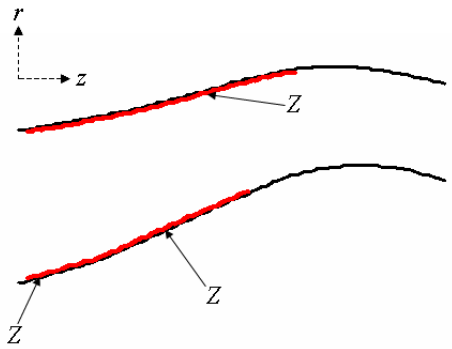

Figure 5.3: Sketch of bypass duct showing liner configuration with single impedance Z.

Chapter 4). The expression for the insertion loss is given by:

$$\Delta PWL_{Awt} = 10\log_{10}\frac{\sum_{j=1}^{n}\frac{I^j_{T(HW)}}{N_j}\cdot 10^{a_j/10}}{\sum_{j=1}^{n}\frac{I^j_{T(Lined)}}{N_j}\cdot 10^{a_j/10}}, \tag{5.1}$$

where n is the number of one-third octave centre frequencies, and for the jth one-third octave centre frequency, a_j is the A-weighting factor in dB, and N_j is the number of propagating modes at the exhaust plane of the duct. $I^j_{T(HW)}$ is the total transmitted intensity for the hard-walled bypass duct and $I^j_{T(Lined)}$ is the total transmitted intensity for the lined bypass duct.

5.3.1 Liner optimisation results

As in the uniform duct cases, an ARMOGA search is used first to explore the design space and locate potential global optima. A DHC search is then performed which refines the global optimum to obtain a more accurate location (details of these methods are discussed in Chapter 3 and are not included here). The cost function is given by expression (5.1), and the input variables are the non-dimensional resistance and liner depth varying between 0 to 5, and 0 to 2 inches respectively. In order to improve the homogeneity of the search in the two-dimensional (2D) design space, the bounds of the non-dimensional resistance r and the liner depth d are normalised so that they both vary between 0 and 1. The ARMOGA search used to obtain the results presented in this chapter, uses an initial

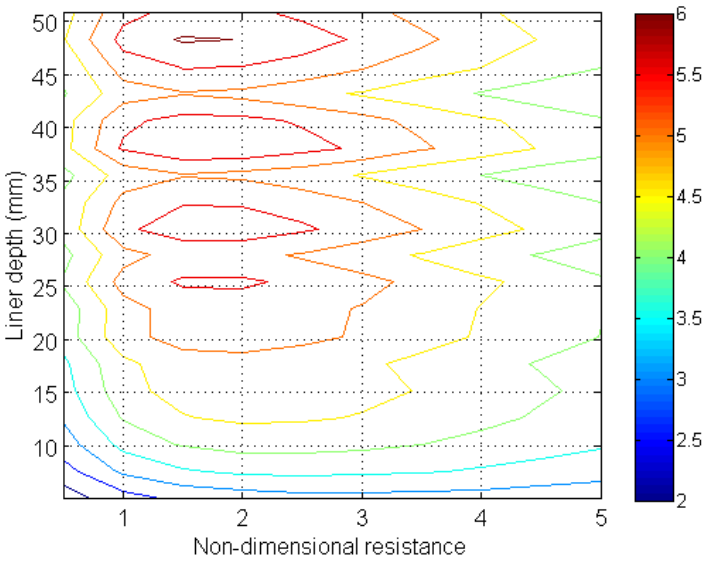

Figure 5.4: Contours of A-weighted liner insertion loss ΔPWL_{Awt}, as a function of non-dimensional resistance r and liner depth d.

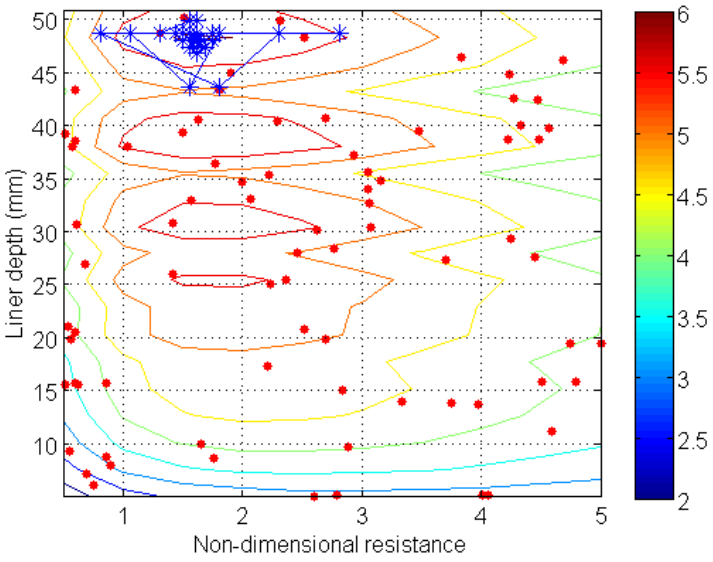

Figure 5.5: ARMOGA search (dots) followed by a DHC search (lines and crosses). Global optimum is found at a non-dimensional resistance $r = 1.62$ and liner depth $d = 48.1$ mm, corresponding to $\Delta PWL_{Awt} = 6.06$ dB.

Table 5.2: Optimum r and d, for maximum ΔPWL_{Awt} for a uniform power distribution.

Frequency (Hz)	$f_{1/3}$: 500 Hz - 10 kHz
r $(R/\rho c)$	1.62
d	48.1 mm $\approx$ 1.9 inches
ΔPWL_{Awt} (dB)	6.06
CPU time	47h 13m 47s
Number of evaluations	141

population size of 50 designs transformed once to give a total of 100 designs. In the DHC search, the initial step size is 0.1 and the minimum step size is 0.0001, in terms of the normalised variables.

In the case of this two-parameter optimisation problem, in order to check that the search locates the global optimum, contours of insertion loss, as a function of non-dimensional resistance r and liner depth d can be plotted. These contours are generated by sampling the design space at regularly spaced grid points in the r-d plane, and by calculating ΔPWL_{Awt} at these points. These contours are shown in Figure 5.4. This shows that the design space has multiple optima at different liner depths.

Figure 5.5 shows an ARMOGA search (dots) followed by a DHC search (lines and crosses), superposed on the contours of ΔPWL_{Awt}. This search finds a global optimum at $r = 1.62$ and $d = 48.1$ mm, corresponding to $\Delta PWL_{Awt} = 6.06$ dB. The optimisation was performed on a 3 GHz processor with 16 GB of RAM. A summary of the results, including the CPU time and the total number of evaluations is given in Table 5.2. From Figure 5.5, the ARMOGA and DHC searches correctly locate the global optimum as indicated by ΔPWL_{Awt} contours of Figure 5.4 which are also shown in Figure 5.5.

5.3.2 Discussion

The optimum non-dimensional resistance and liner depth obtained in this study are compared with the optimum values obtained by McAleer shown in Table 5.1. In the liner optimisation performed by using B-induct and SOFT, three liners are considered to have

the same impedance. The results shown in Table 5.2 can be compared with optimum impedances for the three liners (OFS, IFS1 and IFS2) shown in Table 5.1. The optimum resistance of 1.62 obtained in the current study compares reasonably well with an optimum resistance of 1.40 for the OFS liner in Table 5.1. In the case of the other two liners (IFS1 and IFS2), both with resistances of 1.05, there is a larger disparity with the current prediction. However, it is important to note that, for the IFS1 and IFS2 liners, the EPNL contours in reference [1] show that around the optimum, EPNL is not very sensitive to porosity, and a porosity of 10% corresponding to a resistance of 1.40 could equally be chosen as the optimum, as indicated in Figures 5.6(a) and 5.6(b) taken from reference [1].

In the case of the optimum liner depth, an optimum depth of 1.9 inches is obtained in the current study. This is in close agreement with an optimum depth of 2 inches chosen for all three liners (OFS, IFS1 and IFS2) in McAleer's study using EPNL as the cost function.

5.4 Conclusion

In this chapter, an automatic liner optimisation procedure has been applied to a realistic bypass duct geometry, using as cost function the A-weighted liner insertion loss ΔPWL_{Awt}. The results from this study have been compared with results from a liner impedance optimisation which was performed by using EPNL as the cost function [1]. Considering the differences in the number of liner impedances and the cost functions used in both cases, the results generally show a good agreement.

The similarity in the results in spite of the difference in the number of liner impedances in both cases, suggests that there is little noise benefit from having different impedance segments in the bypass duct, certainly when a multimode source is assumed.

The EPNL optimisation procedure performed by McAleer takes between 1-2 weeks. The current automatic ΔPWL_{Awt} optimisation takes about 2 days, and the calculation of the ΔPWL_{Awt} cost function is relatively cheap. The automatic ΔPWL_{Awt} optimisation procedure can therefore be used for preliminary liner design as a cheaper option to the

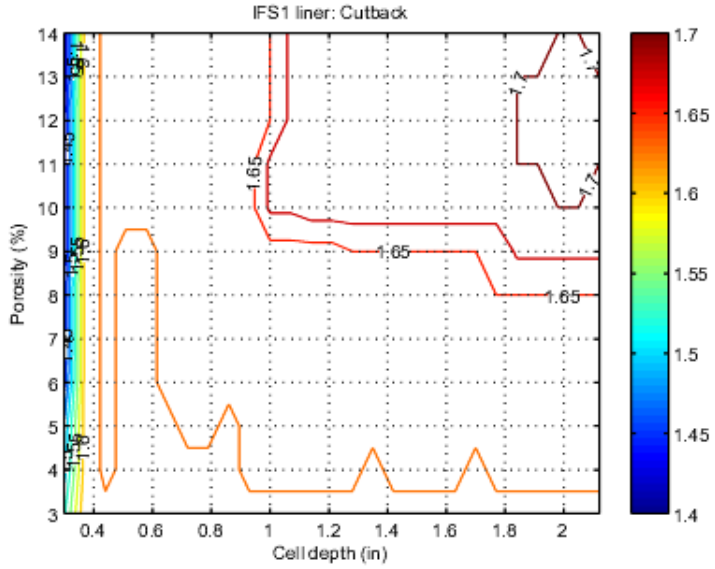

(a) IFS1 liner.

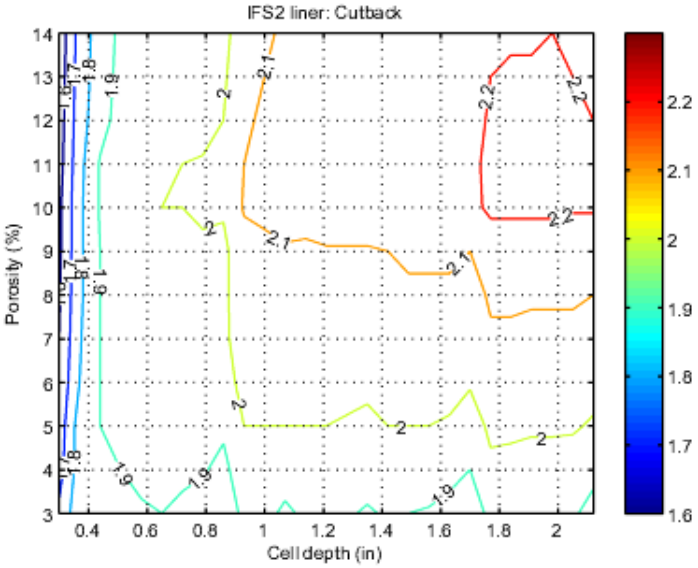

(b) IFS2 liner.

Figure 5.6: Contour plots of ΔEPNL for IFS1 and IFS2 liners at cutback condition [1].

more computationally expensive EPNL optimisation, and can be performed over a period which is acceptable for application in industry.

Chapter 6

Prediction of forward fan noise propagation and radiation from engine intakes

6.1 Introduction

The evolution of aeroengines from 1960s turbojets to modern turbofans has led to a large reduction in jet mixing noise. This has accentuated the presence of other noise sources such as fan noise. Fan noise is major noise source at the approach and take-off conditions in modern high bypass ratio turbofan engines. Fan noise is generally made up of tones (rotor-locked tones and/or buzz-saw tones) superposed on a broadband noise floor generated by turbulent unsteady flow over the fan and Outlet Guide Vanes (OGVs). It propagates into the forward arc through the intake and into the rear arc through the bypass duct. This chapter deals with the noise propagated and radiated into the forward arc as shown in Figure 6.1.

Considering that the optimisation procedure described in the previous chapters is only valid if the propagation model gives the correct result, the propagation model needs to be validated. This model can only be validated by comparison to measured data. Measured

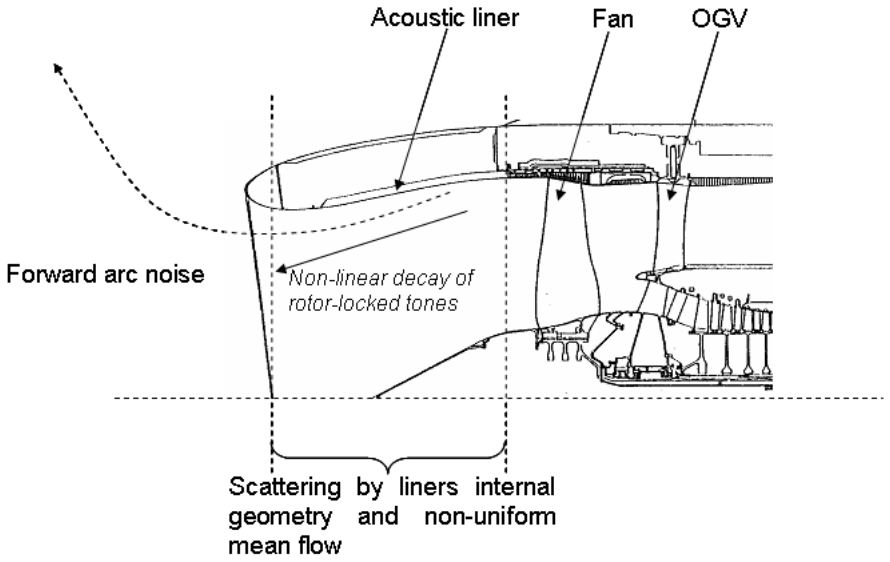

Figure 6.1: Propagation of fan noise through intake and radiation into the far field.

data from the intake is generally more suitable than exhaust data for validating the model because far field and in-duct data is available from rig tests which excludes other sources and which permits accurate representation of the fan source.

6.2 Fan noise sources

In this section the generation of the major components of fan noise is briefly explained. More comprehensive descriptions can be found in reference [5].

6.2.1 Rotor-locked tones

A rotor-locked tone is a pressure field generated by a rotating fan or rotor, and is stationary in the rotating frame of reference, hence the term 'rotor-locked'. Considering a fan with N identical blades, rotating with angular velocity Ω rad/sec ($= 2\pi f_s$ where f_s is the shaft rotation frequency in Hz), for equally spaced blades, the rotating pressure field repeats itself every $\Delta\theta_f = 2\pi/N$, where θ_f is the circumferential coordinate fixed in the rotating frame of reference (see Figure 6.2). The stationary pressure field in the rotating frame of

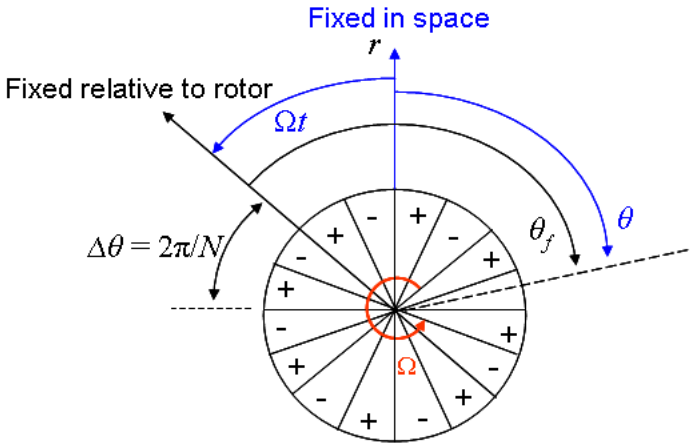

Figure 6.2: A rotating pressure field in fixed and rotating frames of reference produced by an 8-bladed fan with angular velocity Ω [5].

reference $p(r,\theta_f)$ where r is the radial coordinate, can then be expressed as a summation of circumferential harmonics given by:

$$p(r,\theta_f) = \sum_{n=-\infty}^{\infty} p_n(r) e^{inN\theta_f}. \tag{6.1}$$

By considering a frame of reference fixed in space and defined by circumferential angle θ, where $\theta_f = \Omega t + \theta$ where t is the time in seconds, expression (6.1) can be written as an unsteady pressure field such that:

$$p(r,\theta,t) = \sum_{n=-\infty}^{\infty} p_n(r) e^{inN(\Omega t+\theta)} = \sum_{n=-\infty}^{\infty} p_n(r) e^{i\omega_n t} e^{inN\theta}, \tag{6.2}$$

where the angular frequencies ω_n $(= nN\Omega)$ are integer multiples of $N\Omega$. These correspond to harmonics of the Blade Passing Frequency (BPF) measured in Hz where BPF is the product of the number of blades N and the shaft rotation frequency f_s. Expression (6.2) shows that, the rotor-locked pressure field is made up of a discrete spectrum of tones at harmonics of BPF (at f = BPF, 2×BPF, 3×BPF,...etc.).

6.2.2 Buzz-saw tones

When the rotating pressure field contains components which are not periodic with blade spacing in the circumferential direction, more tones can be generated at multiples of the

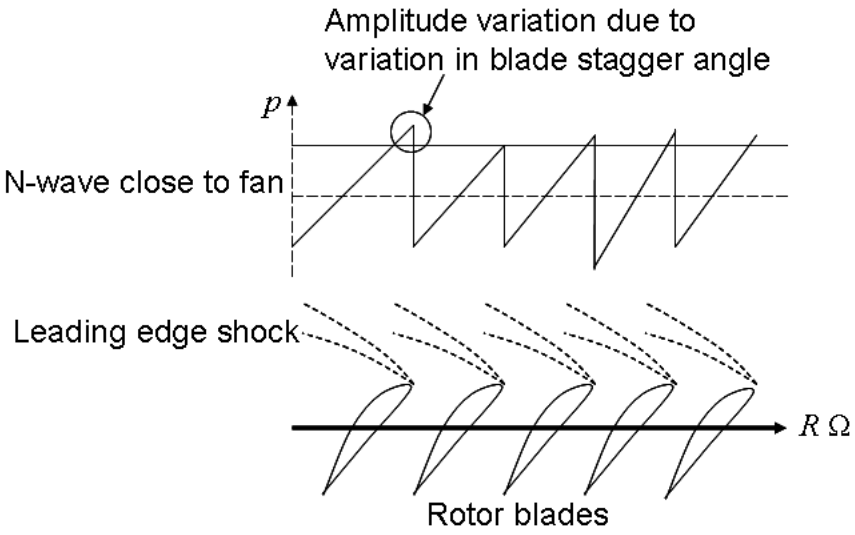

Figure 6.3: N-wave pressure (p) pattern (sawtooth) generated by a fan of radius R rotating with angular velocity Ω [5].

shaft rotation frequency f_s in addition to the multiples of BPF ($= Nf_s$). This occurs when the fan tip speed is supersonic and shock waves are formed upstream of the blade as shown in Figure 6.3 creating an 'N-wave' (sawtooth) pressure pattern. The variation in the initial amplitude of the N-waves close to the fan due to the variations in blade stagger angle is amplified by non-linear propagation close to the fan [104, 105]. Consequently, more irregular non-periodic N-waves are generated upstream of the fan. This produces an acoustic pressure pattern which is 'locked' to the rotating shaft rather than the blade spacing. It corresponds to 'Engine Order' (EO) tones at multiples of the shaft rotation frequency f_s(at $f = f_s$, $2\times f_s$, $3\times f_s$,...etc.), which are also called 'buzz-saw' tones or 'multiple pure' tones. Figure 6.4 shows forward arc noise spectra at approach and sideline conditions from a static engine test. The spectra show BPF tones at the approach condition with subsonic fan tip speeds and, BPF and buzz-saw tones at the sideline condition with supersonic fan tip speeds.

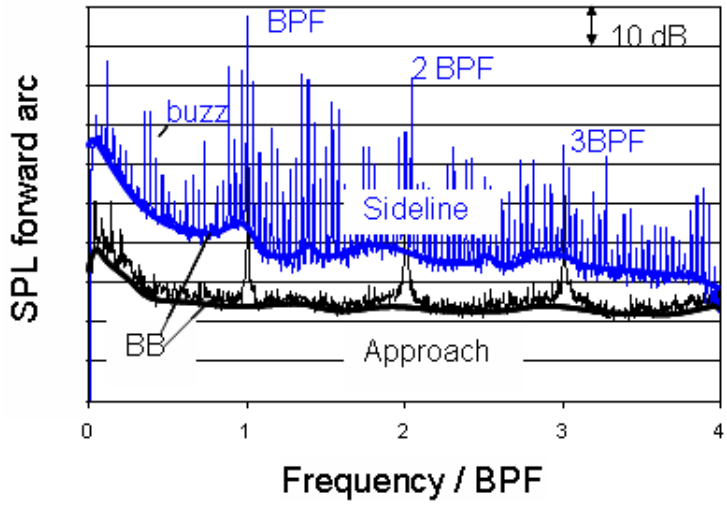

Figure 6.4: Forward arc engine noise spectra at the approach and sideline conditions (reproduced by permission of Rolls-Royce plc) [5].

6.2.3 Fan broadband noise

In Figure 6.4, it can be seen that for both approach and sideline conditions, tones protrude from the non-tonal component with a continuous spectrum. The non-tonal component is called BroadBand (BB) noise. Fan broadband noise is generated by different mechanisms as illustrated in Figure 6.5. These are, turbulence in the boundary layer on the rotor scattered from the trailing edge (1), impingement of turbulent rotor wakes on the stator (2), the interaction of the rotating fan with the turbulent boundary layer on the duct wall (3) and the interaction of the fan with the ingested turbulence (4). A detailed study by Ganz *et al.* [106] showed that the main sources of inlet radiated noise are the first three sources which are of comparable importance.

6.3 Fan noise propagation models

As fan noise propagates through the engine intake, it is scattered by the intake geometry, the liner impedance discontinuities and the non-uniform mean flow (see Figure 6.1). It is also attenuated by the acoustic liners while it propagates through the intake. The

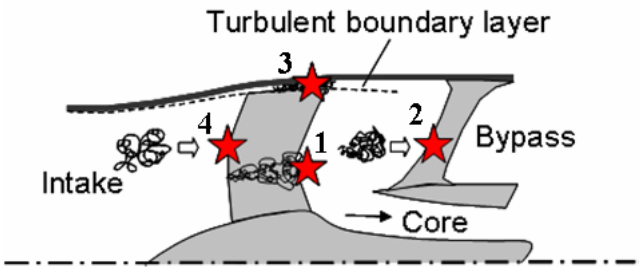

Figure 6.5: Sources of broadband fan noise highlighted by (red) stars [5].

noise then radiates from the intake to the external region towards the far field. A numerical simulation of this intake noise problem poses a significant computational challenge. Approaches that have been used for such problems include Boundary Element (BE) methods [67], Finite and Infinite Element (FE/IE) models [56] and Computational Aeroacoustics (CAA) methods [107].

BE and FE/IE models are commonly used for solving the convected Helmholtz equation in the frequency domain. CAA methods can be used to solve the Reynolds Averaged Navier-Stokes, the Linearised Navier-Stokes or the Linearised Euler equations. These latter methods can capture the physics of the problem better than the FE/IE methods since they can be applied to rotational mean flows. However this is not a major issue for the intake problem because the mean flow is largely irrotational. The great advantage of FE/IE methods for the convected Helmholtz equation is that they are less computationally demanding since they use only a single variable, the velocity potential, at a node point. In addition, the frequency dependence of the impedance of acoustic liners, makes them more easily represented in the frequency domain than in the time domain. They can run within acceptable timescales for realistic problems in industrial applications, especially in the case of axisymmetric problems. Another advantage of using the FE/IE method is that, the far field solution is obtained directly as part of the near field solution. One major limitation of FE/IE methods is the fact that they can only model linear disturbances and hence cannot deal with non-linear effects which can occur near the fan plane.

In this chapter, an FE/IE model is used to obtain a numerical solution of the con-

vected Helmholtz equation. A brief summary of this approach is given in the next section. Also, a concise description of the FE method has been given in section 4.2.

6.3.1 The finite and infinite element model

In this thesis, in order to predict the forward radiated fan noise, the FE/IE analysis code ACTRAN/TM [9] is used within a shell program ANPRORAD [60] used for performing near and far field acoustic analysis for sound propagation and radiation for axisymmetric intake ducts.

Figure 6.6 shows an aeroengine intake model with surface Γ in an unbounded region V and an FE/IE interface S. In this model, an acoustic field propagates on an irrotational mean flow in the unbounded region. The surface Γ is made up of the fan plane Γ_F, the lined surfaces Γ_L and the remaining hard-walled surfaces Γ_H including the nose cone (spinner), and the outer surfaces of the nacelle. In this model, considering that the focus is on modelling the forward radiated noise, the rear of the nacelle is represented by a non-realistic simplified geometry. The unbounded region V is divided into a near field region V_i which is modelled by finite elements (FE) and an external region V_o which extends to infinity modelled by a layer of infinite elements (IE). In contrast to finite elements in which the acoustic velocity potential is expressed in terms of polynomial shape functions, infinite elements are based on a multiple expansion of arbitrary order to model outgoing

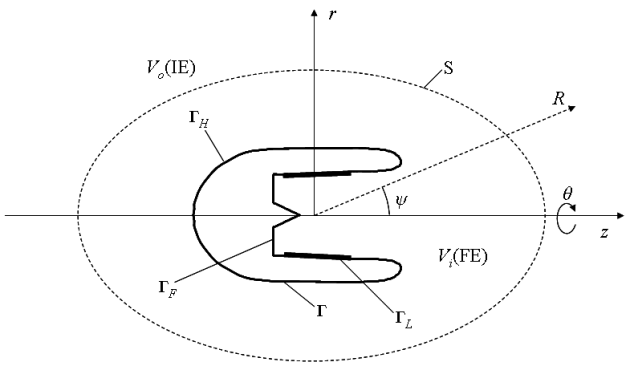

Figure 6.6: Aeroengine inlet geometry in unbounded region V shown in cylindrical (r, θ, z) and spherical (R, ψ, θ) coordinates.

waves. An increase in the order improves the accuracy and enables one to have the FE/IE interface closer to the object.

6.3.2 ANPRORAD intake shell program

ANPRORAD [60] is a shell program used to perform ACTRAN/TM analysis for axisymmetric intake problems. It comprises of a pre-processor that creates ACTRAN/TM input files, a command that executes ACTRAN/TM, and a post-processor that reads the ACTRAN/TM output files and produces files containing the main results in simple formats.

The information required to produce the ACTRAN/TM input file is provided within an input text file for ANPRORAD *inputdata.txt*. This input file contains key geometric data in coordinate form specified by using a number of flag points (ip) and intermediate points. These points are then connected by using a spline interpolation to create the axisymmetric intake geometry (see Figure 6.7). In Figure 6.7 the z-axis is the axis of axisymmetry for the engine intake geometry and the r-axis is the radial axis from the origin which is taken at the centre of the fan. The outer boundary of the FE domain is defined by an ellipsoid with a centre (zrc, 0) and axes a and b as shown in Figure 6.8. Given the intake surface and the FE boundary, the pre-processor generates an FE mesh with quadratic elements for the surrounding near field region (see Figure 6.9). A layer of infinite elements is attached externally to the FE domain.

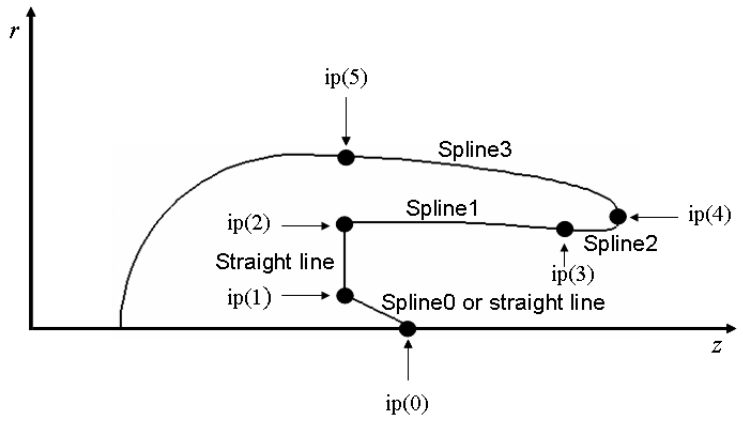

Figure 6.7: Sketch showing flag points (ip) and spline interpolation between points.

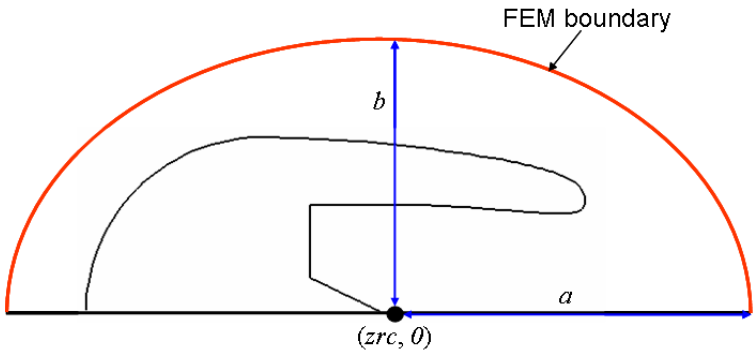

Figure 6.8: FEM boundary ellipsoid with centre (zrc, 0) and major and minor axes a and b respectively.

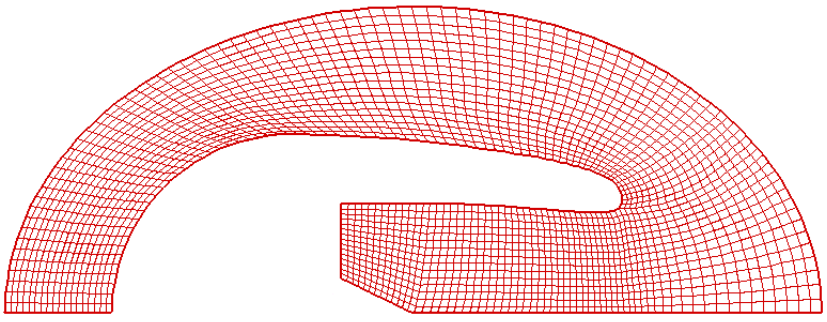

Figure 6.9: Intake FE mesh generated by ANPRORAD pre-processor.

The mesh resolution is controlled by the number of elements across the fan plane (in the r-direction) and by the number of nodes per wavelength (which is used to determine mainly the element size) in the z-direction. Typically, 10 nodes per wavelength are used in both directions in the results presented in this thesis. In addition, the IE order, corresponding to the order of the multiple expansion in the radial direction is specified. In the results presented in this thesis, an IE order of 15 is typically used.

In the input file, the mean flow parameters; fluid density, sound speed and Mach number or mass flow rate are also specified at the fan plane. The flow field can either be specified as a uniform flow with a constant Mach number or as a non-uniform flow with a mass flow variation with radial position on the fan plane. In this thesis, a uniform flow is always specified at the fan plane. To define the noise source, a modal boundary condition is imposed at the fan plane. The source at this boundary is defined in terms of hard-walled annular duct modes. In ACTRAN/TM axisymmetric analysis, the problem is solved for a single circumferential order at a time. An analysis for a circumferential order, can be solved for multiple incident modes of different radial orders simultaneously. The acoustic power of each incident mode is defined in terms of Morfey's formulation for acoustic intensity [97]. The reflected modes at this modal boundary are not known beforehand and are obtained from the analysis as part of the solution by imposing anechoic boundary conditions for noise propagating back into the fan.

Acoustic liners are defined by specifying their axial start and end positions as well as their acoustic impedances. This information is then used to apply the admittance boundary condition on the lined segment of the intake wall. Prior to running ACTRAN/TM for the acoustic analysis, ANPRORAD solves the compressible Euler equations by imposing a uniform flow at the fan plane, and a constant mean flow Mach number at the outer FE boundary (see Figure 6.10). The mean flow solver uses the same mesh created for the acoustic analysis, but ignoring mid-nodes and treating each element as a linear element. The resulting mean flow in the form of the axial and radial component of the fluid velocity is then interpolated onto each node of the acoustic elements.

In order to compare the predicted results to measured data, the positions of any far

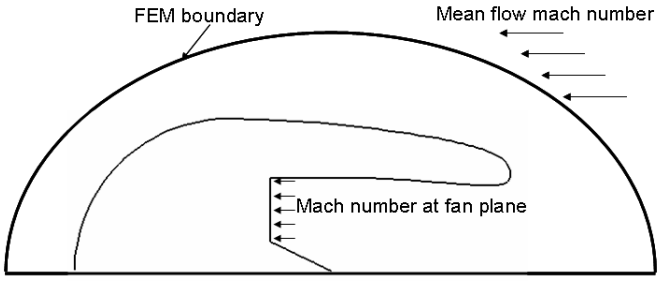

Figure 6.10: Fan plane Mach number and mean flow Mach number boundary conditions used to calculate the velocity flow field in the FE domain.

field microphones can also be included in the input file by specifying a set of field points at which predicted results can be obtained.

Once the input file *inputdata.txt* is created, ANPRORAD uses this file to create the input file for ACTRAN/TM *input.inp*, which contains details of the flow field and the FE mesh. Running ACTRAN/TM with *input.inp* produces an output file *actran_res.opt* which contains the predicted values at any additional field points that were specified in the ACTRAN/TM input file.

The post-processing step of ANPRORAD extracts values from ACTRAN/TM output files which can be readily used by the user to analyze the results. An outline of the processes of ANPRORAD is shown in Figure 6.11.

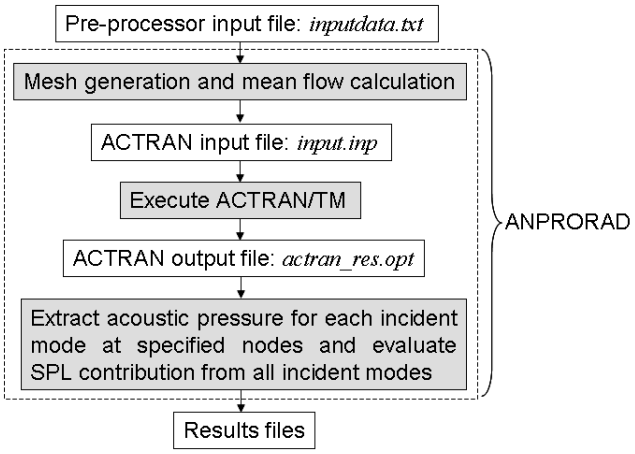

Figure 6.11: Outline of calculation procedure within ANPRORAD.

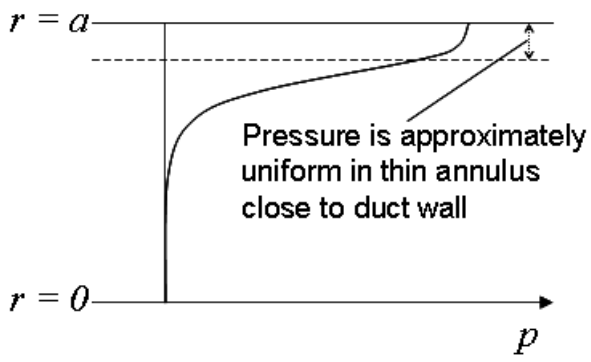

Figure 6.12: Variation of acoustic pressure p with radial coordinate r, showing first radial order in a rigid cylindrical duct.

6.3.3 Non-linear propagation model

As described in section 6.2.2, buzz-saw tones are produced at supersonic fan tip speeds. This pressure pattern attached to the fan with supersonic tip speed has a high amplitude sawtooth [104] waveform and therefore it propagates non-linearly inside the intake. Such non-linear propagation cannot be predicted by ACTRAN/TM which is based on a linear propagation model. In order to tackle this problem, 'Frequency Domain Numerical Solution' (FDNS) [105, 108] can be used to include non-linear effects. FDNS is used later on in this thesis to predict the liner attenuation of rotor-locked modes at supersonic fan tip speeds at BPF. The full details of this model can be found in references [105, 108]. Only a brief summary of the method is given below.

The basis of this model is that, the rotor-locked pressure is modelled approximately by a one-dimensional irregular sawtooth (see Figure 6.3) pressure waveform, in the circumferential direction θ. The rotor-locked pressure field attached to a supersonic fan can be expressed as a superposition of radial modes that are steady in the rotating frame of reference. Since most of the higher order radial modes are cut-off, considering only the first radial mode can give a good approximation to the acoustic pressure field. The energy in the first radial mode is concentrated near the wall due to the nature of the Bessel function at the wall (see Figure 6.12). Consequently, the acoustic pressure field

(in cylindrical coordinates) can be approximated in two-dimensions by (θ, z) where r is constant and can be approximated by the duct radius a.

The propagation of this one-dimensional irregular sawtooth pressure waveform is predicted using the non-linear Burgers equation. The effect of acoustic liners is approximated by including a linear absorption term as proposed by Fisher *et al.* [109].

6.4 Summary

In this chapter, the bases of the numerical analysis for fan noise propagation through a turbofan engine intake have been described. Firstly, the mechanism of generation of the source components of engine fan noise has been summarised. They are BPF tones and buzz-saw tones, and broadband noise. These tone and broadband components can be dealt with separately in prediction models by assuming that they are uncorrelated. In this light, predictions can be performed individually for each component after which they can be combined to give an overall fan noise prediction.

Secondly, a brief explanation has been given about ANPRORAD-ACTRAN/TM, FE/IE model for intake noise prediction. ANPRORAD is a shell program for ACTRAN/TM specialised for turbofan engine intake noise problems. In the intake where boundary layers on the inner surface of the nacelle are thin and the mean flow is largely irrotational, linearised Euler equations based on the acoustic velocity potential, or the convected Helmholtz equation can be applied. In ACTRAN/TM, the problem is described in terms of the convected Helmholtz equation in the velocity potential and solved numerically in the frequency domain using FE/IE methods. These are less computationally demanding than CAA methods and can be used to solve a realistic intake application within acceptable time frames. This is more so for problems where the liner configuration and geometry can be treated as axisymmetric, as in the cases considered in this thesis. This has led to FE/IE methods being more attractive for industrial applications.

The FE/IE model in ACTRAN/TM is a linear one and cannot deal with non-linear effects that occur close to the fan at supersonic fan tip speeds. In order to take into

account such effects, an approach used within FDNS [108] can be used. In this model, the propagation of the rotor-locked pressure field is obtained by solving the non-linear Burgers equation. The effect of acoustic liners is included in the model through the addition of a linear absorption to the non-linear Burgers equation. In this chapter this FDNS model has been briefly described. It is used in Chapter 7 to obtain the liner attenuation of rotor-locked modes including non-linear effects.

Chapter 7

Validating ANPRORAD intake predictions against measured data

7.1 Introduction

In the previous chapter a finite and infinite element (FE/IE) approach (within ANPRORAD) was described for predicting forward radiated fan noise. In order to confidently use this prediction tool in future engine intake designs for low noise, the model has been validated against measured data. This study is presented in the current chapter.

Results on the predicted far field Sound Pressure Level (SPL) field shapes and liner attenuations will be presented for rig and engine intakes at three certification conditions. These are defined by shaft speeds as a percentage of the maximum engine shaft speed (%NL) at approach (50 %NL), cut-back (80 %NL) and sideline (90 %NL). Numerical results are presented in which fan sources are represented as a summation of tones and multiple uncorrelated modes. By inferring the relative strengths of the single mode and multimodal source components from hard-walled in-duct test data, the far field SPL field shapes for hard-walled and lined configurations can be predicted. Corrections to include non-linear acoustic behaviour close to the fan have also been applied. These lead to significant improvements in the agreement between predicted and measured data at the

sideline condition. In the case of tone predictions, the source is multimodal at subsonic tip speeds, and is composed of a multimodal content superposed on a high amplitude rotor-locked mode at supersonic tip speeds. In the case of broadband noise, hard-walled test data have been examined to gain some understanding of its generation and modelling.

The studies presented in this chapter provide an assessment of the robustness of the FE/IE method for realistic intake designs by comparing predicted data to measured data from rig and engine tests. Rig data are not contaminated by other sources such as core and jet noise, present in engine test data. They contain fewer uncertainties and are therefore more useful for a validation study. In this case, an axisymmetric intake was used in the rig test. This facilitated direct comparison with the predicted data obtained from an axisymmetric analysis without approximation.

7.2 Comparison between predicted and rig data

7.2.1 Experimental set-up

Noise measured data from a 1/3-scale model fan rig were taken in the anechoic test cell in the AneCom test facility. The fan rig has a 24-bladed fan with a diameter of 0.86 m. Figure 7.1 shows the general set up of the cylindrical barrel intake. A transition casing

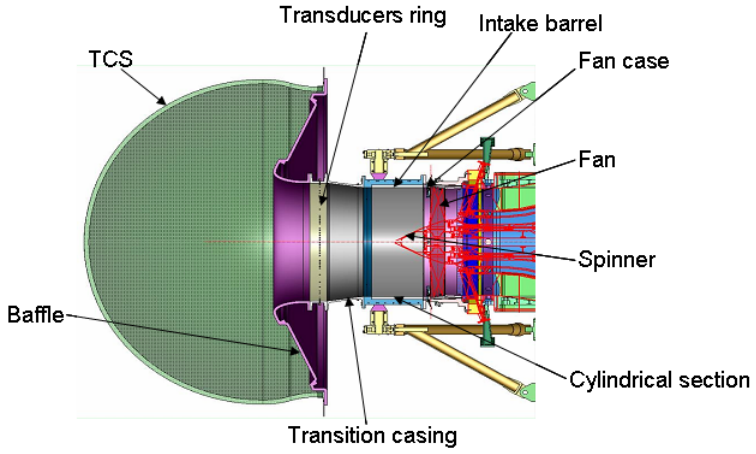

Figure 7.1: Design of fan inlet system by ASSYSTEM in SILENCE(R) programme.

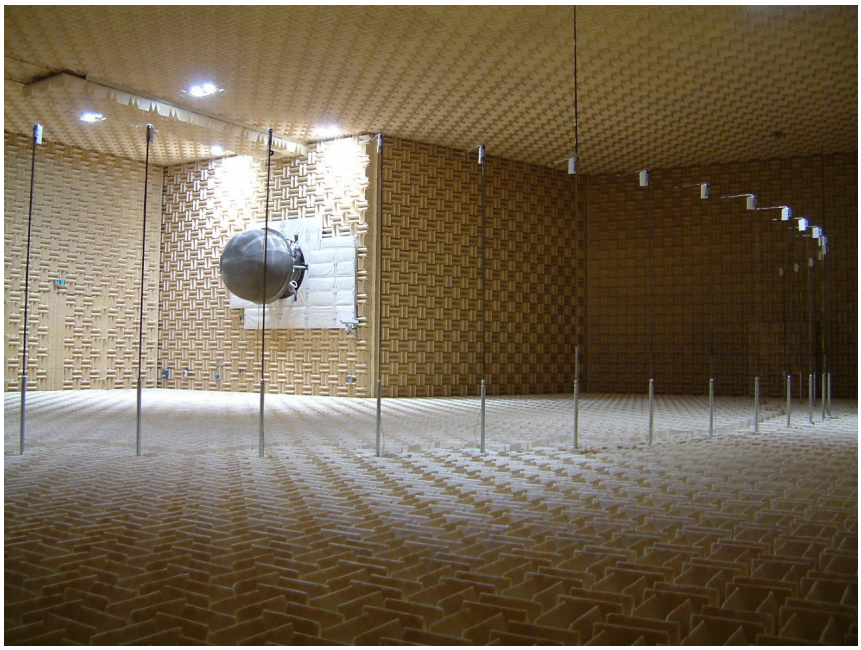

Figure 7.2: Rig including turbulence control screen (TCS) installed in the AneCom Test Facility.

is located between the cylindrical section and the baffle assembly where the pressure transducer ring is located. The location of the pressure transducers is shown in Figure 7.1. Two intake configurations are considered in this study: the first consists of a hard-walled intake barrel and hard-walled fan case, and the second a lined intake barrel and a lined fan case. Figure 7.2 shows the rig installed in the AneCom Anechoic Test facility with the turbulence control screen (TCS) in place. An array of far field microphones is also shown. These are on a circular arc at the rig centreline height, between 0 and 120 degrees relative to the intake axis, with a 5 degrees spacing.

7.2.2 Mode detection

A single-pulse-per-revolution tachometer is used to sample data obtained from the pressure transducers mounted in the mode detection ring. These readings are converted to wall sound pressure levels of the circumferential duct modes using the method described by Rademaker *et al.* [110].

At each microphone channel k, a time pressure signal $s^k(t)$, is measured in a time

interval between two pulses, t_j and t_{j+1} where j is the pulse index. Taking the Fourier transform of this signal gives a complex pressure spectrum ${p^k}_{j,n}$, for $n = 1, ...N$, where n is the Engine Order (EO). The complex pressure amplitudes are given by:

$$a^m_{j,n} = \frac{1}{K} \sum_{k=1}^{K} p^k_{j,n} e^{im\theta_k}, \tag{7.1}$$

where m is the circumferential mode number, K is the number of microphones and θ_k is their angular position. In order to avoid aliasing, the number of microphones has to be at least two times the maximum circumferential mode number. However, at high frequencies this poses a problem since a large number of microphones is required. In this study an optimised array [110] of 100 microphones is used. Therefore, the measurements made in the circumferential mode range of $-79 \leq m \leq 79$, cannot be completely free of aliasing. However, reliable data (not contaminated by aliasing) can be obtained in the given circumferential mode range provided that a dynamic range of 18.2 dB is present, i.e. the difference between the maximum and minimum measured levels decomposed into circumferential mode numbers m is within 18.2 dB.

The spectrum obtained from expression (7.1) can be averaged over S pulses (or revolutions). The averaging can either be performed for the complex pressure amplitudes or their squared absolute values as shown in the following expressions.

$$A^m_n = \frac{1}{S} \sum_{j=1}^{S} a^m_{j,n}, \tag{7.2}$$

$$B^m_n = \frac{1}{S} \sum_{j=1}^{S} \frac{1}{2} \left| a^m_{j,n} \right|^2. \tag{7.3}$$

Expression (7.2) is used to perform averaging of the complex pressure amplitudes which results in filtering out the non-periodic (broadband) noise and expression (7.3) is used to perform averaging of the squares of the magnitude of the complex pressure amplitudes which preserves the non-periodic (broadband) component. In the analysis used in this study, the averaging is performed over 50 pulses. The SPL obtained from the averaged

spectra in expressions (7.2) and (7.3) are calculated by using the following expressions.

$$SPL(A_n^m) = 10.\log_{10}\left(\frac{\frac{1}{2}\left|A_n^m\right|^2}{4.10^{-10}}\right), \tag{7.4}$$

$$SPL(B_n^m) = 10.\log_{10}\left(\frac{B_n^m}{4.10^{-10}}\right). \tag{7.5}$$

Expressions (7.4) and (7.5) are then used to produce mode detection plots of the sound pressure level on the wall against circumferential mode number m, for different engine orders (EO) n. Expression (7.4) derived from averaging the complex pressure amplitudes is used to produce mode detection plots for tones which are periodic, and expression (7.5) derived from averaging the squares of the magnitudes of the complex pressure amplitudes is used to produce mode detection plots for broadband noise.

7.2.3 Predicted data at the Blade Passing Frequency (BPF)

Far field SPL field shapes have been predicted at BPF tone frequencies for the 1/3-scale model fan rig in Figure 7.1. The predictions are made for hard-walled and lined intake barrel configurations at a number of fan speeds. The source is assumed to consist of a multimodal component which in the first instance is assumed to contain equal power per mode for all cut-on modes, and an additional rotor-locked component corresponding to the first radial mode of circumferential mode number m, equal to the number of fan blades ($m = 24$), when the fan tip speed is supersonic and this mode is cut-on. All of the cut-on modes which are included in the multimodal content as well as the rotor-locked $m = 24$ mode, are assumed to be uncorrelated.

At subsonic tip speeds (50% to 70% fan speed), the '$m = 24$' mode is cut-off and the noise source is therefore modelled simply as a multimodal source with equal power in all the cut-on modes. Above 80% fan speed however, the '$m = 24$' mode is cut-on and the noise source is represented by both contributions. From the predicted data, the far field field shapes of the complex acoustic pressure magnitude for each of the modes prescribed at the fan plane are summed as contributions from uncorrelated modes as given in the

expression below,

$$|p|^2 = \sum_{i=1}^{N} |p_i|^2, \tag{7.6}$$

where p_i is the complex acoustic pressure from the ith mode at the fan plane and N is the number of modes present. The sound pressure level is then calculated using the following expression:

$$SPL = 20 \log_{10} \frac{|p|}{\sqrt{2}} \frac{1}{p_{ref}}, \tag{7.7}$$

where $|p|/\sqrt{2}$ is the root mean square pressure and reference pressure p_{ref} is 2×10^{-5} Pa.

Measured data are taken for the case of a hard-walled and a lined intake. The hard-walled case is used to calibrate the fan source model for the numerical analysis. Figure 7.3 displays mode detection data for a hard-walled intake taken by the ring of transducers close to the outlet flare shown in Figure 7.1. The measured SPL on the wall is decomposed as described earlier, into components corresponding to each circumferential mode number m, and plotted to show the variation of each component with fan speed at EO = 24 (BPF). For fan speeds less than 80% the modal SPL is distributed fairly evenly over an expanding

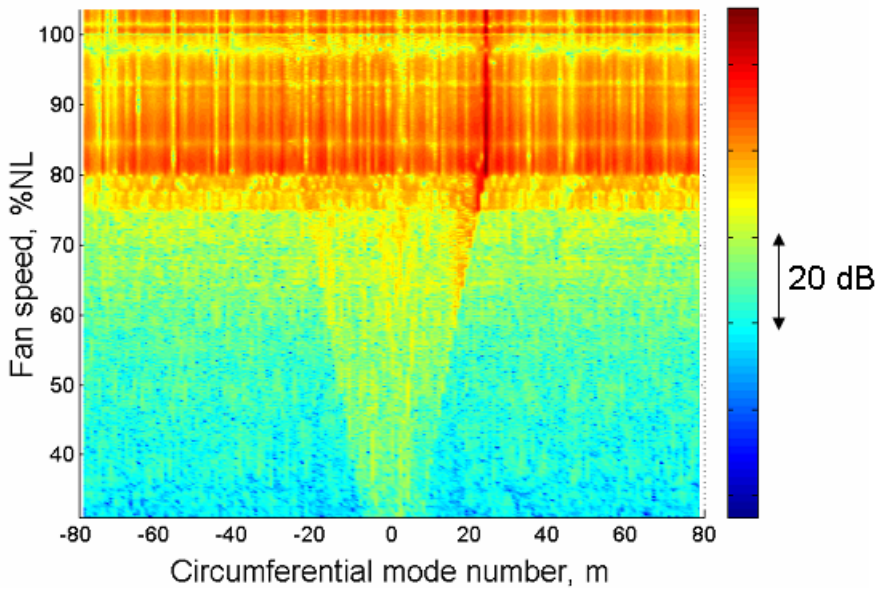

Figure 7.3: Mode detection plot at 1 BPF (EO = 24) showing the variation of sound pressure level with circumferential mode number and fan speed.

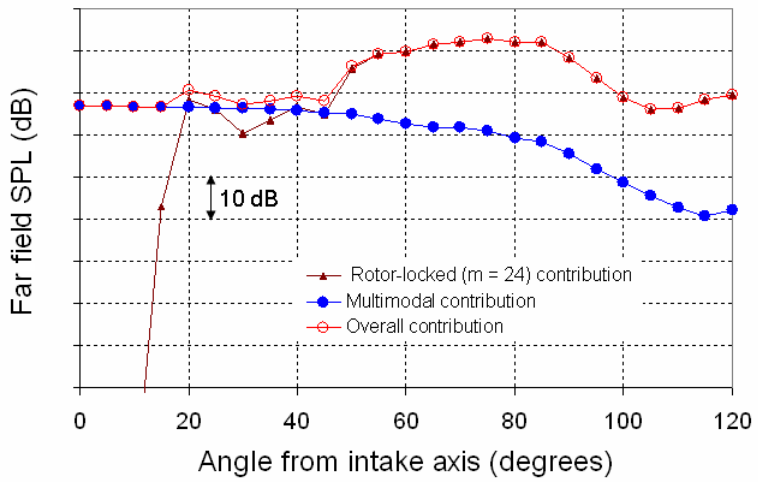

Figure 7.4: Typical prediction of the overall far field SPL field shape at 80% fan speed for a hard-walled intake.

range of circumferential orders corresponding to cut-on modes. However, for fan speeds greater than 80% the '$m = 24$' mode is cut-on and strongly excited. When a modal source of this type, i.e. a strong '$m = 24$' contribution superposed on a multimodal source, is used as an input to ANPRORAD, the resulting far field SPL field shape reflects both sources. This is illustrated in Figure 7.4 which shows a typical prediction of the overall far field SPL field shape at 80% fan speed. The source is composed of a multimodal component and a strong '$m = 24$' contribution. The individual field shapes are shown for each component as well as the overall (summed) contribution.

7.2.3.1 Calibrating source levels to obtain absolute levels

In order to compare the predicted data with measured data, the source levels used in the prediction for the multimodal content and the '$m = 24$' tone are calibrated individually using measured hard-walled data from mode detection. To calibrate a prediction, the SPL is predicted at a node on the FE mesh at the location of the mode detection ring on the rig.

In the case where only a multimodal contribution is present, as shown in Figure 7.5(a),

the source levels are estimated from the far field SPL predictions by using a logarithmic factor equal to the difference between the predicted value at the node point and the measured SPL (Figure 7.5(a)) at the wall of the intake. The measured and predicted values are obtained by adding the contributions from all the circumferential modes incoherently by using expression (7.6).

At 80% and 90% fan speed when the rotor-locked '$m = 24$' mode is cut-on, the source level is estimated from the far field SPL prediction for this mode, by using a logarithmic factor equal to the difference between the predicted wall SPL, and the measured contribution from this mode. The latter is obtained from measured SPL data decomposed into circumferential modes as shown in Figure 7.5(b). For the multimodal content however, the high pressure amplitude in the rotor-locked '$m = 24$' mode and the limitation of a dynamic range of 18.2 dB for the mode detection ring means that, the measured multimodal content of the source at these speeds is unreliable and hence cannot be used to calibrate the source levels for the ANPRORAD predictions. An approximate approach is used to obtain absolute levels. This is done by adjusting the predicted far field SPL directivity curves to match the measured data for far field polar angles in the range 0 to 20 degrees, where the multimodal content dominates over the '$m = 24$' contribution.

7.2.3.2 Comparing predicted results to measured data

Predicted results for the far field SPL field shapes at BPF tone frequencies for 50%, 60%, 70%, 80% and 90% fan speeds are shown in Figures 7.6 to 7.10 for hard-walled and lined cases. A summary of the BPF tone frequencies and Mach numbers at the fan plane for each condition is presented in Table 7.1. The source strengths obtained from the hard-walled data, as detailed in the preceding section, are used for both the hard-walled and the lined predictions.

Comparisons of hard-walled predictions and measured data are good at all angles at all fan speeds as one might expect. The results for the lined cases generally show a good agreement with the measured data for fan speeds up to 80%. However at 90% fan speed

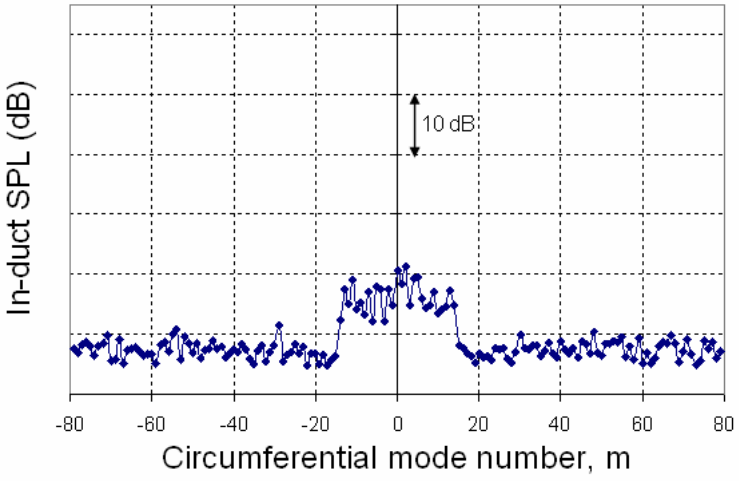

(a) 50% fan speed.

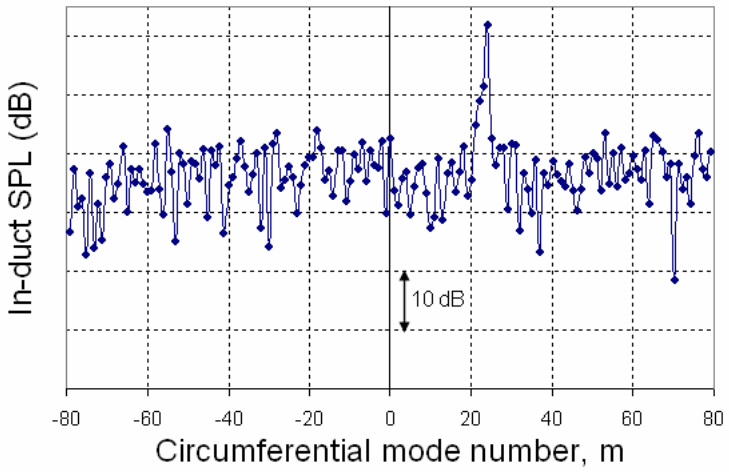

(b) 80% fan speed.

Figure 7.5: Mode detection plots at 50% and 80% fan speeds at 1 BPF (EO = 24).

(Figure 7.10), ANPRORAD over-predicts the overall attenuation due to the liner. This results from an over-prediction of the attenuation of the rotor-locked '$m = 24$' mode. It may also be the case that ANPRORAD over-predicts the attenuation of the '$m = 24$' mode at 80% fan speed, even though the predicted results for the lined case agrees with the measured data. At 80% fan speed the '$m = 24$' mode, which is just cut-on, is very highly attenuated by the liner such that only the multimodal contribution is relevant in the lined intake. Consequently, any over-prediction of the '$m = 24$' mode is not evident since its level is already lower than the floor set by the multimodal contribution. At 90% fan speed however, the '$m = 24$' mode is well cut-on and hence less attenuated and therefore contributes to the overall far field SPL field shape at most angles (see Figure 7.10). In the lined result obtained from ANPRORAD, the attenuation of the '$m = 24$' mode therefore appears to be over-predicted. This could be caused by non-linear effects that occur close to the fan plane which are not considered in the linear ANPRORAD prediction.

To correct for the over-prediction of the liner attenuation of the rotor-locked '$m = 24$' mode due to non-linear propagation, a non-linear model FDNS [105,108] is used to predict the attenuation of this mode. In this study, FDNS is used to obtain the attenuation for the lined case including non-linear effects close to the fan. This attenuation is then applied to the predicted hard-walled SPL field shape obtained from ANPRORAD. Figure 7.11 shows the effect of non-linear propagation illustrating the difference in liner attenuation between a linear prediction and a non-linear prediction, with $\Delta_{linear} > \Delta_{non-linear}$.

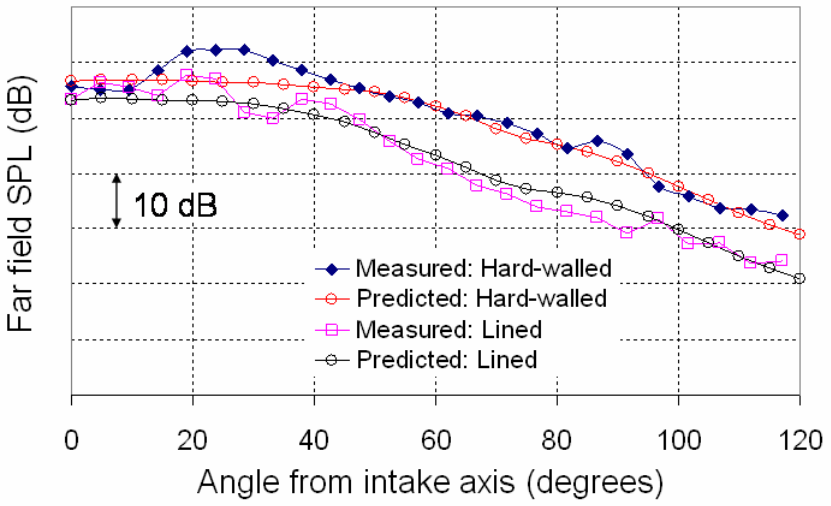

Figure 7.6: 1 BPF, 50% fan speed - predicted data versus measured rig data.

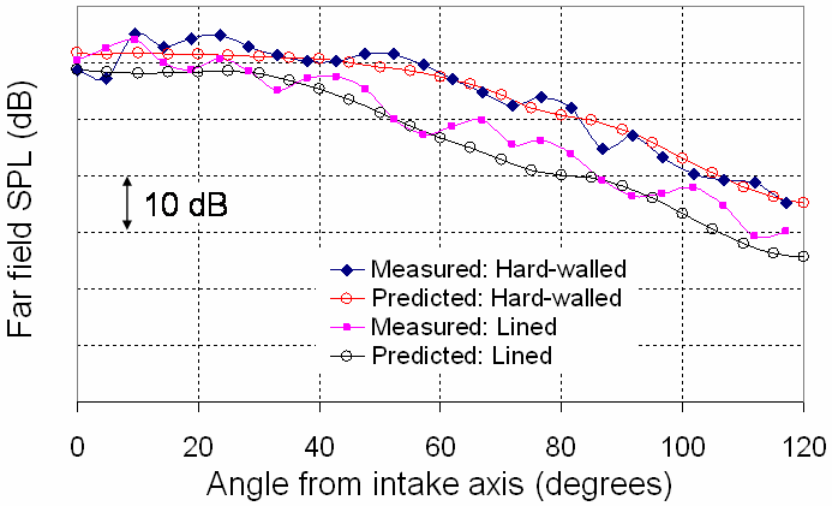

Figure 7.7: 1 BPF, 60% fan speed - predicted data versus measured rig data.

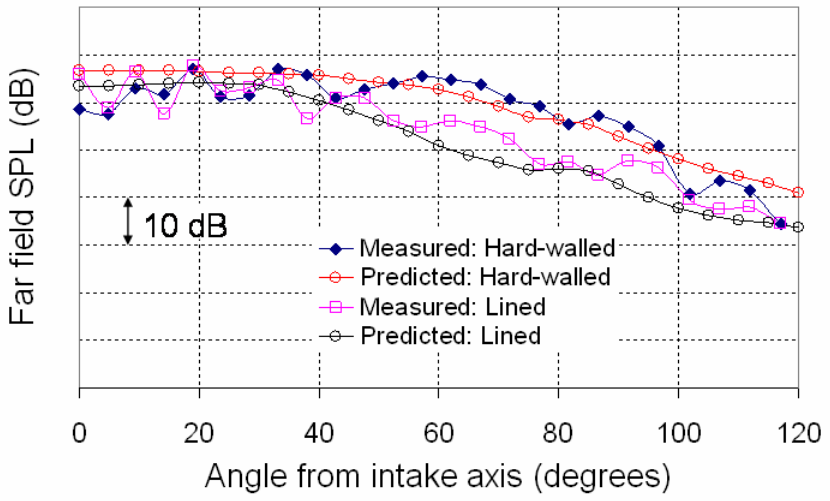

Figure 7.8: 1 BPF, 70% fan speed - predicted data versus measured rig data.

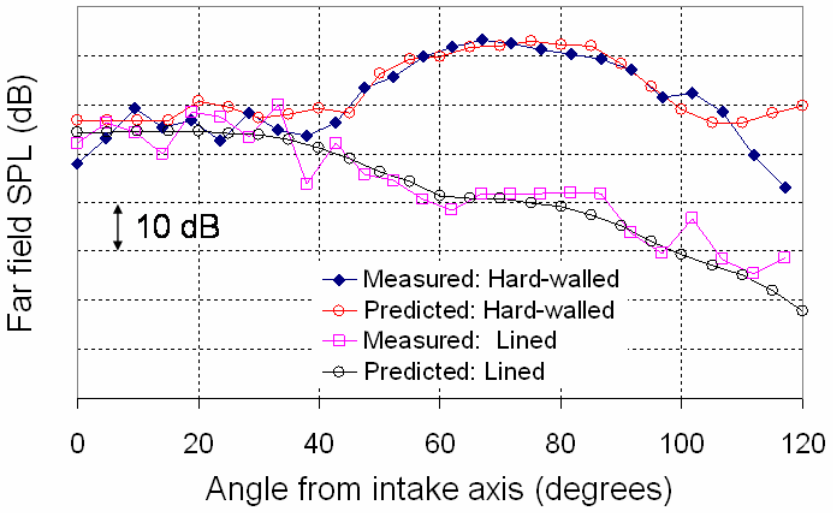

Figure 7.9: 1 BPF, 80% fan speed - predicted data versus measured rig data.

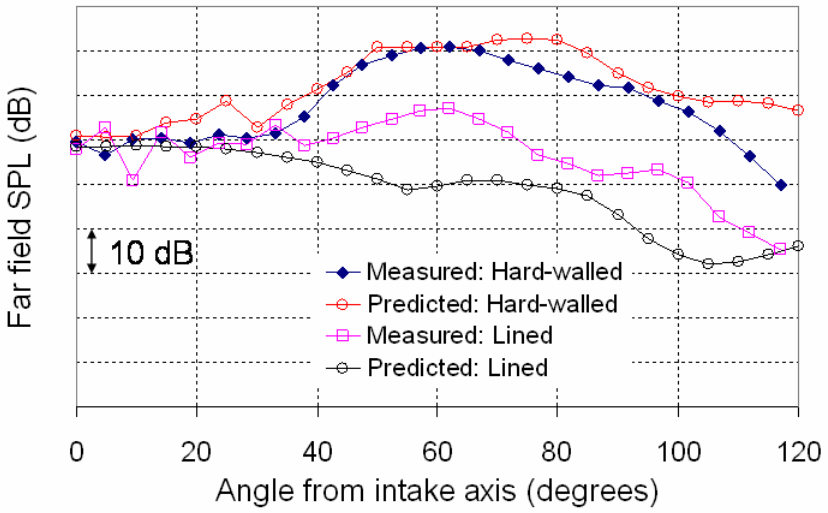

Figure 7.10: 1 BPF, 90% fan speed - predicted data versus measured rig data.

Table 7.1: BPF and Mach number at different rig fan speeds.

Fan speed (%NL)	50	60	70	80	90
BPF (Hz)	1928.4	2319.7	2713.9	3096.2	3486.9
Fan plane Mach number	0.23	0.30	0.37	0.44	0.55

In the non-linear prediction of the liner attenuation of the rotor-locked '$m = 24$' mode at 90% fan speed, the first and second radial modes are considered. Although in FDNS it is assumed that only the first radial mode is present, an approximate liner attenuation for the second radial mode can be obtained if the decay rate for the second radial mode is used. In this analysis the first and second radial modes are assumed to carry equal acoustic power. Given that more realistic decay rates for EO modes can be achieved with the inclusion of a boundary layer (see reference [108]), decay rates for the first and second radial modes are obtained for a uniform mean flow with a 4% boundary layer (typical of current designs) on the intake wall.

Figure 7.12 shows an improved result obtained by using FDNS for the liner attenuation of the '$m = 24$' modes. The disparity between field shapes in the measured and predicted

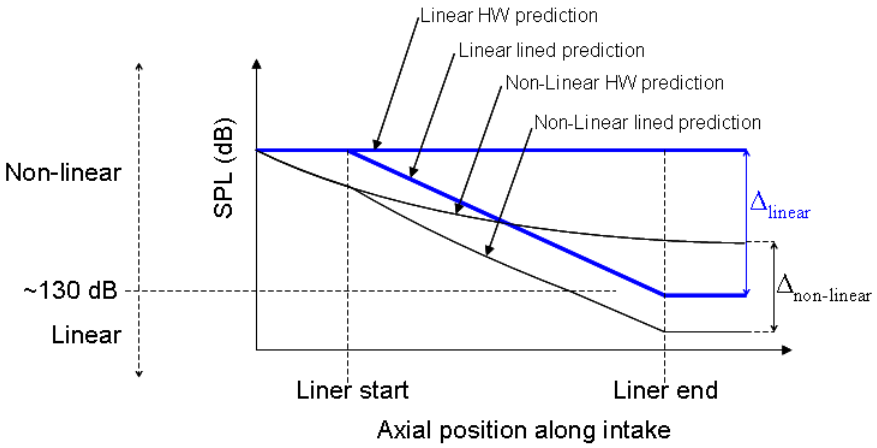

Figure 7.11: Effect of non-linear propagation illustrating the difference in liner attenuation between a linear prediction and a non-linear prediction ($\Delta_{linear} > \Delta_{non-linear}$).

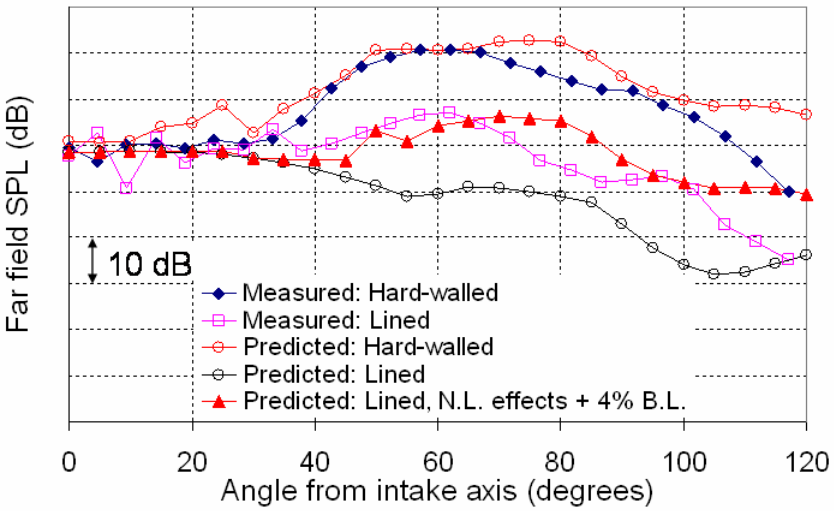

Figure 7.12: Effect of a boundary layer and non-linear effects on the attenuation of EO modes at 1 BPF at 90% fan speed.

results is smaller than before but the correspondence is still not completely satisfactory. This could be due to the fact that the interaction between the first and second radial modes is not modelled in either the linear ACTRAN or the non-linear FDNS solution.

7.2.4 Broadband noise: predicted versus measured data

ANPRORAD predictions have also been performed at lower fan speeds (50%) where fan broadband noise is the dominant noise source. The same multimodal source is used as in the previous section, and equal power per mode is assumed in all the cut-on modes. The modal contributions are summed incoherently. Predicted and measured SPL attenuations at 50% fan speed are shown in Figure 7.13. The predicted data agree with the measured data at most frequencies, at 2410 Hz for example, but not at all frequencies (e.g. 3150 Hz and 4000 Hz). This suggests that, an 'equal power per mode' assumption may not always

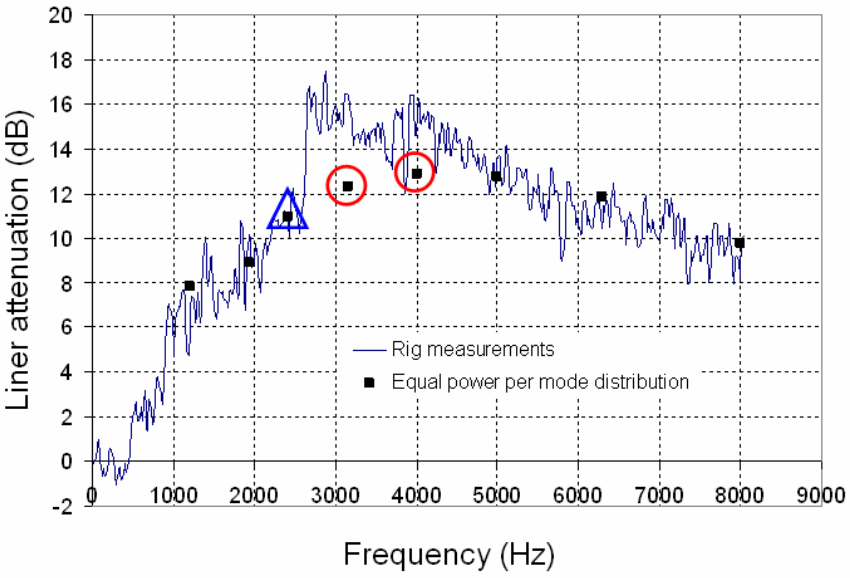

Figure 7.13: Predicted and measured liner SPL attenuation levels at polar angle 60 degrees from the intake axis at 50% fan speed ((blue) triangle shows consistent result at 2411 Hz and (red) circles show inconsistent results and 3150 Hz and 4000 Hz).

accurately represent the source. This will in fact be shown to be the case at 3150 Hz and 4000 Hz, where a misrepresentation of the source leads to an under-prediction of the liner attenuation. In these cases, predictions using a more precise modal power distribution matched to measured data can be used to improve the agreement between the predicted and measured data.

7.2.4.1 Broadband mode detection

To understand why an 'equal power per mode' distribution gives a good result at 2411 Hz and not at 3150 Hz, measured data at 2411 Hz and 3150 Hz corresponding to EOs 30 and 39 were inspected in more detail. Figures 7.14(a) and 7.14(b) show the distribution of modal SPL against circumferential mode number m, and fan speed at frequencies which correspond to EOs 30 and 39 i.e. at frequencies equivalent to 30 $\times$ shaft rotation frequency and 39 $\times$ shaft rotation frequency. These plots indicate the strong presence of the '$m = 30$', and '$m = 39$' modes which cut-on at 80% fan speed as the fan tip speed goes supersonic. The strongly excited modes at '$m = 30$', and '$m = 39$' correspond to harmonics of a buzz tone (due to blade to blade differences in stagger angle) which occurs at multiples of the shaft rotation frequency.

These plots also suggest that intake fan broadband noise is dominated by modes spinning in the same direction as the fan (co-rotating, $m > 0$), compared to those spinning in the opposite direction (counter-rotating, $m < 0$). In a fan noise source diagnostic test, Premo and Joppa [111] also showed that intake fan broadband noise is dominated by co-rotating modes. A study by Sijtsma [112] has shown that this dominance of co-rotating modes could either be due to, the directivity of dipole sources on the stator (which is asymmetric with circumferential mode number) or rotor shielding of dipole sources on the stator.

At the approach condition (50% fan speed) EOs 30 and 39 correspond to frequencies of 2411 Hz and 3150 Hz respectively. At these frequencies, plots of wall $SPLs$ decomposed into circumferential mode numbers are shown in Figure 7.15. At 50% fan speed the cut-on

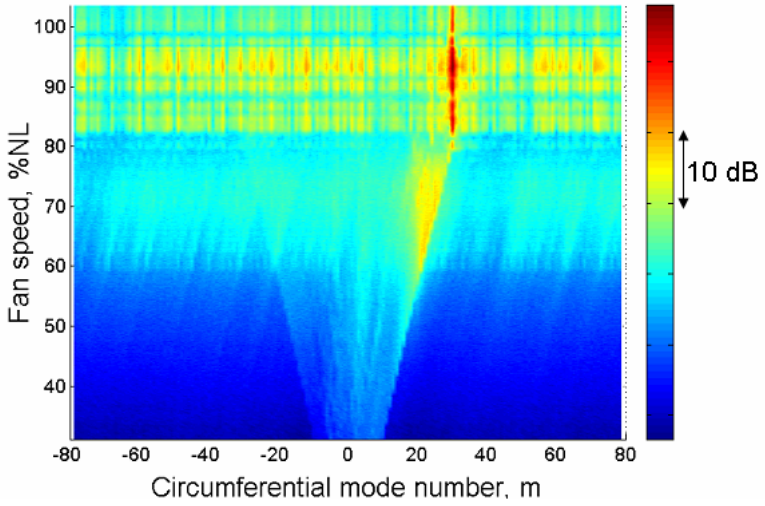

(a) EO 30 (30 × shaft rotation frequency).

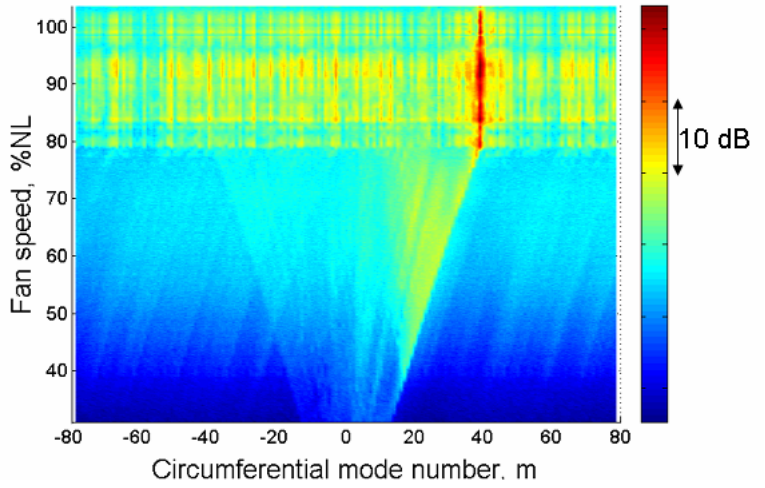

(b) EO 39 (39 × shaft rotation frequency).

Figure 7.14: Wall *SPLs* decomposed into circumferential mode numbers m, at different fan speeds.

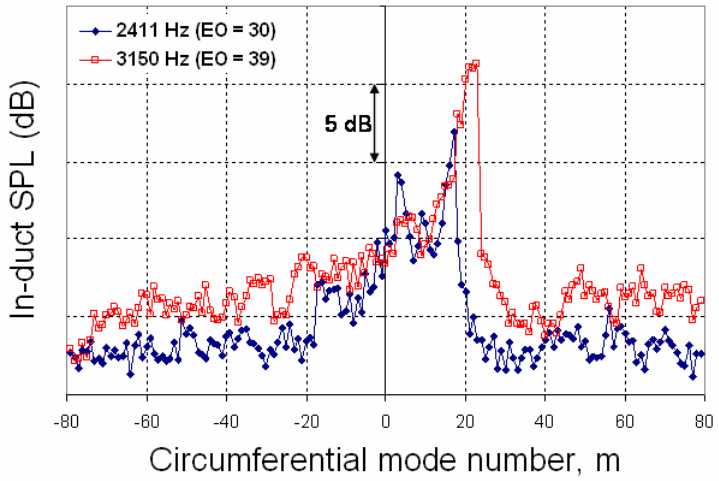

Figure 7.15: Wall $SPLs$ decomposed into circumferential mode numbers m, at 50% fan speed. 2411 Hz (cut-on range:$-17 \leq m \leq 17$) and 3150 Hz (cut-on range:$-23 \leq m \leq 23$).

mode range for EO 30 is $-17 \leq m \leq 17$ and $-23 \leq m \leq 23$ for EO 39. These plots again show that intake broadband noise is dominated by modes spinning in the same direction as the fan. However, at 50% fan speed, the bias towards co-rotating modes is more or less linear with m at EO 30 but rises more steeply with m for EO 39, as m approaches cut-off ($m = 23$).

7.2.4.2 Predicted results for broadband noise

Although Figures 7.14(a) and 7.14(b) show that intake broadband noise is dominated by co-rotating modes, ANPRORAD predictions shown in Figure 7.13 were performed by using an 'equal power per mode' source. Figures 7.16(a) and 7.16(b) show the measured and predicted far field SPL field shapes at 2411 Hz (EO 30) for hard-walled and lined configurations. Good agreement exists between the predicted and the measured data for the field shapes and the liner attenuations even though the modal distribution of energy is clearly asymmetric about $m = 0$. This is because the field shape of a co-rotating mode is the same as that of a counter-rotating mode with the same absolute circumferential mode number, m. In Figure 7.15 therefore, where the SPL variation with m is more

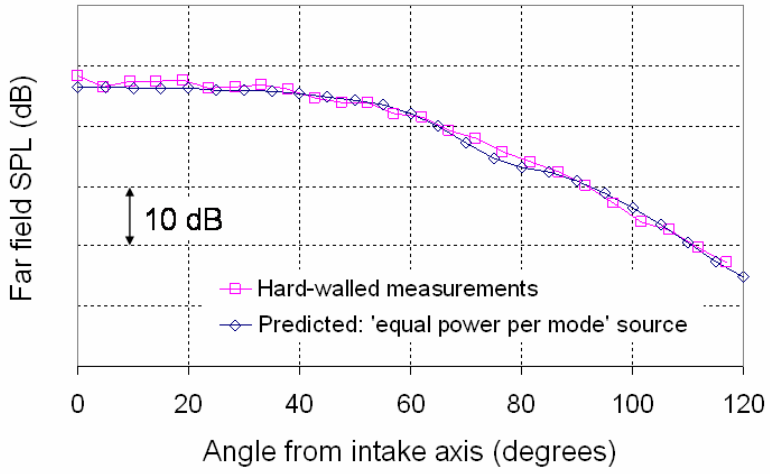

(a) Hard-walled field shapes.

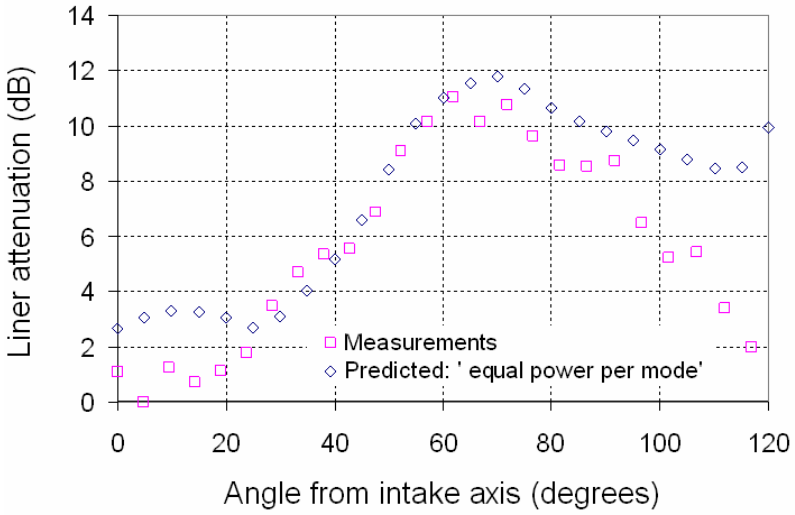

(b) Liner attenuations.

Figure 7.16: Comparison between predicted results using an 'equal power per mode' source at 50% fan speed at EO = 30 (2411 Hz), and measured data.

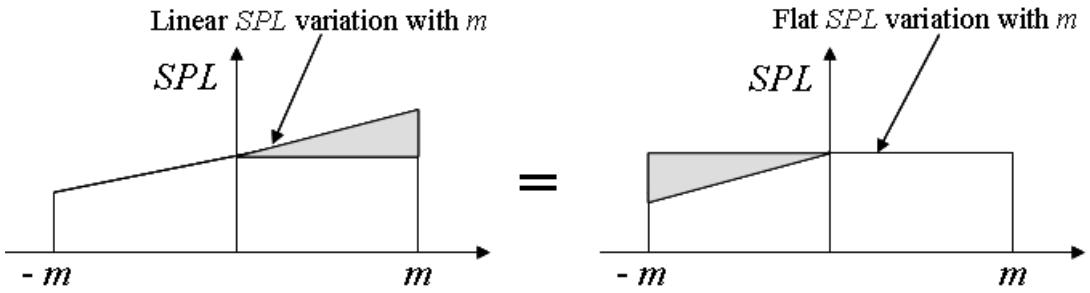

Figure 7.17: Illustration showing a linear SPL variation equivalent to a flat SPL variation, assuming modes are uncorrelated so that field shapes add and do not interfere.

or less linear at 2411 Hz, this gives the same overall field shape as a flat variation (see illustration in Figure 7.17) since the modes are assumed to be uncorrelated and the field shapes add but do not interfere. The distribution of modal energy shown in the linear SPL variation sketch in Figure 7.17, is therefore equivalent to an 'equal power per mode' distribution as far as the resulting field shape is concerned. For this reason an 'equal power per mode' distribution gives a similar field shape to a distribution that produces a linear SPL variation with m.

However, at 3150 Hz the SPL variation with m is disproportionately concentrated near $m = +23$ (see Figure 7.15) and the argument illustrated by Figure 7.17 does not hold. Predicted results using an 'equal power per mode' source do not compare well to measured field shapes and attenuations in this case (Figures 7.18(a) and 7.18(b)). In the next section, a modal power distribution derived from in-duct data for measured SPL is used in place of the 'equal power per mode' assumption to improve the predicted results at 3150 Hz.

7.2.4.3 Using in-duct data for measured SPL to modify the modal power distribution

The modal powers of the incident modes at the fan plane for each circumferential mode number has been modified to represent the effect of dominant co-rotating modes in an ANPRORAD prediction. The modification is such that when the pressure contributions

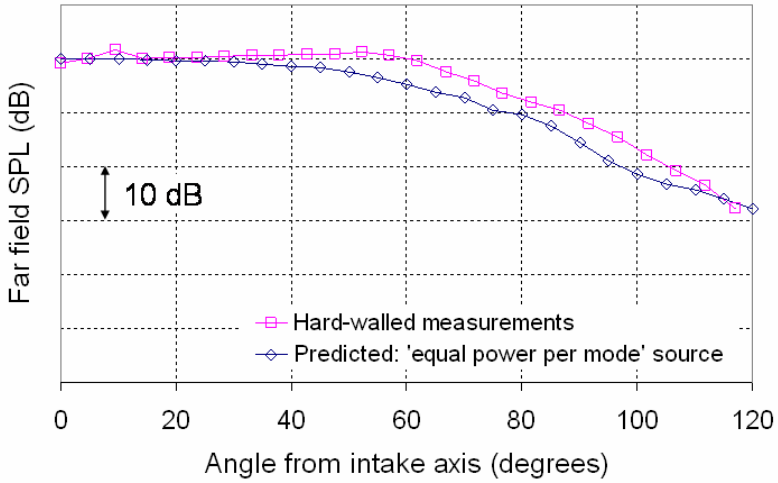

(a) Hard-walled field shapes.

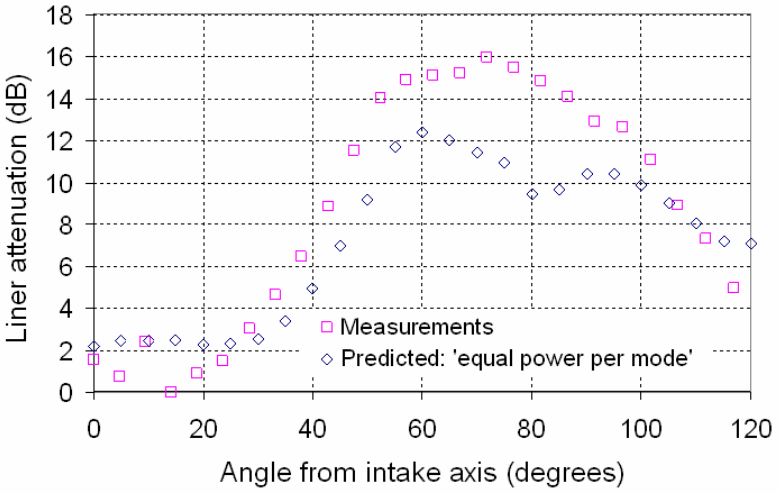

(b) Liner attenuations.

Figure 7.18: Comparison between predicted results using an 'equal power per mode' source at 50% fan speed at EO = 39 (3150 Hz), and measured data.

for each radial mode are summed as uncorrelated modes for each circumferential mode number, an SPL variation with circumferential mode number similar to measured data is obtained. The pressure contributions for each of the modes in the prediction are obtained at a node point on the FE mesh at the location of the mode detection ring on the rig. A plot of SPL versus circumferential mode number predicted at the node on the FE mesh corresponding to the location of the mode detection ring on the rig and assuming an 'equal power per mode' source at the fan plane is shown in Figure 7.19. In the prediction, the contributions from the negatively spinning modes are assumed to be the same as those from positively spinning modes with the same absolute circumferential mode number. It can be seen that the distribution of in-duct SPL with mode number is more or less even.

Figure 7.19 also shows data for measured SPL decomposed into circumferential modes using the method described earlier in section 7.2.2. The predicted values have been normalised so that they match the measured data at mode $m = 23$. The modal power P or modal intensity I[1] for a given mode is proportional to the square of the acoustic pressure contribution from that mode. This implies that:

$$I \propto 10^{SPL/10}. \tag{7.8}$$

By considering the contribution from each circumferential mode number in Figure 7.19, for a given prescription of modal intensity at the fan plane, the modal intensity required to give a distribution of SPL with circumferential mode number which is consistent with the measured data is given by:

$$I_m = \frac{10^{SPL_m/10}}{10^{SPL_{epm}/10}} I_{epm}, \tag{7.9}$$

where I_m is the modified modal intensity at the fan plane for modes with a given circumferential mode number m, I_{epm} is the modal intensity for equal power per mode prescribed at the fan plane, SPL_m is the measured SPL for a given circumferential mode number

[1]Even though the source is described as an 'equal power per mode' source, modal intensities are used in the prediction. Intensity I and power P are interchangeable since $I = P/A$, where A is the fan plane cross-sectional area which is a constant

and SPL_{epm} is the predicted SPL for an 'equal power per mode' source. By using Equation (7.9), the modal intensities for an 'equal power per mode' source can be modified so that the predicted SPL variation with circumferential mode number in Figure 7.19 matches the measured data.

Bar charts of the modal intensities for all the cut-on modes at 3150 Hz for an 'equal power per mode' source and for the distribution of modal powers matched to measured data are shown in Figures 7.20(a) and 7.20(b) respectively. Predictions of far field SPL performed at 3150 Hz when the modified modal power distribution in Figure 7.20(b) is used to describe the noise source are shown in Figures 7.21(a) and 7.21(b). These give a better agreement with measured data for hard-walled field shapes and a closer prediction of the attenuation due to the liner.

Figure 7.22 shows a comparison between predicted and measured liner attenuations at discrete broadband frequencies from 1.2 kHz to 8 kHz, at polar angle 60 degrees from the intake axis, in which an 'equal power per mode' source has been used in the prediction at all frequencies, except at 3150 Hz and 4000 Hz. At these frequencies, the modal power distributions were observed to differ significantly from the equal power model, and modified distributions matched to measured data were used. Predicted and measured liner attenuation levels then show good agreement across the full frequency range. It is not clear why the modal power distribution is different at these two frequencies (3150 Hz and 4000 Hz). Nevertheless, this study highlights the importance of defining the source correctly in order to use propagation models to accurately predict far field SPL field shapes and liner attenuations.

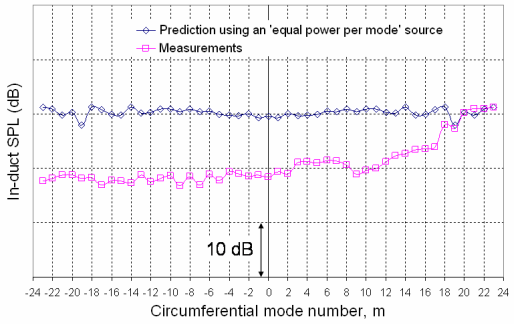

Figure 7.19: In-duct SPL contributions from each circumferential mode number for measured, and predicted data using an 'equal power per mode' source.

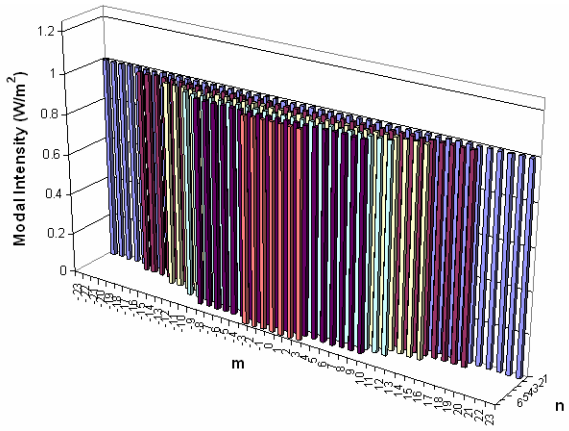

(a) 'Equal power per mode' distribution.

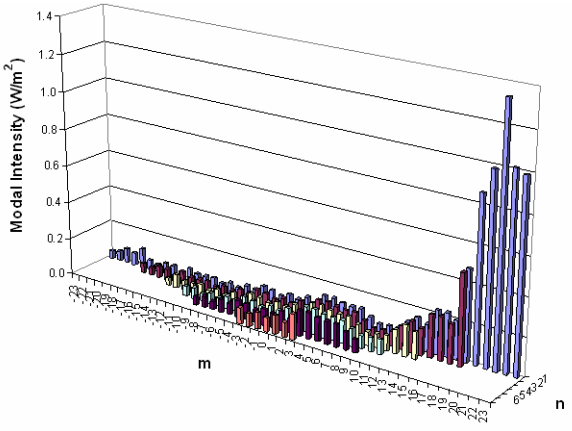

(b) Distribution derived from measured data.

Figure 7.20: Variation with circumferential mode number m and radial order n (3150 Hz).

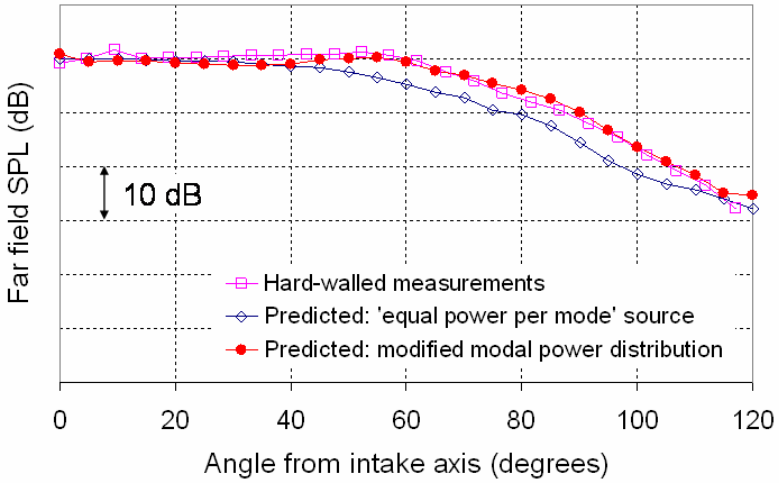

(a) Hard-walled field shapes.

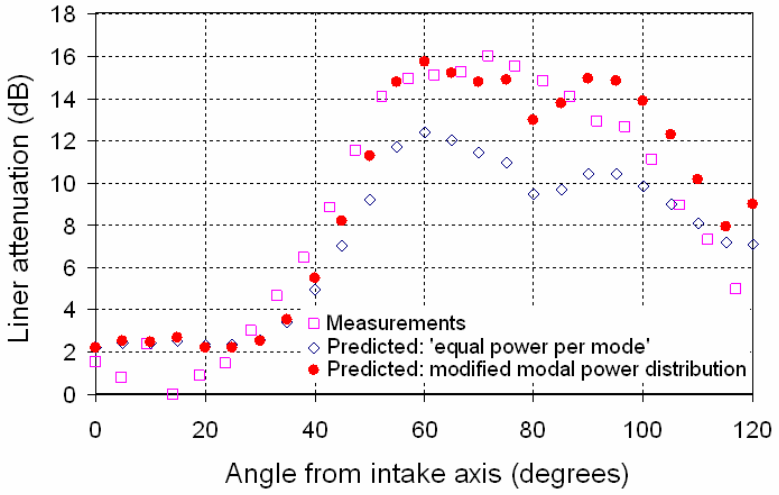

(b) Liner attenuations.

Figure 7.21: Comparisons showing improvement in predicted results from using a source modal power distribution matched to measured data (3150 Hz).

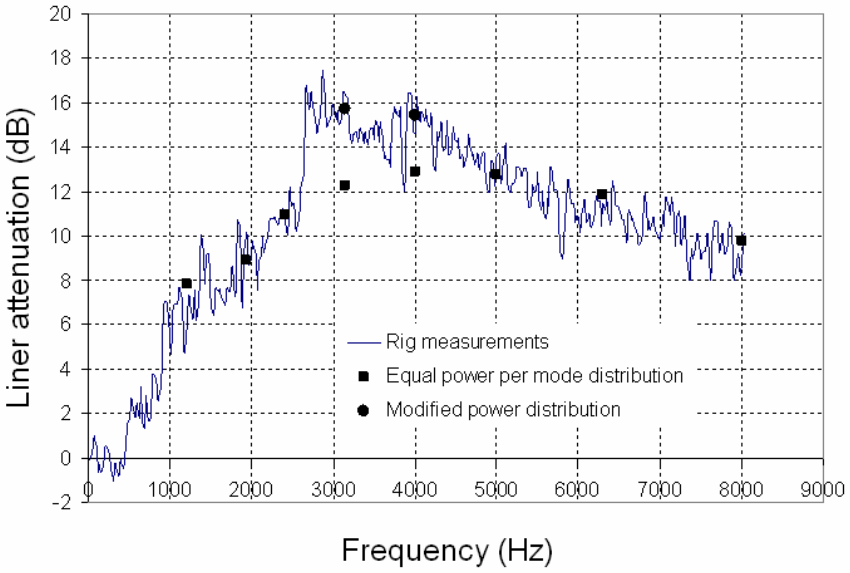

Figure 7.22: Comparison between predicted and measured liner SPL attenuation levels at polar angle 60 degrees from the intake axis at 50% fan speed (dots show improved results using modified modal distribution at 3150 Hz and 4000 Hz).

7.2.5 Discussion

Predicted far field SPL field shapes obtained from ANPRORAD have been validated for a number of cases against measured fan rig data. The predicted data are calibrated to obtain absolute levels by using mode detection data for a hard-walled intake taken from a ring of pressure transducers close to the highlight. From this validation exercise, some key conclusions about the noise source at BPF and broadband frequencies can be drawn.

In the prediction model, for BPF tones the source is described as multimodal at subsonic tip speeds, and composed of a multimodal content and a high amplitude rotor-locked $m = N$ (for an N-bladed fan) content at supersonic tip speeds. In the multimodal content, all the cut-on modes are considered and they are all assumed to be uncorrelated, and carrying equal acoustic power. Predicted far field SPL field shapes for hard-walled and lined cases show that, for BPF tones at subsonic speeds, an 'equal power per mode'

assumption is a good approximation for representing the multimodal content of the noise source. At supersonic tip speeds however, non-linear and boundary layer effects need to be incorporated into the current prediction model to predict the liner attenuation of the rotor-locked mode. In this thesis, a one-dimensional non-linear propagation model FDNS, developed by McAlpine and Fisher [105, 108] is used. A multi-dimensional analysis for non-linear propagation is being developed by Fernando *et al.* [113]

Generally, in forward radiated fan broadband noise, the noise is dominated by co-rotating modes. A study by Sijtsma [112] has shown that the dominance of co-rotating modes could either be due to, the directivity of dipole sources on the stator (which is asymmetric with circumferential mode number) or rotor shielding of dipole sources on the stator. However, at frequencies where this bias towards the co-rotating modes is reasonably linear with circumferential mode number, predicted field shapes and liner attenuations using an 'equal power per mode' approximation give a good agreement with measured data. Where this bias is disproportionate, the use of a more accurate power distribution derived from in-duct SPL measured data to define the noise source improves the accuracy of the predicted field shapes and liner attenuations.

7.3 Comparison between predicted field shapes and engine data

In this section, predicted far field SPL field shapes and liner attenuations for a 24-bladed Rolls-Royce turbofan engine are calculated at BPF and compared to measured engine data. The predicted results are obtained using the methods described in section 7.2.

7.3.1 Experimental set-up

Noise test data were acquired from a static engine test performed at the Rolls-Royce 11-Bed powerplant facility at Hucknall. The engine had a 24-bladed fan with a diameter of 2.94 m. The intake cowl used in the test is cambered (drooped) downwards relative to

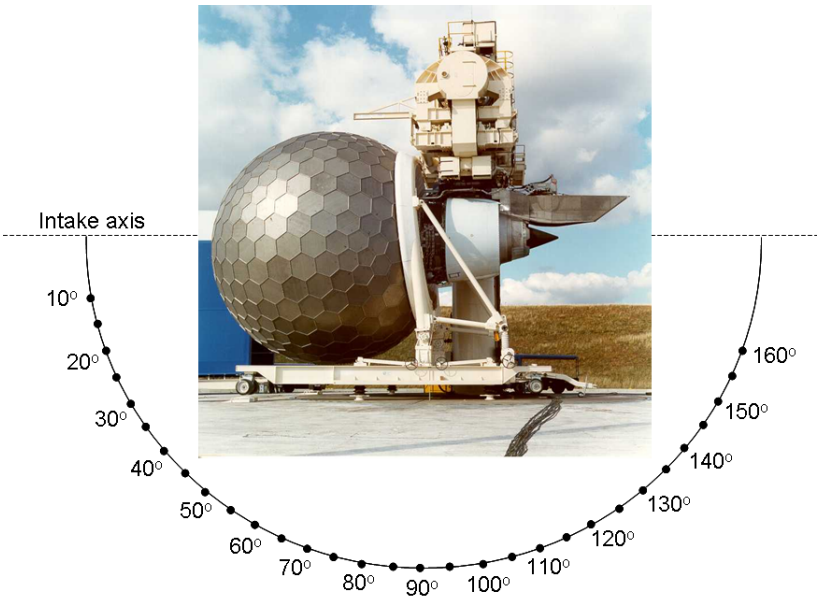

Figure 7.23: Engine mounted at the 11-Bed powerplant facility at Hucknall showing angle range of far field microphone array (reproduced by permission of Rolls-Royce plc).

the engine axis. The purpose of the droop in nacelle design is to take into account the angle of attack at which the aircraft operates. Also included in the intake is a noise flare around the lip, which is used to prevent flow separation during static engine tests. In order to simulate clean airflow in flight, a turbulence control screen (TCS) is attached to the inlet as shown in Figure 7.23.

The far field measured data were acquired using an array of ground microphones distributed at locations between 10 and 160 degrees relative to the intake axis, at 5 degree intervals (see Figure 7.23). During the test, in-duct measurements were also taken using an inlet mode array of 124 pressure sensors. With this array, reliable measurements were possible in the circumferential mode number range $-66 \leq m \leq 66$, with a dynamic range of 29.5 dB.

7.3.2 Mode detection data

Figures 7.24, 7.25 and 7.26 show in-duct SPL data decomposed into circumferential mode numbers m when the fan tip speed is subsonic at 50%, 60% and 70% fan speeds. Figures

7.27 and 7.28 show similar plots when the fan tip speed is supersonic at 80% and 90% fan speeds.

7.3.2.1 Distortion tones

The presence of a droop on the intake distorts the circumferential variation of the mean flow going unto the fan. When this happens, interaction tones are generated as the rotor-locked pressure field is modulated by a factor representative of the periodicity of the mean flow distortion (typically $m = 1$ for simple droop), these tones only propagate when the circumferential phase speed at the outer wall is supersonic. In the mode detection plots, there is some evidence of mean flow distortion especially at 70%, 80% and 90% fan speeds.

At 70% fan speed, Figure 7.26 shows the strong presence of a tone at $m = 20$ even though the rotor-locked $m = 24$ mode is cut-off. This '$m = 20$' mode might be a distortion tone with a rotational speed that is greater than the shaft speed, such that the phase velocity at the wall is supersonic even though the fan tip speed is subsonic. In which case, the '$m = 20$' distortion tone will propagate even though the the rotor-locked mode is cut-off.

At 80% and 90% fan speeds, the fan tip speed is supersonic and the rotor-locked mode is cut-on. However, due to the distorted mean flow unto the fan, the energy in the rotor-locked $m = 24$ mode is scattered into neighbouring circumferential mode orders depending on the periodicity of the mean flow distortion. Figures 7.27 and 7.28 show the strong excitement of the rotor-locked $m = 24$ mode as well as neighbouring circumferential modes due to scattering into these modes.

7.3.3 Noise predictions

By using the same approach as described in section 7.2, engine noise predictions have been performed at the blade passing frequency (BPF, EO 24) for 50%, 60%, 70%, 80% and 90% fan speeds.

Given that the prediction method is axisymmetric, the three-dimensional (3D) droop

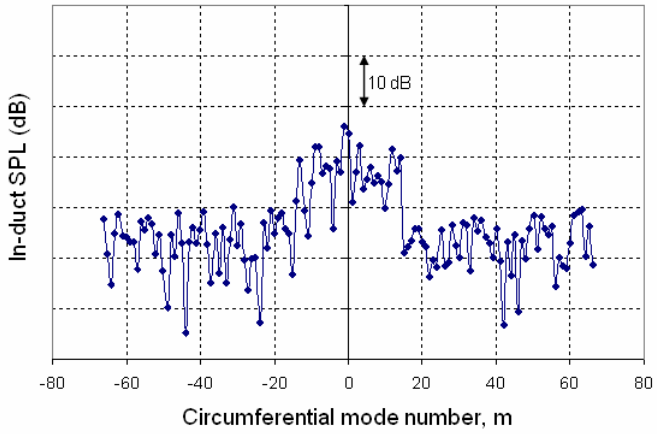

Figure 7.24: 50% fan speed - mode detection at 1 BPF.

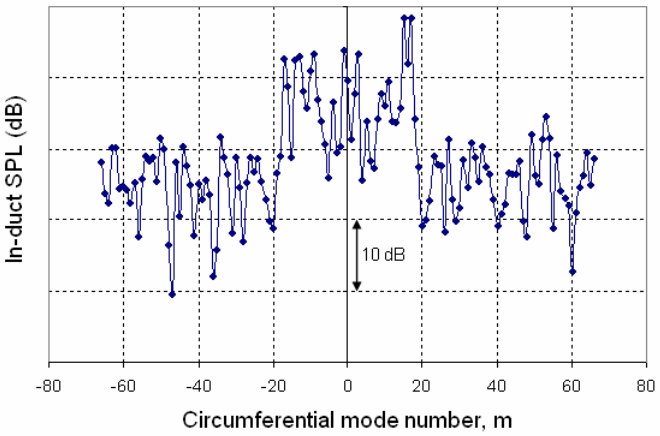

Figure 7.25: 60% fan speed - mode detection at 1 BPF.

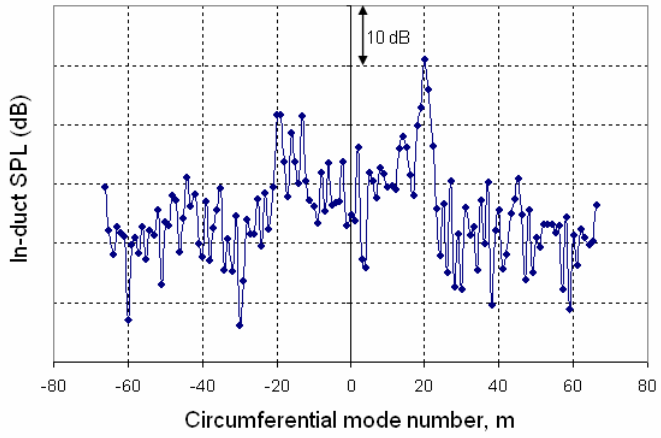

Figure 7.26: 70% fan speed - mode detection at 1 BPF.

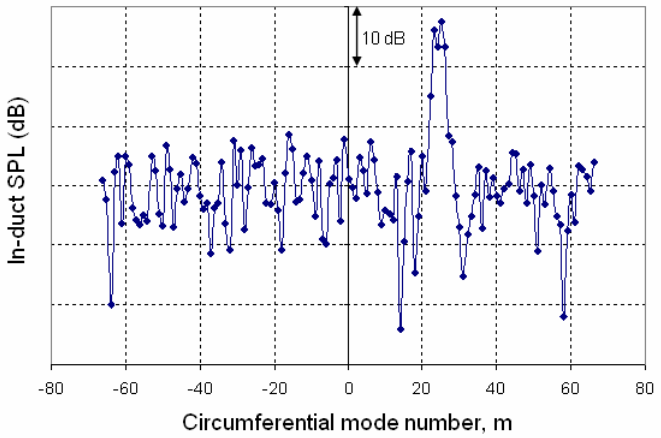

Figure 7.27: 80% fan speed - mode detection at 1 BPF.

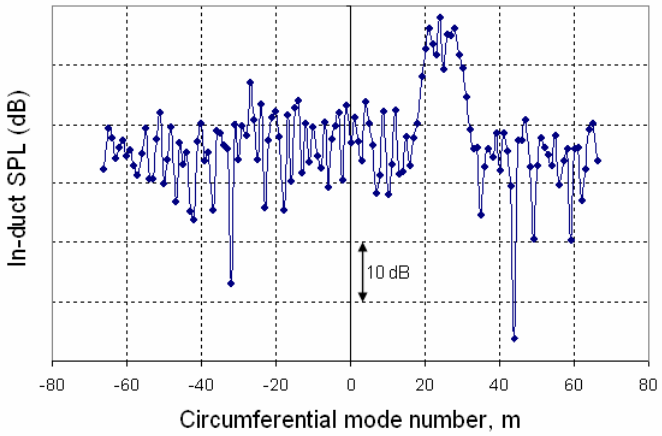

Figure 7.28: 90% fan speed - mode detection at 1 BPF.

on the engine cannot be accurately represented in this method. The engine intake geometry is therefore approximated by a two-dimensional (2D) slice (from the 3D geometry) rotated around the intake axis. This axisymmetric intake (see Figure 7.29) is then used in the prediction method. While this model will not be able to represent 3D geometric effects due to a drooped intake, the effect of droop on the fan source definition will be represented in the axisymmetric analysis through the mode detection data. In the BPF predictions at varying fan speeds, all the propagating modes are considered at each fre-

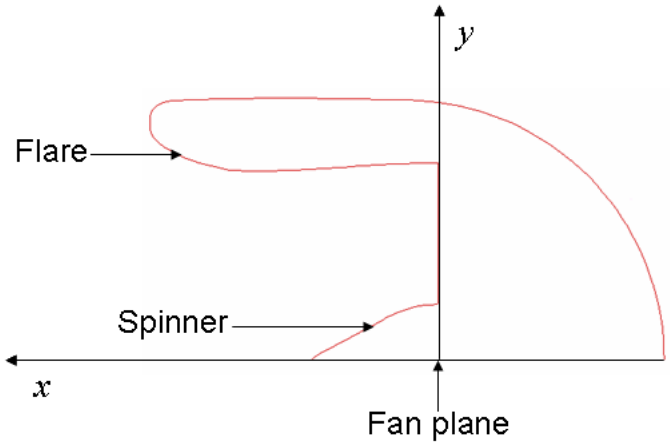

Figure 7.29: 2D slice showing intake geometry used to perform engine predictions.

Table 7.2: BPF and Mach number at different engine fan speeds.

Fan speed (%NL)	50	60	70	80	90
BPF (Hz)	584.7	695.3	810.5	928.3	1043.1
Fan plane Mach number	0.26	0.31	0.37	0.45	0.56

quency. A summary of the fan speeds and corresponding tone frequencies and fan plane Mach numbers are presented in Table 7.2. At 50% and 60% fan speeds, the source is represented by a multimodal content of uncorrelated modes which carry equal acoustic power. At 70% fan speed, due to the strong presence of a distortion tone at $m = 20$, the source is represented by a multimodal content and a high amplitude tone component at $m = 20$. At 80% and 90% fan speeds, the source is represented by a multimodal content and a rotor-locked $m = 24$ component. Also included at 80% and 90% fan speeds, are circumferential mode orders which contain energy scattered from the rotor-locked mode and have similar SPL levels to rotor-locked mode. At 80% fan speed high pressure amplitude modes included in addition to the rotor-locked mode are: $m = 23$, $m = 25$ and $m = 26$ (see Figure 7.27). At 90% fan speed, the additional modes range from: $19 \leq m \leq 23$ and $25 \leq m \leq 30$ (see Figure 7.28).

7.3.4 Results and Discussion

Predicted engine far field SPL field shapes for hard-walled and lined intakes at different fan speeds, are compared to measured data in Figures 7.30 to 7.34. The use of ground microphones for the engine noise measurements leads to a doubling of the pressure measured by the microphones, due to the effect of ground reflection. This in turn leads to measured SPL levels 6 dB higher than the ambient levels. In the results presented here, a correction factor of 6 dB is subtracted from all the measured SPL values.

Absolute levels for the predicted far field SPL field shapes are obtained by calibrating the source levels using in-duct measurements, using the method described in section 7.2.3.1. The measured far field SPL data is presented for microphones in the angular

range from 10 to 160 degrees. Predicted SPL data is presented for the same angular range. However, for the purpose of validating the current FE/IE prediction method for intakes, only data in the angular range from 10 to 90 degrees is important, since in the rear arc (angles greater than 90 degrees) the measured noise is contaminated by noise from the exhaust.

Figures 7.30, 7.31 and 7.32 show a comparison between measured and predicted data at different fan speeds (50%, 60% and 70%) with subsonic fan tip speeds. Between 0 and 90 degrees where the measured noise is dominated by forward radiated fan noise, the predicted data follow the general trend of the measured data. The predicted and measured attenuation levels are broadly similar if one assumes that the irregularities in the measured far field SPL field shapes can be attributed to 3D geometric effects, mean flow distortion and contamination from other sources not included in the prediction model.

At 80% fan speed, again there is a good overall agreement between the measured and predicted field shapes, which confirm that the attenuation of the rotor-locked and distortion tones is accurately predicted.

At 90% fan speed, there are significant irregularities in the measured SPL field shapes, and a comparison with the predicted field shapes is less straight forward. However, there is still a general trend which suggests the over-prediction of the attenuation of the rotor-locked and distortion tones, due to non-linear effects (see section 7.2.3.2). Non-linear effects are not included in the current prediction. It is also important to note that the effect of a boundary layer on the attenuation of these modes could be mitigated by the fact that many modes are present and refraction effects are less important.

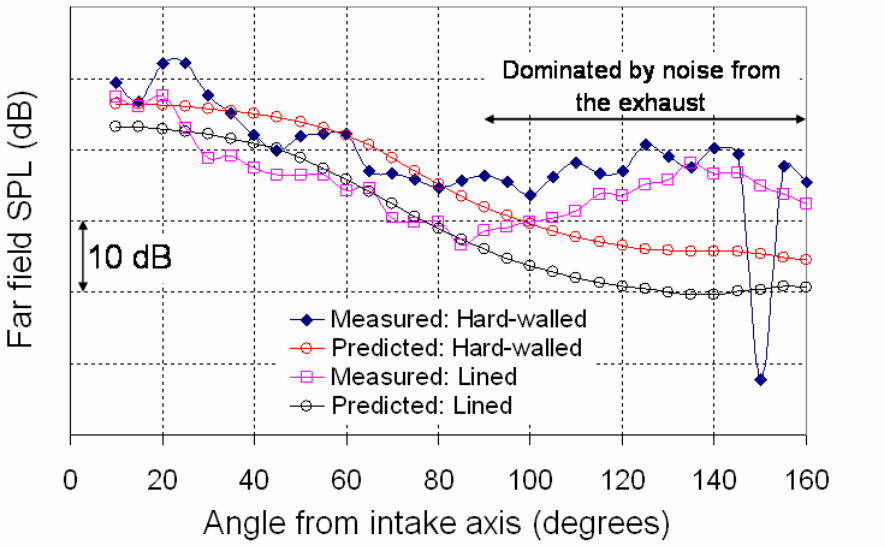

Figure 7.30: 1 BPF, 50% fan speed - predicted data versus measured engine data.

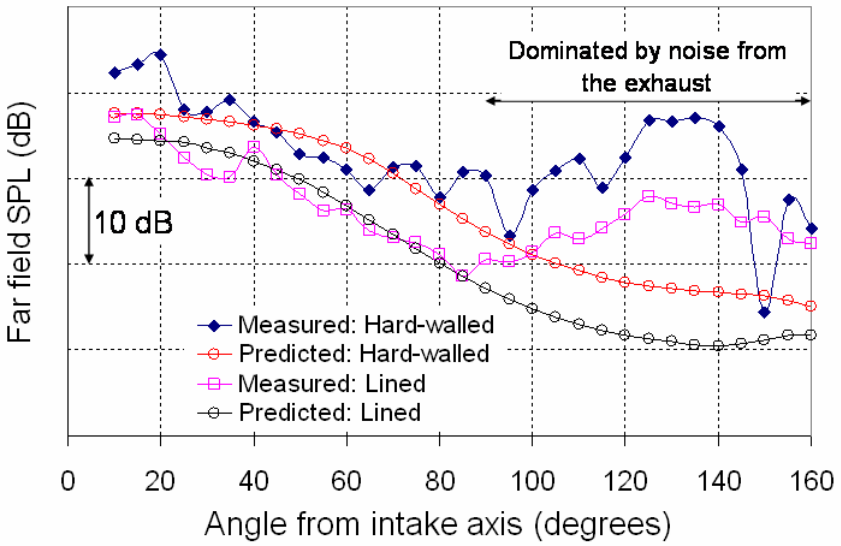

Figure 7.31: 1 BPF, 60% fan speed - predicted data versus measured engine data.

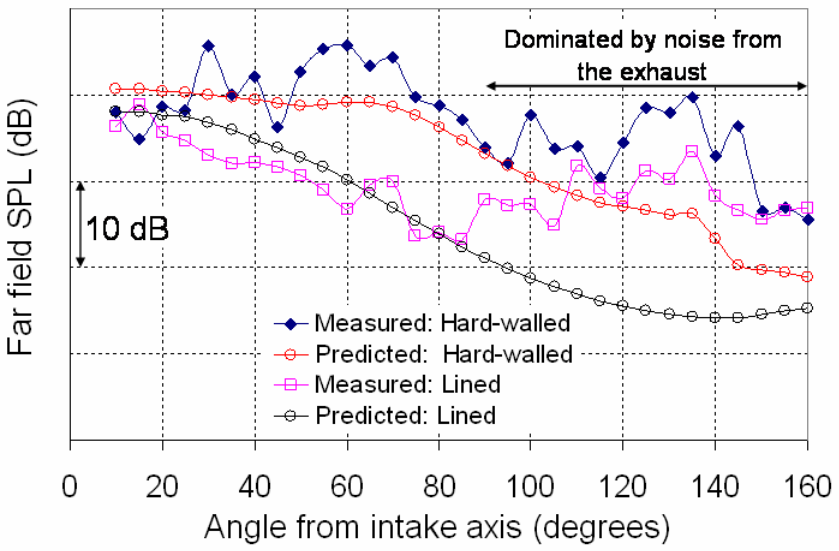

Figure 7.32: 1 BPF, 70% fan speed - predicted data versus measured engine data.

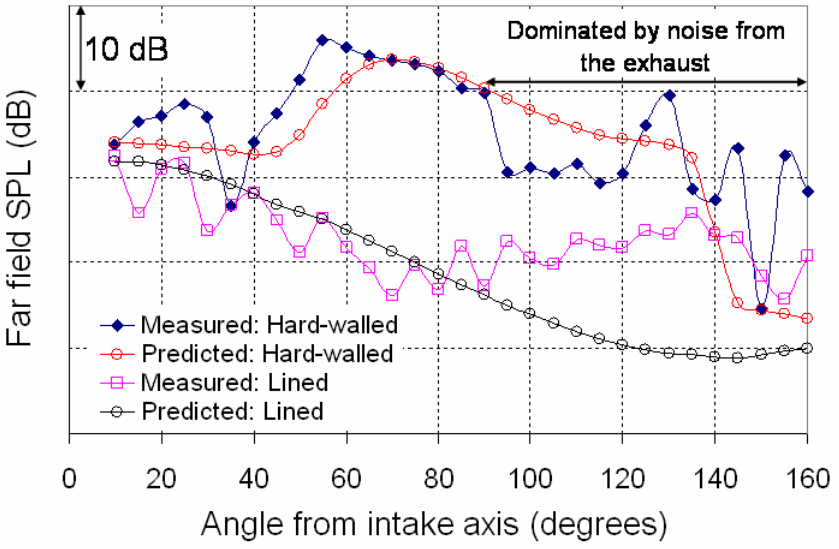

Figure 7.33: 1 BPF, 80% fan speed - predicted data versus measured engine data.

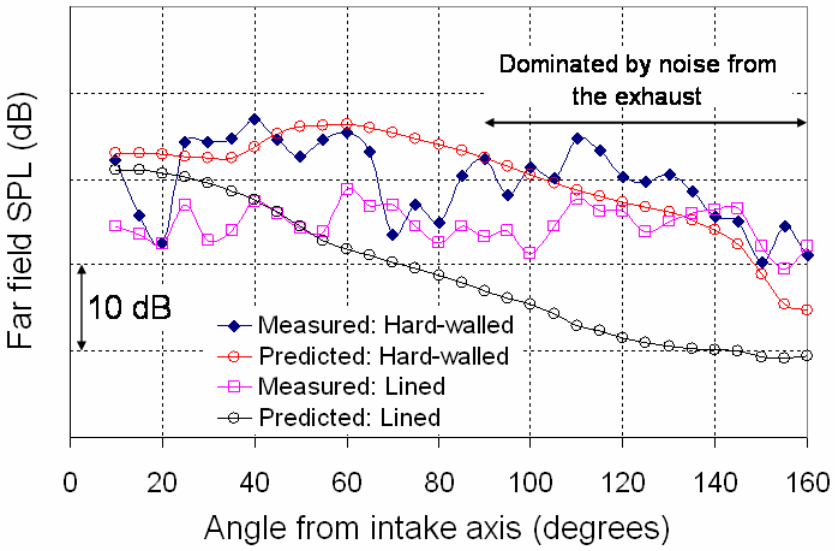

Figure 7.34: 1 BPF, 90% fan speed - predicted data versus measured engine data.

7.4 Conclusion

In this chapter a FE/IE approach implemented in ACTRAN/TM and ANPRORAD has been used to predict far field SPL field shapes for hard-walled and lined axisymmetric intake configurations. The predicted far field SPL field shapes and attenuations have been validated against rig and engine data at the different fan speeds including the approach (50% fan speed), cutback (80% fan speed) and sideline (90% fan speed) conditions.

Given that the rig data is generally cleaner than the engine data, a detailed validation exercise was performed first by using rig data, comparing predictions to the measured data. At BPF, results show that accurate absolute predictions of the far field SPL field shapes are possible for realistic intake geometries and flows in the absence of liners, provided that the source modal content is correctly specified. The prediction of attenuated tone field shapes for lined intakes requires the inclusion of adjustments to account for non-linear propagation close to the fan at supersonic fan tip speeds. For predictions at broadband frequencies, instead of using an 'equal power per mode' source, the dominance of co-rotating modes may have to be represented in the source to accurately predict hard-

walled far field SPL field shapes and liner attenuations.

The FE/IE approach has been at least partially validated for BPF tone predictions against engine data. The non-symmetric intake of the test geometry was not represented, but the presence of any measured distortion tones was included in the predictions in order to validate the measured data. In general, there is a reasonable agreement between the predicted and measured data. This implies that the 3D droop on the engine is important in the modification of the noise at source but has less geometric effect on its propagation and radiation. If so, a good representation of the modified source in an axisymmetric model can still give good results. In conclusion, while the 3D droop is important in terms of generating additional distortion tones it may not be so significant in terms of geometric scattering of the resulting sound field.

Chapter 8

Case study: Predicting intake effects on fan blade stability at low frequencies using ANPRORAD

8.1 Background

In turbomachinery applications, components experiencing high speed air flows such as fan blades in turbofan aeroengines are susceptible to vibration which can interact with the unsteady mean flow giving rise to coupled instabilities. It is important that such a phenomenon is taken into account during the design of the fan and intake.

In a study undertaken by Vahdati *et al.* [114], the stability of a ducted fan is coupled to the intake duct acoustics. These two factors can be investigated separately by considering the fan blade response and the intake acoustic domain as distinct entities. Individual analyses of these entities can be linked through the surface pressure on the fan blade from which the fan blade stability can be determined. The details of this procedure are beyond the scope of this thesis and are detailed in a method proposed by Imregun [115].

In the study performed by Vahdati *et al.* [114], it was concluded that the fan blade becomes unstable when the pressure perturbation due to the fan rotation and the blade

vibration matches an acoustic mode in the intake, in both frequency and shape. The first bending mode shape of the blade occurs when the blade tip has the largest response, and this is referred to as the first flap $1F$ mode. For a given first flap natural frequency ($1F$) mode, the frequency ω of the pressure perturbation due to the fan rotation and the blade vibration is given by [114]:

$$\omega = \omega_n + N\Omega, \tag{8.1}$$

where ω_n is the natural frequency of the blade $1F$ mode, N is the number of nodal diameters (ND) in vibration mode and Ω is the rotational speed of the fan.

By using Equation (8.1), a pressure perturbation mode can be obtained that can be used as an input into an intake duct acoustics model. When such a mode propagates in an intake, acoustic reflections can occur due to the variable cross-sectional area which leads to modes cutting off along the intake. The presence of liners can also cause absorption and reflection. These reflections can relieve or exacerbate fan blade instability. This will depend on the amplitude and phase of the reflected mode at the fan plane. A large reflected mode amplitude at the fan plane and/or a reflected mode in phase with the fan is most likely to reduce fan stability.

This chapter focuses on the intake duct acoustics model (rather than the fan response) and comprises of computations of the reflected mode amplitude and phase at a source plane at low frequencies, for a prescribed incident mode at this plane with a given amplitude and phase.

8.2 Introduction

In chapters 6 and 7, ACTRAN/TM within a shell program ANPRORAD for intakes, has been introduced and validated against measured rig and engine data.

In this chapter, ANPRORAD is used to predict the reflected mode amplitude and phase at a source plane at low frequencies, for a prescribed incident mode at this plane with a given amplitude and phase. In this chapter, modes corresponding to a fan vibration

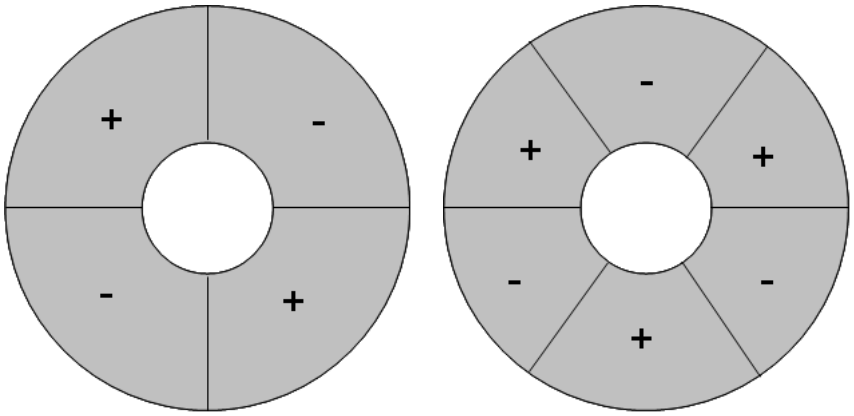

(a) Two nodal diameters (2ND). (b) Three nodal diameters (3ND).

Figure 8.1: Sketch showing unsteady pressure pattern (fan flap modes) generated by a rotating fan in two and three nodal diameter vibration mode.

mode with two or three nodal diameters (see Figure 8.1) are used as the incident modes at the source plane at low frequencies. This implies that, for the $1F$ vibration mode, acoustic modes (2,1) and (3,1) are considered, where the first digit is the circumferential mode number and the second digit is the radial order.

Given that in real applications, the intake may vary from engine to engine, the predictions are performed using different hard-walled intakes to investigate the effect of intake geometry. The predictions are also performed at a range of fan speeds.

Also, since the modes of interest occur at low frequencies, liners with large cell depths (deep liners) are required to target these frequencies. In this chapter, ANPRORAD is integrated within the in-house Rolls-Royce optimisation suite SOFT, and used to optimise the impedance of deep liners to minimise the amplitude of the reflected mode at the source plane.

8.3 Geometry effects on the 2ND and 3ND modes

In this section, computations are performed to assess the effect of three hard-walled intake geometries at different fan speeds on the reflection of 2ND and 3ND modes. The intakes

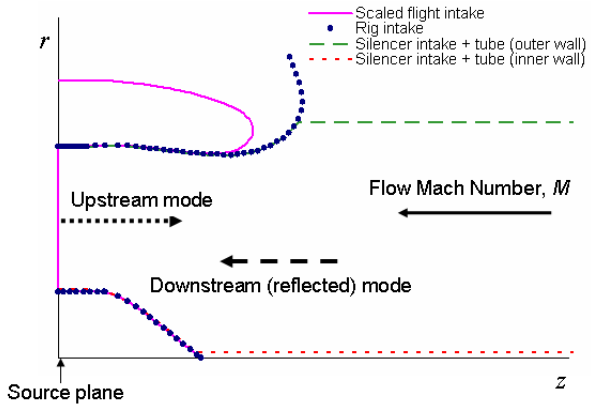

Figure 8.2: Intakes used to investigate effect of geometry.

used are: a scaled flight intake, a rig intake, and a modification of the rig intake which includes a cylindrical extension at the highlight (see Figure 8.2). The computations are performed for 2ND (2,1) and 3ND (3,1) modes incident at the source plane. The source plane is located at a small distance downstream of the fan plane with a uniform duct extension from the latter. This is to ensure a region of uniform flow upstream of the fan plane so that the reflected mode at the source plane is in a uniform flow region, since the mode shapes prescribed in the acoustic domain are for a uniform flow.

The reflected mode amplitudes computed by ANPRORAD are used to determine the reflection coefficient at the fan plane (see Figure 8.2). In the intake, when a mode cuts off it gets reflected. Reflections also occur at the intake highlight since the interface between the highlight and the surrounding acoustic region acts as an impedance discontinuity. In this study, plots are obtained showing the variation of the reflection coefficient at the source plane with fan speed, for each geometry, for the 2ND and 3ND modes as shown in Figure 8.3. The reflection coefficient is defined as the ratio of the reflected to the incident mode amplitude.

In Figure 8.3 the reflection coefficient is plotted against fan speed for 2ND and 3ND modes and different intake geometries. The peak reflection coefficient in each curve indicates the fan speed at which the incident mode (2ND or 3ND) cuts on at the source plane. As the fan speed increases beyond this point, the mode becomes more cut-on.

This leads to less energy being reflected downstream as the fan speed increases. This is because the modes which are more cut-on are reflected less, since they are less likely to cut-off when the duct cross-sectional area hence flow field changes along the intake. This trend is observed in Figure 8.3 for the 2ND and 3ND modes for all three geometries. In the curves for the 3ND modes, the peaks occur to the right of those for the 2ND modes, since the 3ND modes cut-on at a higher fan speed.

Considering the 2ND mode, Figure 8.4 shows plots of the imaginary part of the axial wave number k_z obtained from an in-house analytic code developed by McAlpine [105]. The axial wave number values are obtained for upstream and downstream propagating modes at different axial locations along the intake at 73% fan speed and 82% fan speed. These are superposed on a plot of the intake geometries. These fan speeds correspond to frequencies at which the 2ND mode is not well cut-on(73% fan speed) and well cut-on (82% fan speed). Although the computations for the axial wave number are performed just for the rig intake including the cylindrical extension, this geometry overlaps with the other two geometries, and hence the plot of the imaginary part of the axial wave number is equally relevant to these geometries in establishing where the 2ND mode is cut-on and where it is cut-off along the intake. For hard-walled ducts as examined in this section, the 2ND mode is cut-on when the imaginary part of the axial wave number is zero and cut-off when the imaginary part is non-zero. Figure 8.4 therefore shows where the upstream and downstream propagating 2ND mode is cut-on and cut-off (reflected) in each of the intakes.

In terms of assessing the effect of geometry, the plots in Figure 8.3 show that the reflection coefficients obtained for the scaled flight intake and the rig intake are similar at low fan speeds. However, they diverge at higher speeds as the modes become more cut-on. The similarity at low speeds could be due to the fact that, since the mode is cut-off over a significant portion of the intake, energy is reflected inside the intake. Consequently, since the mode has a smaller amount of energy when it reaches the highlight, the effect of the slightly different geometries (see Figure 8.2) at this point does not have a major impact on the overall reflection at the source plane. At high speeds however, the mode

is well cut-on in the intake, hence more energy reaches the highlight and slight variations in geometry at this point have a bigger effect on the reflection coefficient.

In the case of the modified rig intake with the cylindrical extension, the reflection coefficient is lower than that of the rig intake at all fan speeds. This is due to the anechoic boundary condition which is imposed at end of the cylindrical extension, which effectively ignores reflections from the impedance discontinuity at the highlight.

Figure 8.5 shows the variation in the phase difference (between incident and reflected modes) plotted against fan speed for 2ND and 3ND modes, for different geometries. This shows a linear variation of phase with fan speed for all three geometries when the modes are cut-on at the source plane.

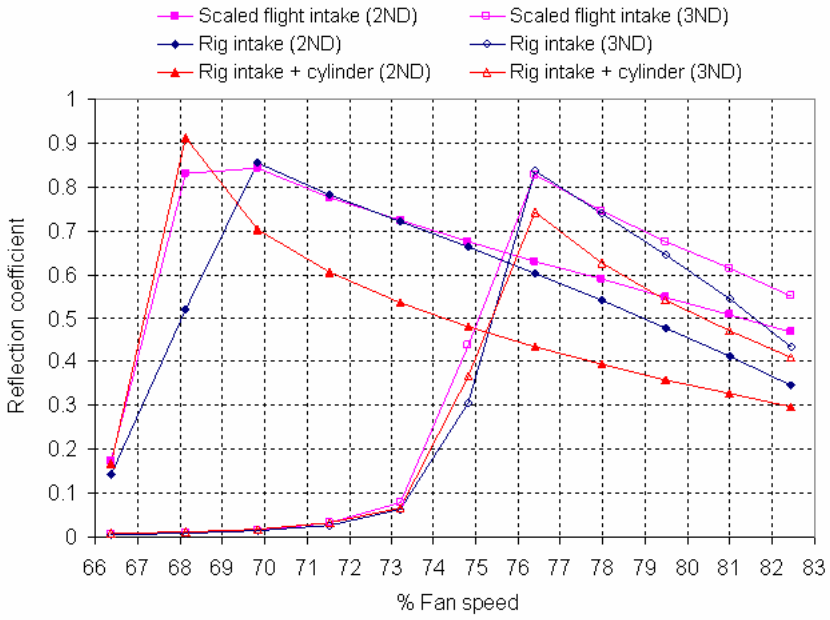

Figure 8.3: Reflection coefficient (ratio of reflected to incident mode amplitude) at the source plane versus fan speed, showing the effect of geometry for 2ND and 3ND modes.

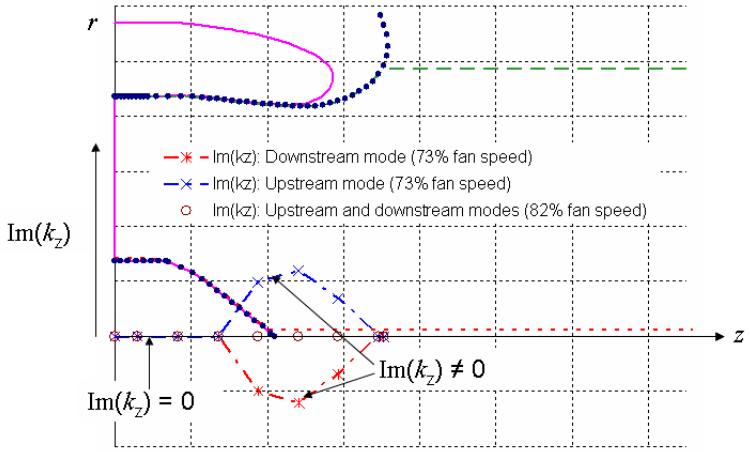

Figure 8.4: Imaginary part of axial wave number for 2ND mode at 73% and 82% fan speeds, at different axial stations on the intake geometry.

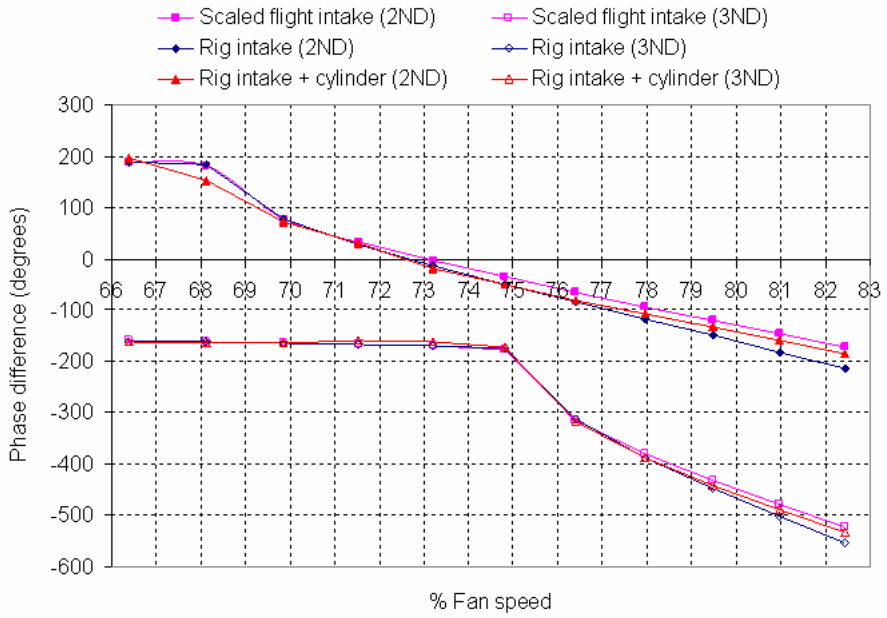

Figure 8.5: Variation of phase difference (between incident and reflected mode) at the source plane with fan speed, showing the effect of geometry for 2ND and 3ND modes.

8.4 Design of a deep liner by using ANPRORAD and SOFT

In this section, ANPRORAD is integrated within SOFT to perform an impedance optimisation for a deep liner. The optimisation process is similar to that used earlier in Chapter 4 with B-induct and SOFT, except that ANPRORAD is used in the place of B-induct.

In this study, the objective is to design a deep liner to minimise the amplitude of the reflected mode ($amp_{reflected}$) at the source plane for the rig geometry in Figure 8.2. A 2ND mode (2,1) incident at the source plane is considered, at 71% fan speed and a frequency of 359 Hz. A short strip of deep liner of variable impedance is installed between a community noise liner whose impedance is fixed during the deep liner optimisation. The impedance of the deep liner is optimised in terms of the non-dimensional resistance r and the non-dimensional reactance χ'. A sketch illustrating the problem set-up is shown in Figure 8.6.

The non-dimensional reactance of the deep liner is permitted to vary between -5 and 5, and the non-dimensional resistance varies between 0 and 5. An ARMOGA search

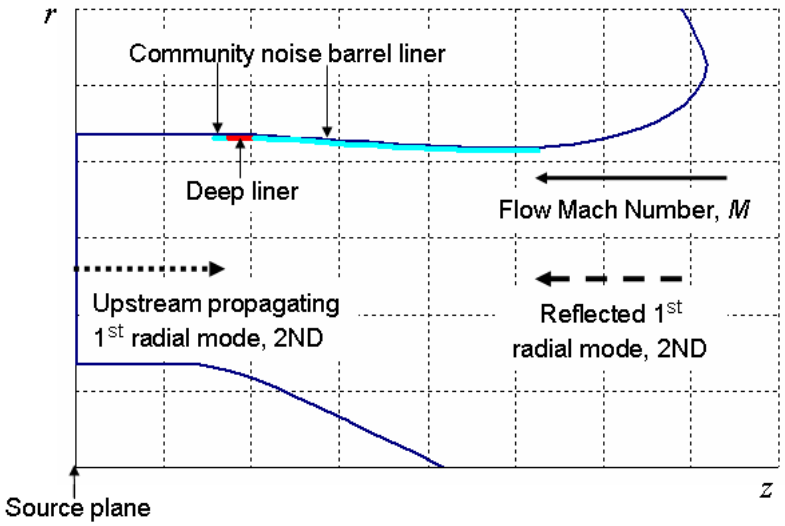

Figure 8.6: Sketch showing problem description for deep liner optimisation to minimise the amplitude of the reflected 2ND mode.

followed by a DHC search is used to explore and exploit the design space. Contours of the amplitude of the reflected mode at the source plane as a function of the resistance and reactance, are shown in Figure 8.7. These are generated from values of the reflected amplitude evaluated at grid points on a regular grid in the design space. These contours are used to check the optimised impedance obtained from SOFT. The superposition of the automatic search on the contours is shown in Figure 8.8. The results agree closely. Data for the SOFT optimisation are presented in Table 8.1.

Table 8.1: Deep liner impedance for minimum reflected amplitude of the 2ND mode at source plane.

Mode	2ND (2,1)
r	0.77
χ'	-1.43
$amp_{reflected}$ (pa)	0.001
CPU time	35m 51s
Number of evaluations	143

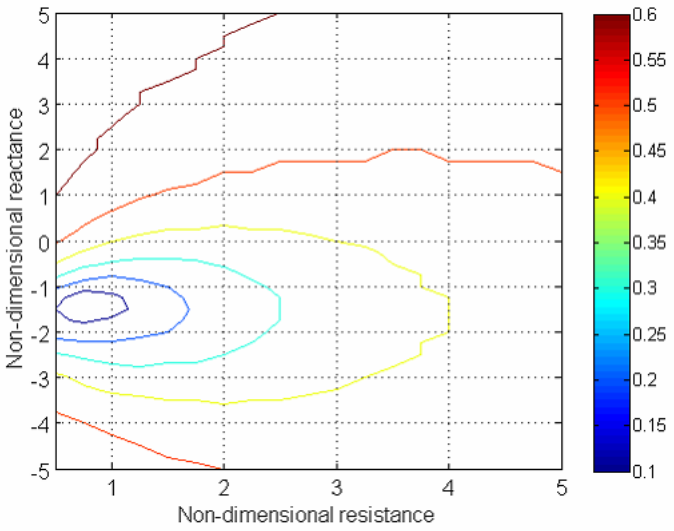

Figure 8.7: Contours of reflected amplitude of the 2ND mode at source plane versus non-dimensional resistance and non-dimensional reactance.

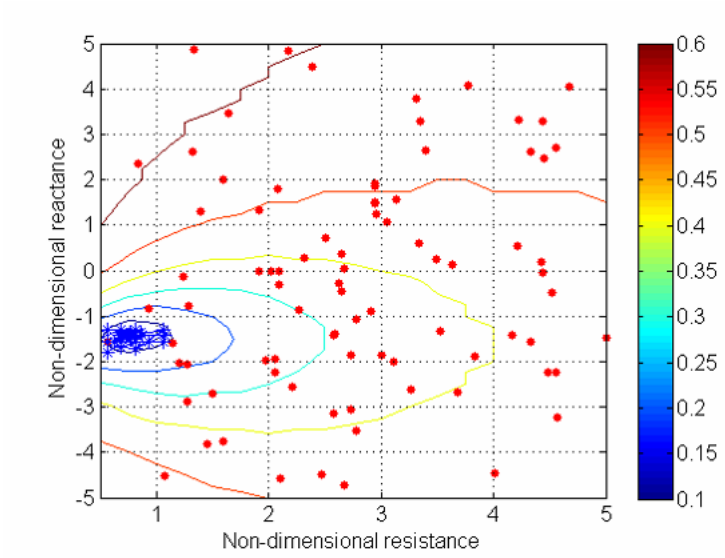

Figure 8.8: ARMOGA search (dots) followed by DHC search (lines and crosses) superposed on contours of reflected mode amplitude.

By using the expression $\chi' = kl - \cot(kd)$ for a single cavity liner model, where k is the wave number, d is the liner depth, and l is the mass inertance (= 0.014 m), the optimum reactance of -1.43 in Table 8.1 corresponds to a liner depth of 3.5 inches. A liner depth of 3.5 inches and a facing sheet resistance of 0.77, are values that one might expect from a conventional barrel liner impedance optimisation which targeted this frequency.

8.5 Conclusion

In this chapter, ACTRAN/TM within the shell program ANPRORAD has been used to predict the amplitude and phase of reflected 2ND and 3ND modes at the source plane, having prescribed incident 2ND and 3ND modes at this plane. The computations were performed over a range of fan speeds and at low frequencies in the vicinity of the cut-on frequencies for these modes. In this study, the effect of geometry on the variation of the reflected mode amplitude and reflected mode phase with fan speed was investigated.

In terms of the effect of geometry on the reflected mode amplitude, the results in Figure 8.3 suggest that the amplitude of the reflected mode is largely determined by the

distance over which the mode is cut-off within the intake and on the extent to which the mode is reflected when it reaches the highlight. The amount of reflection at the highlight depends on the abruptness of the impedance discontinuity. A gradual geometry expansion into the surrounding acoustic region produces a slower impedance change and hence a smaller reflection. This is evident by the fact that the reflection coefficient for the rig intake with the flare is smaller than the reflection coefficient for the scaled flight intake at high fan speeds (see Figure 8.3).

In terms of the phase, the results in Figure 8.5 show a linear variation of the reflected mode phase with fan speed for all three geometries when the incident mode (2ND or 3ND) is cut-on at the source plane. Differences in geometry have a small effect on the slope of the curve.

Finally, ANPRORAD was integrated within SOFT and used to optimise the impedance of a deep liner to minimise the reflected amplitude for a 2ND incident mode at 359 Hz. The optimum facing sheet resistance (0.77) and liner depth (3.5 inches) for the deep liner was found to agree closely with values which might have been expected for a conventional barrel liner at this frequency.

Chapter 9

Conclusions and Future work

9.1 Conclusions

The work reported in this thesis is motivated by the need for industry to use more efficient prediction tools to aid in the design of quieter turbofan aeroengines. This thesis presents novel methodologies that can be used for designing low-noise bypass ducts and intakes. These exploit the capabilities of the commercial FE/IE code ACTRAN/TM, within two shell programs B-induct and ANPRORAD developed at the ISVR to model the propagation of sound in bypass and intake ducts and its radiation to the far field. An automated liner impedance optimisation capability, is demonstrated by exploiting the in-house Rolls-Royce optimisation suite SOFT.

B-induct has been integrated within SOFT, and an optimisation strategy presented which involves a global ARMOGA search followed by a local DHC search procedure to optimise liner impedance. Results from the SOFT optimisation procedure have been presented for single segment and double segment liners.

Results have been presented for an automated liner impedance optimisation of a uniform bypass duct for a single frequency multimodal source. These results suggest that a multi-segment liner is only effective at low frequencies, and not at high frequencies. It appears likely that at low frequencies when fewer modes are present, noise benefits are ob-

tained from the effects of scattering. However at higher frequencies when many modes are present, the effect of scattering is mitigated. Other results suggest that, having different liner impedances on the inner and outer walls could be more effective than multi-segment liners when many modes are present.

In the case of multiple impedance segments, when many modes are present, the results obtained by optimising the impedances in turn (one after the other) give similar results to those obtained by optimising the impedances simultaneously. When few modes are present however, this is not the case since the effects of scattering are exploited more when the impedances are optimised simultaneously.

When the optimisation is performed over a range of frequencies, an A-weighted insertion loss cost function ΔPWL_{Awt}, integrated over one-third octave bands assuming each band is represented by its centre frequency from 0.5-10 kHz is used to simulate EPNL, for preliminary liner design. Using the ΔPWL_{Awt} cost function, an automated liner impedance optimisation has been performed for a real bypass duct geometry. The results from this study have been compared to a full EPNL optimisation for the same bypass duct geometry and shown to give similar results indicating the viability of the ΔPWL_{Awt} cost function in industrial applications.

ANPRORAD has been applied to predict hard-walled and lined far field SPL field shapes for axisymmetric intake configurations. The predicted results have been validated against rig and engine test data at different fan speeds. The hard-walled BPF tone predictions show that, accurate absolute predictions of the far field SPL field shapes are possible for realistic intake geometries and flows, provided that the source modal content is correctly specified. At supersonic fan tip speeds, the prediction of attenuated BPF tone field shapes for lined intakes requires the inclusion of adjustments to account for non-linear propagation close to the fan. At broadband frequencies, instead of using an 'equal power per mode' source in the prediction, the dominance of co-rotating modes may have to be represented in the source to accurately predict hard-walled far field SPL field shapes and liner attenuations.

Computed predictions are also presented in this thesis for a non-axisymmetric drooped

engine nacelle, and compared to static engine test data. BPF tone predictions have been presented. Considering that the engine intake is drooped and the BPF tone predictions are performed for an axisymmetric intake, the predictions are only partially validated. However, measured distortions due to the droop are included in the source definition and good agreement is obtained between the predicted and measured data. This suggests that the droop on the engine is important in the modification of the noise source, but has a small geometric effect on its propagation and radiation.

ANPRORAD has also been used to investigate the effect of the intake geometry on low-frequency acoustic reflections of fan flap modes at a range of fan speeds. The results suggest that, the amplitude of the reflected mode is determined by the distance over which the mode is cut-off in the intake, and the by energy left in the mode when it reaches the highlight. In addition, the amount of reflection at the highlight depends on the geometry of the nacelle at the highlight and on any resulting impedance discontinuity.

ANPRORAD was also integrated within SOFT to perform an automated impedance optimisation for a low-frequency (deep) liner to minimise the acoustic reflections from a low-frequency 2ND mode. The optimum impedance from this exercise was found to agree with that of a conventional liner designed for this low frequency.

9.2 Future work

This thesis has introduced novel methodologies that can be used to tackle bypass and intake duct noise problems to aid in the design of quieter engines. However, some aspects of these methods can be developed further so that the capabilities presented in this thesis are more adaptable and so that they can be readily used in a wider range of noise engine design projects.

The automated liner impedance optimisation for bypass ducts presented in this thesis has been developed as far as applying an A-weighting to the liner insertion loss cost function. In the future work, a radiation model should be incorporated into the acoustic prediction so that a far field SPL directivity can be predicted and subsequently the EPNL

can be used as the cost function for the liner impedance optimisation.

In the case of the intake, the results presented in this thesis show that, accurate noise predictions are possible for realistic geometries and flows provided the modal content of the source is correctly specified. However, for future engine designs, the modal power distributions of the fan source and absolute levels will not be available beforehand. The ANPRORAD methodology should be further developed by incorporating empirical, theoretical or computational models to describe the modal distributions and absolute levels for the fan noise source for a given engine without recourse to in-duct measured data.

While ANPRORAD has been integrated within SOFT to perform impedance optimisations for low-frequency liners to minimise acoustic reflections in the intake, this tool can be further developed to simultaneously optimise an intake barrel liner for community noise and a deep liner for low-frequency acoustic reflections.

Appendix A

Absorption coefficient of a locally reacting impedance subject to a diffuse incident field

In sections 3.4.3.1 and 3.4.3.2, the expressions for the absorption coefficient for a locally reacting liner were obtained by considering the complex pressure amplitudes of the incident and reflected waves for all the propagating modes. However, the same result should be obtained from using the expression obtained from integrating the power absorbed by an infinite locally reacting impedance plane (see Figure A.1) subject to a diffuse incident field. This is because a diffuse sound field can be modelled as mutually uncorrelated plane waves that propagate in all directions with equal probability, this is similar to a situation in a straight tube when a large number of modes are present.

In this section, the expression for the absorption coefficient of an infinite locally reacting impedance plane (for a single frequency), derived by integrating the sound power absorbed over all angles of incidence (0 to $\pi/2$), is used to produce contours of absorption coefficient versus facing sheet resistance and liner depth. These contours are then used to confirm the contours of absorption coefficient obtained by considering the complex pressure amplitudes of the incident and reflected waves for all the propagating modes (see

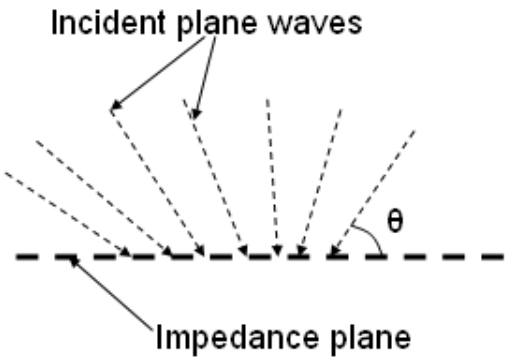

Figure A.1: Equally distributed plane waves for all angles of incidence θ.

Equation (3.32)).

A.1 Methods

The expression for the absorption coefficient obtained from integrating the power absorbed by an infinite locally reacting impedance plane over all angles of incidence, can be written as (see reference [116]):

$$\eta = 8\Gamma \left[\left(1 - \Gamma \log_{10} \left(\frac{r}{\Gamma} + 2r + 1 \right) \right) + \left(\Gamma \frac{\chi}{r} \right) \left(\left(\frac{r}{\chi'} \right)^2 - 1 \right) \tan^{-1} \left(\frac{\chi'}{r+1} \right) \right] \tag{A.1}$$

where,

$$\chi' = \frac{\chi}{\rho c}, \quad r = \frac{R}{\rho c}, \quad \Gamma = \frac{r}{r^2 + \chi'^2} \quad \text{and} \quad \chi = \rho c \left[kl - \cot\left(kd \right) \right].$$

Contours obtained for a single frequency multiple mode source (for 5 kHz) using Equation (A.1) are shown in Figure A.2(a) alongside contours for the absorption coefficient obtained from considering incident and reflected waves for all the propagating modes in Figure A.2(b).

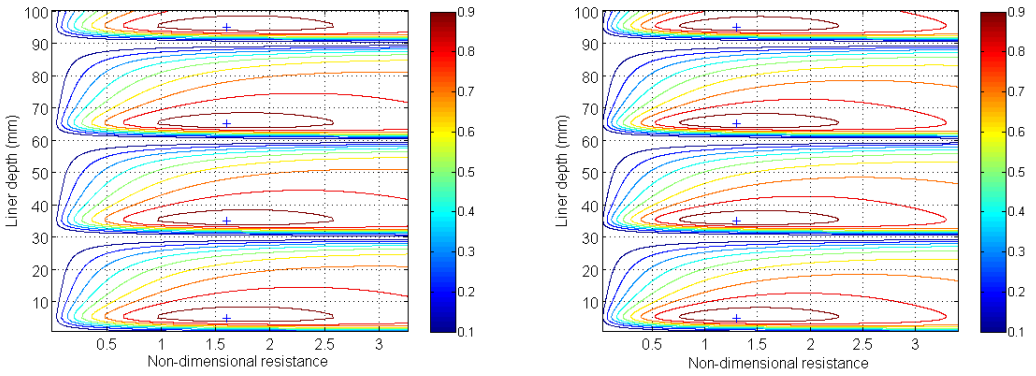

(a) Contours by using 'diffuse field' model (b) Contours by using 'all propagating modes'

Figure A.2: Contour plots for absorption coefficient obtained using two different methods.

A.2 Discussion

From Figures A.2(a) and A.2(b) it can be seen that using both methods of calculating the absorption coefficient give very similar results as expected. This is because, in the method of 'propagating modes' high order modes are essentially equivalent to a number of superposed tranverse modes, which radiate in all directions like sound radiating from an infinitely long plate.

Both methods give very similar multiple optima: a non-dimensional resistance of 1.6 occurring at liner depths of 5 mm, 35 mm, 65 mm and 95 mm for the 'diffuse field' model and a non-dimensional resistance of 1.3 occurring at liner depths of 5.5 mm, 35.5 mm, 65.5 mm and 95.5 mm for the method using 'all propagating modes'.

Bibliography

[1] C. R. McAleer, "Predicting fan noise propagation in aeroengine bypass ducts," EngD Thesis, Institute of Sound and Vibration Research, University of Southampton, UK, March 2009.

[2] R. J. Astley, A. Agarwal, K. R. Holland, P. F. Joseph, R. H. Self, M. G. Smith, R. Sugimoto, and B. J. Tester, "Predicting and reducing aircraft noise," in *14th International Congress on Sound and Vibration*, Cairns, Australia, 9-12 July 2007.

[3] M. J. T. Smith, *Aircraft Noise*. Cambridge University Press, 2004.

[4] R. Sugimoto, "B-induct users' manual, shell program for ACTRAN induct analysis for bypass ducts," (ISVR, University of Southampton, UK), November 2004.

[5] R. J. Astley, "Propulsion system noise - turbomachinery," in *The Encyclopedia of Aerospace Engineering (Richard Blockley and Wei Shyy editors)*, John Wiley and Sons, Chichester (in publication), 2010.

[6] International Civil Aviation Organisation, "Volume 1: Aircraft noise" in *Annex 16 to the Convention on International Civil Aviation: Environmental Protection*, 5th Edition, July 2008.

[7] C. Hodge, "Quiet aircraft design and operational characteristics," in *Aeroacoustics of flight vehicles: Theory and practice, volume 2: Noise control* (H. Hubbard, ed.), pp. 383–413, 1991.

[8] P. Arguelles, J. Lumsden, M. Bischoff, D. Ranque, P. Busquin, S. Rasmussen, B. Droste, P. Reutlinger, R. Evans, R. Robins, W. Kroll, H. Terho, J. Lagardere, A. Wittlov, and A. Lina, "Meeting society's needs and winning global leadership," in *European aeronautics: A vision for 2020*, January 2001.

[9] *Actran/TM 2006 users' manual*. Free Field Technologies, Leuven-la-Neuve, Belgium, 2006.

[10] S. Shahpar, "SOFT: A new design and optimisation tool for turbomachinery," in *Evolutionary methods for design, optimisation and control* (K. Giannakoglou, D. Tsahalis, J. Periaux, K. Papailiou, and T. Fogarty, eds.), CIMNE, Barcelona, 2002.

[11] I. Achunche, "Numerical acoustic optimisation for sound propagation in aero-engine bypass ducts," EngD Mini-thesis, Institute of Sound and Vibration Research, University of Southampton, UK, October 2007.

[12] J. M. Tyler and T. G. Sofrin, "Axial flow compressor noise studies," *SAE transactions*, vol. 70, pp. 309–332, 1962.

[13] D. Lansing and W. Zorumski, "Effects of wall admittance changes on duct transmission and radiation of sound," *Journal of Sound and Vibration*, vol. 27, no. 1, pp. 85–100, 1973.

[14] A. McAlpine, R. Astley, V. Hii, N. Baker, and A. Kempton, "Acoustic scattering by an axially-segmented turbofan inlet duct liner at supersonic fan speeds," *Journal of Sound and Vibration*, vol. 294, pp. 780–806, 2006.

[15] T. R. Law and A. P. Dowling, "Optimisation of annular and cylindrical liners for mixed exhaust aeroengines," in *13th AIAA/CEAS Aeroacoustics Conference*, Rome, Italy, 7-9 May 2007, AIAA-2007-3546.

[16] T. R. Law and A. P. Dowling, "Reduction of aeroengine tonal noise using scattering from a multi-segmented liner," in *14th AIAA/CEAS Aeroacoustics Conference*, Vancouver, Canada, 5-7 May 2008, AIAA-2008-2978.

[17] C. J. Brooks and A. McAlpine, "Sound transmission in ducts with sheared mean flow," in *13th AIAA/CEAS Aeroacoustics Conference*, Rome, Italy, 7-9 May 2007, AIAA-2007-3545.

[18] L. Lafronza, A. McAlpine, A. J. Keane, and R. J. Astley, "Computer-aided liner optimisation for broadband noise," in *10th AIAA/CEAS aeroacoustics conference*, Manchester, United Kingdom, 10-12 May 2004, AIAA-2004-3029.

[19] R. J. Astley, V. Hii, and G. Gabard, "A computational mode matching approach for propagation in three-dimensional ducts with flow," in *12th AIAA/CEAS Aeroacoustics Conference*, Cambridge, MA, 8-10 May 2006, AIAA-2006-2528.

[20] A. J. Kempton, "Ray-theory to predict the propagation of broadband fan noise," in *6th AIAA Aeroacoustics Conference*, Hartford, CT, 4-6 June 1980, AIAA-80-0968.

[21] A. J. Kempton, "Ray-theory and mode-theory predictions of intake-liner performance: A comparison with engine measurements," in *8th AIAA Aeroacoustics Conference*, Atlanta, GA, 11-13 April 1983, AIAA-83-0711.

[22] A. J. Kempton and M. G. Smith, "Ray-theory predictions of the sound radiated from realistic engine intakes," in *7th AIAA Aeroacoustics Conference*, Palo Alto, CA, 5-7 Oct 1981, AIAA-81-1982.

[23] B. Tester, "Ray models for sound propagation and attenuation in ducts, in the absence of mean flow," *Journal of Sound and Vibration*, vol. 27, no. 4, pp. 515–531, 1973.

[24] B. Tester, "The propagation and attenuation of sound in lined ducts containing uniform or 'plug' flow," *Journal of Sound and Vibration*, vol. 28, no. 2, pp. 151–203, 1973.

[25] W. Boyd, A. J. Kempton, and C. L. Morfey, "Ray-theory predictions of the noise radiated from aeroengine ducts," in *9th AIAA/NASA Aeroacoustics Conference*, Williamsburg, VA, 15-17 Oct 1984, AIAA-84-2332.

[26] D. McNamara, C. Pistorius, and J. Malherbe, *Introduction to The Uniform Geometric Theory of Diffraction*. E & F N Spon, London, 1990.

[27] S. Chapman, J. Ockendon, and V. Saward, "Edge diffraction of creeping rays," *Journal of the Acoustical Society of America*, vol. 107, no. 4, pp. 1841–1845, 2000.

[28] S. Chapman, J. Lawry, J. Ockendon, and R. Tew, "On the theory of complex rays," *SIAM Review*, vol. 41, no. 3, pp. 417–509, 1999.

[29] W. Eversman, "Theoretical models for duct acoustics propagation and radiation," in *Aeroacoustics of flight vehicles: Theory and practice, volume 2: Noise control* (H. Hubbard, ed.), pp. 101–163, 1991.

[30] C. Brooks, "Prediction and control of sound propagation in turbofan engine bypass ducts," EngD Thesis, Institute of Sound and Vibration Research, University of Southampton, September 2007.

[31] G. Homicz and J. Lordi, "A note on the radiative directivity patterns of duct acoustics modes," *Journal of Sound and Vibration*, vol. 41, no. 3, pp. 283–290, 1974.

[32] E. Rice, "Multimodal far-field acoustic radiation pattern using cutoff ratio," *AIAA Journal*, vol. 16, no. 9, pp. 906–911, 1978.

[33] E. Rice, "Optimum wall impedance for spinning modes - a correlation with mode cut-off ratio," *Journal of Aircraft*, vol. 16, no. 5, pp. 336–343, 1978.

[34] P. Joseph and C. Morfey, "Multimodal radiation from an unflanged, semi-infinite circular duct," *Journal of the Acoustical Society of America*, vol. 105, no. 5, pp. 2590–2600, 1999.

[35] G. Gabard and R. Astley, "Theoretical model for sound radiation from annular jet pipes: Far- and near-field solutions," *Journal of Fluid Mechanics*, vol. 549, pp. 315–341, 2005.

[36] R. Munt, "The interaction of sound with a subsonic jet issuing from a semi-infinite cylindrical pipe," *Journal of Fluid Mechanics*, vol. 83, no. 4, pp. 609–640, 1977.

[37] R. Munt, "Acoustic transmission properties of a jet pipe with subsonic jet flow: I. The cold jet reflection coefficient," *Journal of Sound and Vibration*, vol. 142, no. 3, pp. 413–436, 1990.

[38] S. Rienstra, "Acoustic radiation from a semi-infinite annular duct in a uniform subsonic mean flow," *Journal of Sound and Vibration*, vol. 94, no. 2, pp. 267–288, 1984.

[39] C. Tam and J. Webb, "Dispersion-relation-preserving finite difference schemes for computational acoustics," *Journal of Computational Physics*, vol. 107, pp. 262–281, 1993.

[40] T. Colonius and S. Lele, "Computational aeroacoustics: progress on non-linear problems of sound generation," *Progress in Aerospace Sciences*, vol. 40, pp. 345–416, 2004.

[41] A. Agarwal, P. Morris, and R. Mani, "Calculation of sound propagation in uniform flows: supression of instability waves," *AIAA Journal*, vol. 42, no. 1, 2004.

[42] X. Zhang, X. Chen, C. Morfey, and B. Tester, "Computation of fan noise radiation through a realistic engine exhaust geometry with flow," in *9th AIAA/CEAS Aeroacoustics Conference*, Hilton Head, SC, 12-14 May 2003, AIAA-2003-3267.

[43] S. K. Richards, X. Chen, and X. Zhang, "Parallel computation of 3d acoustic radiation from an engine intake," in *11th AIAA/CEAS Aeroacoustics Conference*, Monterey, CA, 23-25 May 2005, AIAA-2005-2947.

[44] Y. Ozyoruk, L. Long, and M. Jones, "Time-domain numerical simulation of a flow impedance tube," *Journal of Computational Physics*, vol. 146, pp. 85–100, 1998.

[45] N. Schoenwald, L. Panek, C. Richter, and F. Thiele, "Investigation of sound radiation from a scarfed intake by CAA-FWH simulations using overset grids," in *13th AIAA/CEAS Aeroacoustics Conference*, Rome, Italy, 7-9 May 2007, AIAA-2007-3524.

[46] L. Panek, N. Schoenwald, C. Richter, and F. Thiele, "Simulation of the rearward propagation of fan noise through a long cowl aero-engine," in *14th AIAA/CEAS Aeroacoustics Conference*, Vancouver, Canada, 5-7 May 2008, AIAA-2008-2820.

[47] J. Manera, R. Leneveu, S. Caro, and J. Mardjono, "Broadband turbomachinery noise: exhaust noise computations with ACTRAN/TM and ACTRAN/DGM," in *15th AIAA/CEAS Aeroacoustics Conference*, Miami, FL, 11-13 May 2009, AIAA-2009-3292.

[48] B. Schiltz, R. Leneveu, S. Caro, Y. Druon, and A. Mosson, "Exhaust noise prediction of realistic 3d lined turbofans submitted to strong shear layers," in *15th AIAA/CEAS Aeroacoustics Conference*, Miami, FL, 11-13 May 2009, AIAA-2009-3416.

[49] R. Leneveu, B. Schiltz, S. Laldjee, and S. Caro, "Performance of a DGM scheme for LEE and applications to aircraft engine exhaust noise," in *14th AIAA/CEAS Aeroacoustics Conference*, Vancouver, Canada, 5-7 May 2008, AIAA-2008-2884.

[50] Y. Zhao and P. Morris, "The prediction of fan exhaust noise propagation," in *11th AIAA/CEAS Aeroacoustics Conference*, Monterey, CA, 23-25 May 2005, AIAA-2005-2815.

[51] T. J. R. Hughes and A. Brooks, "A multidimensional upwind scheme with no crosswind diffusion," in *Finite elements for convection dominated flows* (T. Hughes, ed.), pp. 19–35, Vol. AMD 34 of ASME, 1979.

[52] D. Kelly, S. Nakazawa, and O. Zienkiewics, "A note on anisotropic balancing dissipation in the finite element method approximation to convection diffusion problems," *International Journal on Numerical Methods in Engineering*, vol. 15, pp. 1705–1711, 1980.

[53] Y. Ozyoruk, "Numerical prediction of aft radiation of turbofan tones through exhaust jets," *Journal of Sound and Vibration*, vol. 325, pp. 122–144, 2009.

[54] S. Redonnet, C. Mincu, and E. Manoha, "Computational aeroacoustics of realistic co-axial engines," in *14th AIAA/CEAS Aeroacoustics Conference*, Vancouver, Canada, 5-7 May 2008, AIAA-2008-2826.

[55] Y. Ozyoruk and L. Long, "Computation of sound radiation from engine inlets," *AIAA Journal*, vol. 34, no. 5, pp. 894–901, 1996.

[56] W. Eversman, "Mapped infinite wave envelope elements for acoustic radiation in a uniformly moving medium," *Journal of Sound and Vibration*, vol. 224, no. 4, pp. 665–687, 1999.

[57] R. J. Astley, G. J. Macaulay, J.-P. Coyette, and L. Cremers, "Three-dimensional wave-envelope elements of variable order for acoustic radiation and scattering. Part I. Formulation in the frequency domain," *Journal of the Acoustical Society of America*, vol. 103, no. 1, pp. 49–63, 1998.

[58] R. J. Astley and J. A. Hamilton, "Modelling tone propagation from turbofan inlets - the effect of extended lip liners," in *8th AIAA/CEAS Aeroacoustics Conference*, Breckenridge, CO, 17-19 June, AIAA-2002-2449.

[59] B. V. Antwepen, R. Leneveu, S. Caro, and P. Ferrante, "New advances in the use of Actran/TM for nacelle simulations," in *14th AIAA/CEAS Aeroacoustics Conference*, Vancouver, Canada, 5-7 May 2008, AIAA-2008-2827.

[60] N. Tsuchiya, "Inlet shell users' manual," (ISVR, University of Southampton, UK), June 2005.

[61] I. Achunche, J. Astley, R. Sugimoto, and A. Kempton, "Prediction of forward fan noise propagation and radiation from intakes," in *15th AIAA/CEAS Aeroacoustics Conference*, Miami, FL, 11-13 May 2009, AIAA-2009-3239.

[62] R. Sugimoto and R. J. Astley, "Modelling of flow effects on propagation and radiation from bypass ducts," in *11th AIAA/CEAS Aeroacoustics Conference*, Monterey, CA, 23-25 May 2005, AIAA-2005-3011.

[63] R. Sugimoto, R. J. Astley, L. De Mercato, K. R. Holland, and V. Jurdic, "Prediction methods for propagation in bypass ducts and comparison with measured data," in *11th AIAA/CEAS Aeroacoustics Conference*, Monterey, CA, 23-25 May 2005, AIAA-2005-3059.

[64] R. Sugimoto and R. J. Astley, "Validation and application of a hybrid prediction scheme for bypass ducts," in *12th AIAA/CEAS Aeroacoustics Conference*, Cambridge, MA, 8-10 May 2006, AIAA-2006-2520.

[65] R. Sugimoto, R. J. Astley, G. Gabard, and N. Tsuchiya, "Three-dimensional effects of geometries and acoustic treatments on bypass-duct noise," in *13th AIAA/CEAS Aeroacoustics Conference*, Rome, Italy, 7-9 May 2007, AIAA-2007-3549.

[66] C. McAleer, R. J. Astley, K. Holland, R. Sugimoto, and A. Kempton, "Fan noise propagation within curved bypass ducts with 3D features," in *14th AIAA/CEAS Aeroacoustics Conference*, Vancouver, Canada, 5-7 May 2008, AIAA-2008-2878.

[67] S. Lidoine, H. Batard, and A. Delnevo, "Acoustic radiation modelling of aeroengine intake, comparison between analytical and numerical methods," in *7th AIAA/CEAS Aeroacoustics Conference*, Maastricht, The Netherlands, 28-30 May 2001, AIAA-2001-2140.

[68] F. Montetagaud and S. Montoux, "Negatively scarfed intake: design and acoustic performance," in *11th AIAA/CEAS Aeroacoustics Conference*, Monterey, CA, 23-25 May 2005, AIAA-2005-2944.

[69] A. Keane and P. Nair, *Computational approaches for aerospace design.* John Wiley and Sons Ltd., 2005.

[70] P. Boggs and J. Tolle, "Sequential quadratic programming," *Acta Numerica*, vol. 4, no. 4, pp. 1–51, 1995.

[71] P. Boggs and J. Tolle, "A strategy for global convergence in a sequential quadratic programming algorithm," *SIAM Journal of Numerical Analysis*, vol. 26, pp. 600–623, 1989.

[72] D. Yuret and M. de la Maza, "Dynamic hill climbing: overcoming the limitations of optimization techniques," *Proceedings of the 2nd Turkish Symposium on Artificial Intelligence and Artificial Neural Networks, Istanbul, Turkey*, pp. 254–260, 1993.

[73] S. Kirkpatrick, C. D. Gelatt Jr., and M. P. Vecchi, "Optimization by simulated annealing," *Science*, vol. 220, pp. 671–680, 1983.

[74] D. Goldberg, *Genetic Algorithms in Search, Optimization and Machine Learning.* Addison-Wesley, 1989.

[75] R. Fisher, *The Design of Experiments.* Oliver and Boyd, Edinburgh, 1935.

[76] A. A. Giunta, S. F. Wojtkiewics Jr., and M. S. Eldred, "Overview of modern design of experiments methods for computational simulations," in *Proceedings of the 41st AIAA Aerospace Sciences Meeting and Exhibit*, Reno, NV, 6-9 January 2003, AIAA-2003-0649.

[77] I. Sobol, V. Turchaninov, Y. Levitan, and S. B.V., "Lptau: Quasi-random sequence generators," *Russian Academy of Sciences*, Moscow, 1992.

[78] A. Hedayat, N. Sloane, and J. Stufken, *Orthogonal Arrays: Theory and Applications.* Springer, 1999.

[79] A. Forrester, A. Sobester, and A. Keane, *Engineering Design via Surrogate Modelling. A Practical Guide.* John Wiley and Sons, Ltd, 2008.

[80] J. Sacks, W. W. J., M. T. J., and H. P. Wynn, "Design and analysis of computer experiments," *Statistical Science*, vol. 4, pp. 409–435, 1989.

[81] K. Kryter, "Concepts of perceived noisiness, their implementation and application," *The Journal of the Acoustical Society of America*, vol. 43, no. 2, pp. 344–361, 1968.

[82] C. A. Powell and J. M. Fields, "Human response to aircraft noise," in *Aeroacoustics of flight vehicles: Theory and practice, volume 2: Noise control* (H. Hubbard, ed.), pp. 1–52, 1991.

[83] G. Box and N. Draper, *Empirical Model-Building and Response Surfaces.* John Wiley and Sons, 1987.

[84] J. Robinson and W. Watson, "Performance of a checkerboard liner with uncertain impedances," in *11th AIAA/CEAS Aeroacoustics Conference*, Monterey, CA, 23-25 May 2005, AIAA-2005-2850.

[85] T. Law and A. Dowling, "Optimization of traditional and blown liners for a silent aircraft," in *12th AIAA/CEAS Aeroacoustics Conference*, Cambridge, MA, 8-10 May 2006, AIAA-2006-2525.

[86] D. Copiello and P. Ferrante, "Multi-objective optimization of 'true' zero-splice liners for aero-engine intakes," in *15th AIAA/CEAS Aeroacoustics Conference*, Miami, FL, 11-13 May 2001, AIAA-2009-3107.

[87] K. Deb, A. S., P. A., and T. Meyarivan, "A fast elitist non-dominated sorted genetic algorithm for multi-objective optimization: NSGA-II," in *Parallel Problem Solving from Nature VI conference*, Paris, 2000.

[88] K. Schittkowski, "NLPQL, a fortran subroutine for solving constrained non-linear programming problems," *Annals of Operations Research*, vol. 5, pp. 485–500, 1986.

[89] J. H. Holland, "Genetic algorithms and the optimal allocation of trials," *SIAM Journal on Computing*, vol. 2, no. 2, pp. 88–103, 1973.

[90] D. Sasaki and S. Obayashi, "Efficient search for trade-offs by adaptive range multi-objective genetic algorithms," *Journal of Aerospace Computing, Information, and Communication*, vol. 2, pp. 44–64, 2005.

[91] D. Sasaki, "Adaptive range multi-objective genetic algorithms for aerodynamic design problems," Phd Thesis, Department of System Information Sciences, Tohoku University, Japan, 2004.

[92] L. Ingber, "Simulated annealing: Practice versus theory," *Mathematical and Computer Modelling*, vol. 18, no. 11, pp. 29–57, 1993.

[93] M. K. Myers, "On the acoustic boundary condition in the presence of flow," *Journal of Sound and Vibration*, vol. 71, no. 3, pp. 429 – 434, 1980.

[94] R. E. Motsinger and R. E. Kraft, "Design and performance of duct acoustic treatment," in *Aeroacoustics of flight vehicles: Theory and practice, volume 2: Noise control* (H. Hubbard, ed.), pp. 165–205, 1991.

[95] R. J. Astley, "Numerical methods for noise propagation in moving flows, with application to turbofan engines," *Acoustical Science and Technology*, vol. 30, no. 4, pp. 227–239, 2009.

[96] W. Eversman, "The boundary condition at an impedance wall in a non-uniform duct with potential mean flow," *Journal of Sound and Vibration*, vol. 246, no. 1, pp. 63–69, 2001.

[97] C. L. Morfey, "Acoustic energy in non-uniform flows," *Journal of Sound and Vibration*, vol. 14, no. 2, pp. 159–170, 1971.

[98] M. Petyt and C. Jones, "Numerical methods in acoustics," in *Advanced applications in acoustics, noise and vibration* (F. Fahy and J. Walker, eds.), pp. 53–99, Spon Pres, 2004.

[99] B. A. Finlayson, *The method of weighted residuals and variational principles.* London Academic Press, 1977.

[100] R. Astley and W. Eversman, "A finite element formulation of the eignenvalue problem in lined ducts with flow," *Journal of Sound and Vibration*, vol. 65, no. 1, pp. 61–74, 1979.

[101] L. Lafronza, "Computer-aided liner optimization for fan noise propagation and radiation," MPhil Thesis, Institute of Sound and Vibration Research, University of Southampton, UK, 2008.

[102] *MUtifrontal Massively Parallel sparse direct Solver.* http://mumps.enseeiht.fr.

[103] R. Sugimoto and R. Astley, "Validation and application of a hybrid prediction scheme for bypass duct noise," in *12th AIAA/CEAS Aeroacoustics Conference*, Cambridge, MA, 8-10 May 2006, AIAA-2006-2520.

[104] A. McAlpine and M. Fisher, "On the prediction of "buzz-saw" noise in aero-engine inlet ducts," *J. Sound Vib.*, vol. 248, no. 1, pp. 123–149, 2001.

[105] A. McAlpine and M. Fisher, "On the prediction of "buzz-saw" noise in acoustically lined aero-engine inlet ducts," *Journal of Sound and Vibration*, vol. 265, no. 1, pp. 175–200, 2003.

[106] U. Ganz, P. Joppa, J. Patten, and D. Scharpf, "Boeing 18 inch fan rig broadband noise test," *NASA CR 1998 - 208704*, 1998.

[107] Y. Ozyoruk, V. Ahuja, and L. Long, "Time domain simulations of radiation from ducted fans with liners," in *7th AIAA/CEAS Aeroacoustics Conference*, Maastricht, The Netherlands, 28-30 May 2001, AIAA-2001-2171.

[108] A. McAlpine, M. Fisher, and B. Tester, ""buzz-saw" noise: A comparison of measurement with prediction," *Journal of Sound and Vibration*, vol. 290, pp. 1202–1233, 2006.

[109] M. Fisher, B. Tester, and P. Schwaller, "Supersonic fan tone noise prediction," No. AIAA-98-2249, AIAA, 1998.

[110] E. Rademaker, P. Sijtsma, and B. Tester, "Mode detection with an optimised array in model turbofan engine intake at varying shaft speeds," in *7th AIAA/CEAS Aeroacoustics Conference*, Maastricht, The Netherlands, 28-30 May 2001, AIAA-2001-2181.

[111] J. Premo and P. Joppa, "Fan noise source diagnostic test - wall measured circumferential array mode results," in *8th AIAA/CEAS Aeroacoustics Conference*, Breckenridge, CO, 17-19 June 2002, AIAA-2002-2429.

[112] P. Sijtsma, "Using phased array beamforming to identify broadband noise sources in a turbofan engine," in *12th CEAS-ASC workshop and 3rd scientific workshop of X^3-noise*, Bilbao, Spain, 23-24 October 2008.

[113] R. Fernando, Y. Druon, R. Marchiano, and F. Coulouvrat, "A nonlinear computational method for the propagation of shock waves in aero-engine inlets towards a new model for buzz-saw noise prediction," in *15th AIAA/CEAS Aeroacoustics Conference*, Miami, FL, 11-13 May 2009, AIAA-2009-3238.

[114] M. Vahdati, A. I. Sayma, C. Bread, and M. Imregun, "Computational study of intake duct effects on fan flutter stability," *AIAA Journal*, vol. 40, no. 3, pp. 408–418, 2002.

[115] M. Imregun, "Prediction of flutter stability using aeroelastic frequency response functions," *Journal of Fluids and Structures*, vol. 9, pp. 419–434, 1995.

[116] F. Fahy, *Foundations of Engineering Acoustics.* Elsevier Academic Press, 2007.